2018

Electrospray and Superlens Effect of Microdroplets for Laser-Assisted Nanomanufacturing

Eduardo Castillo Orozco
University of Central Florida

ELECTROSPRAY AND SUPERLENS EFFECT OF MICRO-DROPLETS FOR LASER-ASSISTED NANOMANUFACTURING

by

EDUARDO A. CASTILLO OROZCO
B.S. Escuela Superior Politécnica del Litoral, 2012
M.S. University of Central Florida, 2015

A dissertation submitted in partial fulfillment of the requirements
for the degree of Doctor of Philosophy
in the Department of Mechanical and Aerospace Engineering
in the College of Engineering and Computer Science
at the University of Central Florida
Orlando, Florida

Summer Term
2018

Major Professor:
Kumar R. Professor
Kar A. Professor

ABSTRACT

Nanoparticles of various materials are known to exhibit excellent mechanical, chemical, electrical, and optical properties. However, it is difficult to deposit and transform nanoparticles into large two-dimensional and three-dimensional structures, such as thin films and discrete arrays. Electrospray technology and laser heating enable the deposition of these nanoparticles through the dual role of microdroplets as nanoparticle carriers and superlenses. The main goals of this dissertation are to delineate the electrospray modes, to achieve subwavelength focusing, and to enable a process for the deposition of nanoparticles into microlayers and discrete nanodots (a nanodot is a cluster of nanoparticles) on rigid and flexible substrates. This additive manufacturing process is based on the electrospray generation of water microdroplets that carry nanoparticles onto a substrate and the laser sintering of these nanoparticles. The process involves injecting nanoparticles (contained inside electric field-driven water microdroplets) into a hollow laser beam. The laser beam heats the droplets, causing the water to evaporate and the nanoparticles to sinter and form deposit of material on the substrate.

The electrohydrodynamic inkjet printing of nanoparticle suspensions has been accomplished by the operation of an electrospray in microdripping mode and it allows the deposition of monodisperse microdroplets containing nanoparticles into discrete nanodot arrays, narrow lines, and thin films. For flow rates with low Reynolds number, the mode changes from dripping to microdripping

mode, and then to a planar oscillating microdripping mode as the electric capillary number, Ca_e increases. The microdripping mode which is important for depositing discrete array of nanodots is found to occur in a narrow range, $2 \leq Ca_e \leq 2.5$.

The effect of the physical properties on the droplet size and frequency of droplet formation is more precisely described by the relative influence of the electric, gravity, viscous, and capillary forces. A scaling analysis is derived from a fundamental force balance and has yielded a parameter based on the electric capillary number, capillary number, and Bond number. Results for different nanoparticle suspensions with a wide range of physical properties show that the normalized radius of droplet, can be correlated using this parameter in both dripping and microdripping modes. The same parameter also correlates the normalized frequency of droplet formation, N_d^* as an increasing function in the microdripping mode. Viscosity affects the shape of the cone by resisting its deformation and thus promoting a stable microdripping mode. Reduction in surface tension decreases the droplet size in the electrospray modes. However, the capillary size and electrical conductivity have minimal effect on the size of the ejected droplets. Electrical conductivity affects the transition between microdripping and oscillating microdripping modes. Based on this analysis, it is possible to design the electrospray to produce uniform monodisperse droplets by manipulating the voltage at the electrode, for any desired nanoparticle concentration of a suspension to be sintered on a substrate.

For the fabrication of nanodots, a laser beam of wavelength $\lambda = 1064$ nm was focused to a diameter smaller than its wavelength. When the microdroplets did not carry nanoparticles, the subwavelength focusing of the laser yielded nanoholes smaller than its wavelength. Results show

that tiny features with high resolution can be created by loading microdroplets with nanoparticles and squeezing the laser beam to subwavelength regions. Nanodots of silicon and germanium with diameters between 100 - 500 nm have been deposited on a silicon substrate.

This study demonstrates an interdisciplinary mechanism to achieve subwavelength focusing in a laser process. In this process, the microdroplets serve as both a nanoparticle carrier and a superlens that focuses a laser beam to subwavelength diameters up to $\lambda/10$, thus overcoming the diffraction limit. The microdroplets are generated from a suspension of nanoparticles using an electrospray technique and the superlens characteristic of these microdroplets is attributed to three optical phenomena such as Maxwell's fish eye lens or Lüneberg lens, evanescent waves by laser scattering, and evanescent waves by the total internal reflection principle. A microfluidic cooling effect can also contribute to creating subwavelength features.

In summary, this work describes a new laser-assisted additive manufacturing process for the fabrication of nanodots and microlayers using nanoparticles of different materials. In this process, microdroplets from an electrospray are used as nanoparticle carriers and superlenses to focus the laser to a diameter smaller than its wavelength. While this process is demonstrated to produce subwavelength holes and nanodots, the process is scalable to produce narrow lines and thin films of semiconductor materials by an additive manufacturing technique. This process extends the application of infrared lasers to the production of nanostructures and nanofeatures, and, therefore, provides a novel technology for nanomanufacturing.

This dissertation is dedicated to Maria Valentina and Lucas Samin.

ACKNOWLEDGMENTS

I first would like to express my sincere gratitude to my advisors, Prof. Ranganathan Kumar and Prof. Aravinda Kar, for the continuous support of my Ph.D. study and related research, for being my mentors and for helping me to improve my research skills. Their guidance helped me in all the time of research and writing of this dissertation.

My sincere thanks also goes to Prof. Hyoung Jin Cho and Dr. Pawan Pathak for their cooperation in this project and for their valuable comments.

I would also like to thank my undergraduate research assistants Abhishek Sastri and Marcos Barros and my fellow labmate Tianyi Li for their assistance in the laboratory and help in experiments to accomplish this work. Also Prof. Hyoung Jin Cho and his post-doctoral research assistant Pawan Pathak's assistance is highly appreciated for analyzing certain samples by providing SEM images, EDX spectrograph and resistivity data.

Last but not least, I would like to thank my wife and parents for supporting me spiritually throughout writing this dissertation.

TABLE OF CONTENTS

LIST OF FIGURES

LIST OF TABLES

CHAPTER 1
INTRODUCTION

Two technological breakthroughs of the last decade have been subwavelength focusing of a laser beam using a superlens based on metamaterials [1], and patterning of semiconductor materials to produce flexible electronics [2]. Semiconductor materials have been patterned on flexible substrates by conventional inkjet printing to promote new microelectronics technology [3, 4], but the inkjet-printed films require annealing to improve their electrical conductivity and adhesion to the substrate.

Electrohydrodynamics (EHD) is a promising technique to achieve sub-micrometer resolution in jet printing and also eliminate the clogging problem compared to conventional nozzle-based inkjet technologies [5]. Electrosprays present a convenient method to carry nanoparticles within droplets for deposition of semiconductor materials, e.g., copper-indium-diselenide for solar cells [6] and zinc oxide for thin-film transistors [7]. Electrosprays operate in several modes depending on the flow rate and electric potential. The electrospray can operate in steady cone-jet spray mode where nano- and microdroplets are detached from the tip of a capillary tube due to electric force [8, 9], but in general, it can operate in numerous modes depending on the flow rate and electric potential [10, 11]. The thin jet in the steady cone-jet spray mode and the microdripping mode

can provide a steady stream of uniform nano- and microdroplets that can be used in patterning of microdroplets with sub-micrometer resolution.

The ability to achieve subwavelength focusing is limited by the diffraction effect of light. A slab of negative index metamaterials, which is an unconventional alternative to a lens, has the power to focus and achieve smaller focal spot diameters [12]. The objective of those studies has been to overcome the diffraction limit for imaging objects in the nanometer scale, demonstrating very high resolutions of one-sixth [13, 14] and one-twentieth [15] of the light wavelength. However, passive negatively refracting materials have the disadvantage of being inherently dissipative. With positive refraction, the ability to achieve subwavelength focusing has been analyzed for the perfect lens effect of Maxwell's fish eye in both two-dimensional [16] and three-dimensional [17] media. Random nanoparticles [18], solid microspheres [19, 20], and liquid droplets [21, 22] have been utilized to create subwavelength features on substrates. A droplet placed on a substrate provides the lensing effect due to the curvature and refractive index of the liquid, overcoming the diffraction limit and writing patterns that have sizes one-fourth of the laser wavelength [22]. However, the subwavelength focusing by this method is not readily amenable to implementation in practice to produce thin films or nanodot arrays using nanoparticles since this method requires close proximity between the objective of the microscope and the object, and does not provide a convenient means of replacing the liquid droplet lens to supply fresh nanoparticles to the focused laser beam.

On the other hand, the use of nanoparticles and subsequent laser sintering provides a unique means of depositing microlayers on different types of substrates replacing conventional techniques, such as sputtering, chemical vapor deposition, and self-assembly deposition method. An attractive

advantage of using laser nanoforming for thin-film deposition is that the melting temperature of nanoparticles is less than the melting temperature of the corresponding bulk material [23]. Several studies have employed laser for nanoparticle sintering, e.g., deposition of a nanolayer of silver on a polymer has been achieved using laser annealing process with nanoparticles [24], polycrystalline structure of indium tin oxide on a flexible substrate by using a pulsed-laser sintering process [25], and tungsten micro- and nanoparticles have been film coated on stainless steel substrate for solar thermal application [26]. However, the manipulation of nanoparticles for all cases aforementioned has been limited to laboratory conditions and they are not amiable for large-scale fabrication and technical applications.

Therefore, a considerable amount of research has been carried out to produce structures made out of nanoparticles of various materials due to excellent mechanical, chemical, electrical, and optical properties [27, 28]. Electrospray has been used for thin-film deposition [29, 30] and drop-on-demand printing [31, 32]. Separately, laser processing has been used for deposition of microlayers on plastic and other types of substrates [23]. Furthermore, droplets provide the lensing effect due to the curvature and refractive index of the liquid, overcoming the diffraction limit [21, 22]. However, no attempt seems to have been made to combine these technologies.

An interdisciplinary mechanism of interaction between lasers and microdroplets is discussed in this dissertation to achieve subwavelength focusing and deposit nanoparticles on rigid and flexible substrates such as plastic and paper. This additive manufacturing process of microlayers of semiconductor and conductive materials could be used in the fields of microelectronics, optics,

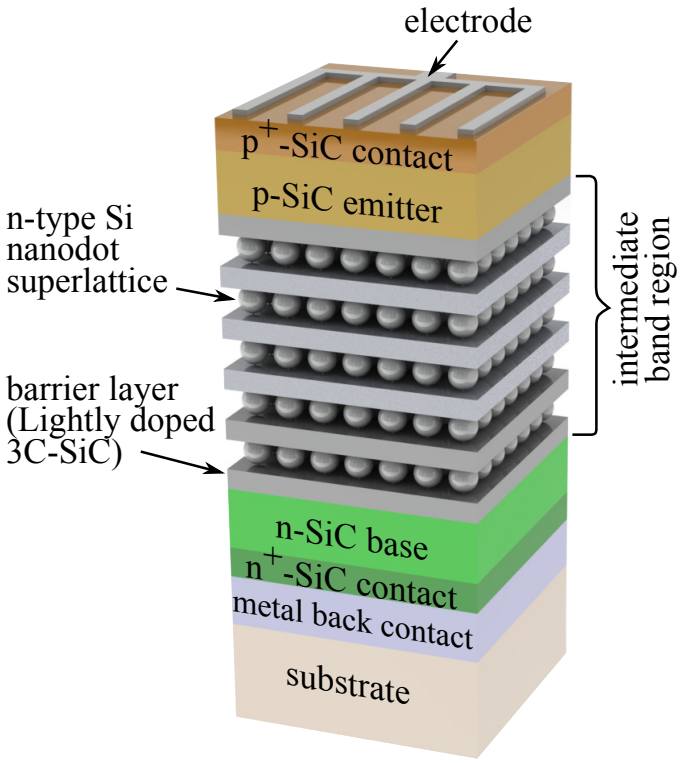

Figure 1.1: Basic IBSC solar cell design showing structural features. Layers are not to scale.

and conformal solar cells such as the intermediate band solar cell (IBSC). Fig. 1.1 shows the basic design of an IBSC with its nanostructure features.

There have been several studies that explore generation and patterning of electrospray micro-droplets, subwavelength focusing of light, and laser sintering of nanoparticles. A review of those studies is presented in Chapter 2. A full description of the methods used in this work is presented in Chapter 3. The results from this study are discussed in Chapter 4 and Chapter 5. Finally, the conclusions are presented in Chapter 6.

CHAPTER 2
LITERATURE REVIEW

2.1 Electrospray deposition

2.1.1 Electrospray of homogeneous liquids

The electrospray is a method of liquid atomization by the application of an electric field between a nozzle and a substrate, or between the nozzle and some kind of extraction electrode (most of the times a ring extractor). Fig. 5.1 shows a typical electrospray setup. Here, the nozzle is a capillary tube and high voltage is applied to it, while the substrate and extraction electrode are earthed.

It should be noticed that different modes of spraying can be obtained due to the interaction of the electrical forces with the system. In 1914, Zeleny [33] reported experimental evidence for several electrosprays operating regimes or modes, such as dripping, burst, pulsating, and cone-jet. Others [34, 35, 36, 37] have observed additional modes, including the microdripping, spindle, multispindle, steady cone-jet spray, multijet, precession, and oscillating mode. Sometimes, these electrospray modes have received different names depending on the authors. For instance, the microdripping mode [38] has also been referred by others as spindle [10] and uniform-dispersion mode [39]. In general, the modes of electrospray depend on liquid properties such as surface tension, viscosity, and electrical conductivity; and on the applied electric field and liquid flow rate.

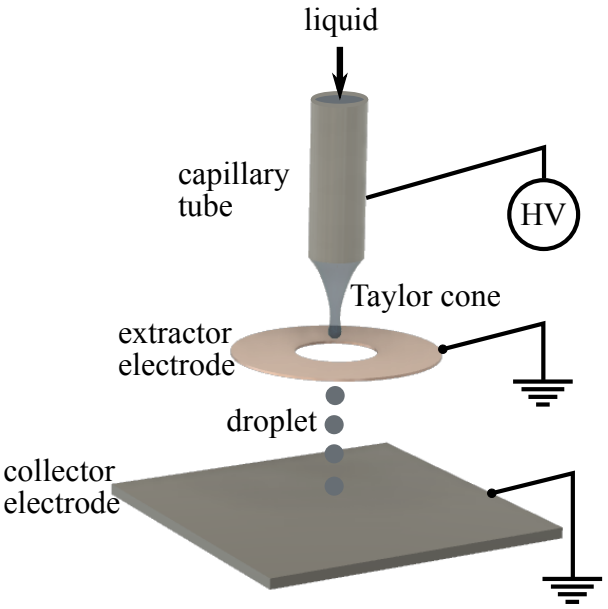

Figure 2.1: Typical electrospray setup

Figure 2.2 shows the operation of electrosprays in various modes. Figs. 2.2a, 2.2b and 2.2c display droplet generation under dripping, microdripping and oscillating microdripping, respectively (water with a surfactant; flow rate: 1.67 mm^3/s; electric voltage: 2500 V, 4000 V, and 5000 V, respectively). Fig. 2.2d displays a steady cone-jet electrospray, where the Taylor cone and thin jet breakup into a stream of highly charged droplets can be observed (adapted from Barrero and Loscertales [40]). Figs. 2.2e, 2.2f and 2.2g show electrosprays in oscillating-jet mode (distilled water; flow rate: 43 mm^3/s; electric voltage: 20000 V), precession mode (distilled water; flow rate: 46.7 mm^3/s; electric voltage: 26000 V) and multijet mode (ethanol; flow rate: 8 mm^3/s; electric voltage: 25000 V), respectively (adapted from Jaworek and Krupta [10]).

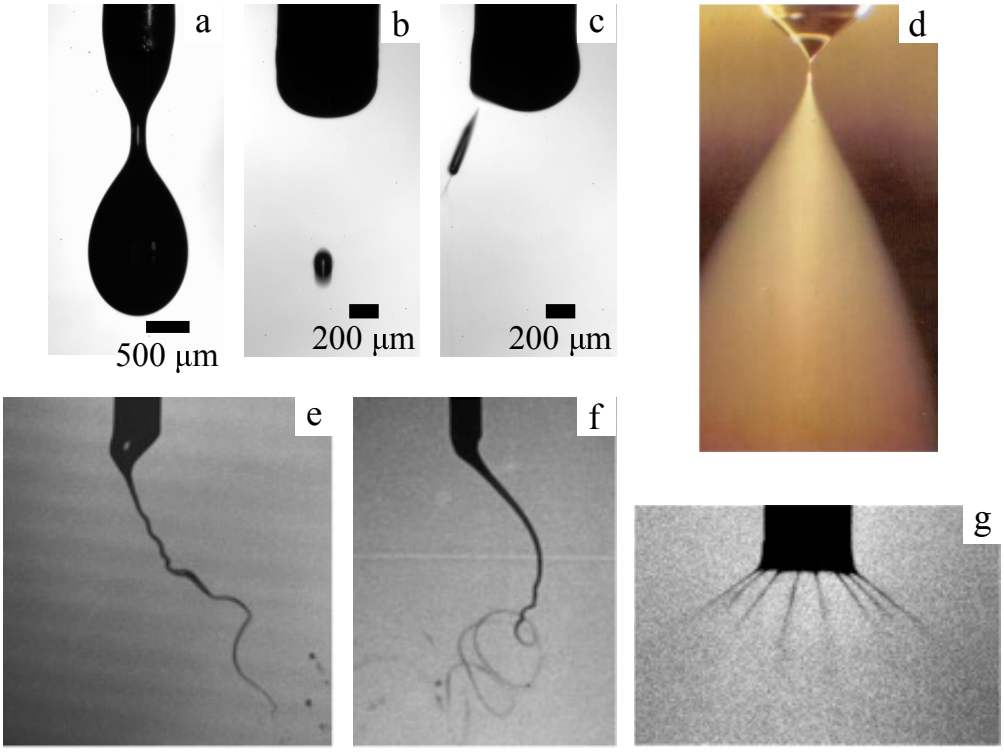

Figure 2.2: Operation of electrospray in various modes. (a) dripping. (b) microdripping. (c) oscillating microdripping. (d) [+]cone-jet spray. (e) [*]oscillating jet. (f) [*]precession. (g) [*]multijet mode. [+]Adapted from Barrero and Loscertales. [*] Adapted from Jaworek and Krupta.

The steady cone-jet spray mode has been the most studied from the aforementioned modes. This is perhaps due to its diverse industrial applications and the nature of the problem being a steady state process. Taylor [41] explained the hydrostatic structure of the conical meniscus, in which a balance between interfacial tension and electrostatic stresses is satisfied on the surface of the equipotential cone. In this operation mode, the liquid interface is deformed into a cone-shaped meniscus (Taylor cone). Mass and charge are emitted from the cone tip in the form of a thin jet of diameter d_j. Charged droplets with a diameter of order d_j, are sprayed from the breakup of this thin jet. These electrospray droplets are highly charged, i.e. up to a fraction of the Rayleigh, which is a magnitude of the charge of a droplet. The charge is given by the following expression

$$q_R = 2\pi(16\gamma\varepsilon_0 r^3)^{1/2} \tag{2.1}$$

where, γ, ε_0 and r are the surface tension, electric permittivity of free space, and radius of the droplet respectively. A detailed description of the dynamics of Taylor cones for liquids with electrical conductivities larger than 10^{-4} S/m can be found in [9].

Although there is not an exact solution to predict the size and frequency of droplets obtained in electrosprays, scaling laws have been developed to characterize each mode. However, results are still controversial. Ogata et al. [42, 43] proposed the following expression for the mean volume-surface diameter of the droplets generated in cone-jet spray mode:

$$\frac{d_{vs}}{(D_o)} = C\, C_a^{2/3} T_i^{2/9} P_o^{-10/9} S_e^{2/5} \tag{2.2}$$

where C is a constant equal to 11.4 for $\gamma/\mu \leq 10$, $C_a = v_j\mu/\gamma$, $T_i = \varepsilon_l\gamma/(\sigma D_o\mu)$, $P_o = \phi/(D_o\gamma/\varepsilon_0)^{1/2}$ and $S_e = H/D_o$. D_o is the outer diameter of the capillary, v_j is the jet velocity, μ is the liquid viscosity, γ is the surface tension, ε_l is the liquid pemittivity, σ is the liquid conductivity, ϕ is the voltage applied to the capillary, and H is the distance between the capillary outlet and counter electrode. The term $(D_o\gamma/\varepsilon_0)^{1/2}$ predicts the minimum voltage necessary for liquid spraying. Ogata et al. [42, 43] obtained this expression from experimental results. The mean volume-surface diameter of the droplets varied in their experiments within the range of $d_{vs} = 100 - 600$ μm.

Tomita et al. [44] proposed the following expressions for the droplet diameter and frequency of droplet formation using the Reynolds and Weber numbers on electrostatic drop formation (miro-dripping mode) for applications in inkjet printing:

$$d^* = \frac{d}{D_o} = 0.25\left(\frac{\sigma}{\sigma_0}\right)^{0.05}\left(\frac{D_i}{D_o}\right)^{0.025} N_{Q\gamma}^{-0.88} We^{0.21} Re^{0.25} \tag{2.3}$$

$$N_d^* = N_d\frac{D_o}{V_0} = 0.29\left(\frac{\sigma}{\sigma_0}\right)^{-0.32}\left(\frac{D_i}{D_o}\right)^{-0.43} N_{Q\gamma}^{0.65} We^{-0.39} Re^{-0.26} \tag{2.4}$$

where $N_{Q\gamma} = \varepsilon_0 E^2 D_o/\gamma$ (ratio of Coulomb force to surface tension force), $E = \phi/H$, $We = \rho V_0^2 D_i^2/(\gamma D_o)$, $Re = \rho V_0 D_i/\mu$, $\sigma_0 = 10^8\sigma_m$, σ_m is the minimum electric conductivity necessary for drop formation (10^{-2} S/m), V_0 is the mean velocity of the fluid in the nozzle, D_i is the internal diameter of the capillary and ρ is the liquid density.

Fernández de la Mora and Loscertales [45] proposed the following equation for droplet diameter in the cone-jet spray mode:

$$d = \alpha\left(\frac{Q\varepsilon_l}{\sigma}\right)^{1/3} \tag{2.5}$$

where α is a constant depending on the liquid permittivity and Q is the liquid flow rate. This result was obtained by conducting experiments with liquids of relatively large electrical conductivities, for which the diameter of the thin jet emitted from the Taylor cone is much smaller than the diameter of the capillary tube ($d_j/D_o \to 0$). In this limit, the structure of the jet is suggested to be independent of electrostatic parameters such as the voltage and electrode configuration, instead, it is governed mostly by the flow rate and physical properties of the liquids.

Hartman et al. [46] proposed the following equation for the same cone-jet spray mode:

$$d = \alpha \left(\frac{Q^3 \varepsilon_0 \rho}{\gamma \sigma} \right)^{1/6} \tag{2.6}$$

Gañan Calvo [47, 48] developed an expression for the mean size of the droplets produced by the steady cone-jet spray mode using scaling laws:

$$d = \alpha d' \left(\frac{Q}{Q'} \right)^{1/2} \tag{2.7}$$

where $d' = (\pi^{-2} \gamma \varepsilon_0^2 \rho^{-1} \sigma^{-2})^{1/3}$, $Q' = \gamma \varepsilon_0 / (\rho \sigma)$ and $\alpha = 2.9$. This result was confirmed by experimental results and d was found to be independent of the liquid permittivity. One can conclude from this expression that the droplet size may be decreased by decreasing the flow rate, decreasing the surface tension, and increasing conductivity of the liquid. Thus, the flow rate is the main controlling parameter. It should be noticed that the viscosity does not appear in Eq. (2.5), (2.6) and (2.7). However, it is expected to have an effect on the droplet size.

For electrospray to occur, certain conditions have been established. Smith [49] noticed that a liquid cannot be atomized by electrical force when its surface tension is higher than 50 mN/m. It is is usually assumed that semi-conducting liquids, which can be atomized by EHD method, are

those of electrical conductivity ranging from 10^{-8} to 10^{-4} S/m [50, 51]. The minimum flow rate at which an electrospray can operate in the steady cone-jet spray mode has been approximated as

$$Q_{min} \approx \gamma \varepsilon_l / (\rho \sigma) \tag{2.8}$$

this minimum flow rate also establishes a minimum diameter of the thin jet

$$d_{j\,min} \approx \varepsilon_{l_r} \left(\frac{\gamma \varepsilon_0^2}{\rho \sigma^2} \right)^{1/3} \tag{2.9}$$

where ε_{l_r} is the relative permittivity of the liquid (liquid dielectric constant). Additionally, it has been reported that $d_{j\,min}$ is of the order of 1 μm when the electric conductivity is in the order of 10^{-3} S/m, but $d_{j\,min}$ can be as small as 10 nm for electrical conductivities of the order of 1 S/m [40].

Watanabe et al. [39] experimented with polymer solutions with high viscosity up to 4000 mPa.s and proposed the following expression for the dripping mode

$$\frac{d}{D_o} = -1.23Es + 5.88 \tag{2.10}$$

and the following expressions for the microdripping mode

$$\frac{d}{D_o} = 5.05Es^{-0.345}We^{0.237}Re^{-0.113} \tag{2.11}$$

$$\frac{d}{D_o} = 1.76Es^{-0.370}We^{0.106}Re^{-0.105} \tag{2.12}$$

where $Es = \varepsilon_0 E^2 D_o / \gamma$, $We = \rho Q^2 / (\gamma D_o^3)$, and $Re = \rho Q / (\mu D_o)$. These two equations were derived experimentally for two different groups of polymer solutions.

2.1.2 Application of electrospray in nanoparticle deposition

Patterning of semiconductor and conductive nanoparticles has a crucial application for fabricating electronic and photonic devices [52, 53]. These nanoparticles can offer the additional benefit of low melting temperature and better mechanical, optical and electrical properties compared to bulk materials. On the other hand, electrosprays present a convenient method to carry these nanoparticles within droplets for deposition of different types of materials.

Direct printing of semiconductor and conductive nanoparticles using electrospray has the potential to significantly lower the cost of producing electronic devices compared to the conventional multistep method of photolithography and chemical processing. Additionally, electrospray is a promising technique to achieve sub-micrometer resolution in jet printing and also eliminates the clogging problem compared to conventional nozzle-based inkjet technologies. These advantages are due to the unique process physics in electrospray for producing droplets of a diameter smaller than the orifice of the nozzle or capillary tube, since the droplets can be formed and ejected from the apex of the conical meniscus instead of the tip of the nozzle. However, there are still technical challenges in this method. Some of the problems are difficulties in preparing the nanosuspensions, uniformity, and stability of the suspensions, optimizing their thermomechanical and electrical properties, and nonuniformities in the printed microstructures due to coffee-ring effect.

Electrohydrodynamic of microdroplets has been used for thin-film deposition [29, 30], drop-on-demand printing [31] and microencapsulation [54, 55, 56] of various nanoparticles for different applications such as electronic devices, solar cells, etc. In general, the material to be deposited

can be sprayed directly upon the substrate, or, the solid film can also be obtained by electrospray deposition of a precursor. Jaworek and Sobczyk [51] present a summary of the different precursors and solvents that have been used for thin-film deposition through electrospray.

Electrospray has been used in solar cell applications, as early as the 1980s. For instance, Mahoney and Perel in 1981 [57] and Pang et al. in 1982 [58] applied electrospray to the fabrication of solar cells, where molten silicon was used for thin-film deposition and later heated at high temperatures (up to 1500 °C) in graphite vessel.

Even though the cone-jet spray mode has been the most used for technical applications, Others have employed different electrospray modes. Kim et al. [59, 60] used multijet mode for thin-film deposition of MgO. In this application, a large number of droplets were deposited simultaneously by using multijet mode, offering an advantage over the steady cone-jet spray mode. Wang et al. [61] used electrospray ink-jet printing to deposit 100 layers of a 10 vol% zirconia suspension in ethanol to produce a wall of ≈ 100 μm in thickness. This wall was dried for 1 hr and sintered in a furnace at a temperature of 1500 °C.

More recently, Muhammad et al. [6] in 2011 reported the use of electrospray for obtaining copper-indium-diselenide films for solar cell fabrication. In the same year, Khan et al. [7] used direct patterning and electrospray deposition (in cone-jet spray mode) for the fabrication of printed thin-film transistors. Park et al. [5] used electrospray ink-jet printing to produce sub-micrometer resolution, resulting in feature sizes in the range of approximately 250 nm to 5 μm . Duan et al. [62] printed micro ceramic patterns using near filed electrospray (the thin jet portion of an electrospray operated in cone-jet spray mode) of polymer-derived ceramics. The highly viscous

polymeric precursor that was patterned with this technique produced lines as narrow as 35 μm and could be converted into ceramics through pyrolysis.

2.2 Optical effects

2.2.1 Subwavelength focusing

Generally speaking, the function of an optical device is to collect and reshape an incident wavefront of light. On the other hand, when an object interacts with light, it emits spherical waves, i.e., rays spread radially in the direction of energy flow (direction of the Poynting vector). Therefore, the optical device collects only a portion of the wavefront and is always unable to collect all the emitted light. As a consequence, there will be an apparent deviation from rectilinear propagation when light advances beyond an obstruction and the optical device, for instance, a lens will be diffraction-limited (there will be a blur spot) [63].

The diffraction limit imposes a fundamental limit on the resolution of an optical device. Ernst Abbe established in 1873 the formula for the resolution limit of a microscope [64]. Light traveling in a medium and converging to a spot with half-angle will make a spot with radius

$$FS = \frac{\lambda}{2n_m sin\theta} \tag{2.13}$$

where λ is the wavelength of light and n_m is the refractive index of the medium.

The ability to achieve super-resolution is limited by the diffraction effect of light. However, the diffraction limit is only valid in the far field. In the near field, devices can use the information

beyond the diffraction limit that is contained in the evanescent field. The basic idea of near-field optics can be understood from the Heisenberg's uncertainty principle. It can be shown by using simple arguments (see [65]) that by having a fast decay of evanescent wave in the z-direction, the resolution in the x- and y-direction can be enhanced. Furthermore, infinite confinement of light becomes theoretically possible and it is not prohibited by any fundamental law.

Techniques such as total internal reflectance microscopy and metamaterials-based superlens have been proposed for imaging with resolution better than the diffraction limit. A slab of negative refractive index material (which is an unconventional alternative to a lens) that has the power to focus and achieve smaller focal spot diameters was suggested by Pendry [12].

Fang et al. [13] successfully resolved objects as small as 60 nm using UV light (at λ of 365 nm) through resonant coupling of evanescent waves to surface plasmon polaritons in silver. Taubner et al. [15] resolved holes of 540 nm using mid-infrared frequency ($\lambda = 11\mu$m) by employing a SiC superlens. The objective of those studies has been to overcome the diffraction limit for imaging objects in the nanometer scale [66], demonstrating very high resolutions of $\lambda/6$ [14, 13], $\lambda/7$ [67], and $\lambda/20$ [15]. However, passive negatively refracting materials have the disadvantage of being inherently dissipative. This means that these superlenses can only acquire images in the near field.

With positive refraction, the ability to achieve subwavelength focusing has been analyzed for the perfect lens effect of Maxwell's fish eye. Leonhardt [16] derived a mathematical proof that Maxwell's fish eye in two-dimensional integrated optics can be used as an instrument with a resolution not limited by the wavelength of light. Later, Leonhardt and Philbin [17] showed that this unlimited resolution is applicable for three dimensions as well.

Furthermore, photonic structures such as photonic crystals [68, 69], spiral zone plate [70] random nanoparticles [18, 71] and solid microspheres [72, 73] have also been used to focus light at subwavelength spots.

2.2.2 Subwavelength patterning

2.2.2.1 Solid microspheres

Solid microspheres of dielectric materials have been utilized to create subwavelength features on substrates. Near-field effects and intensity enhancement have been demonstrated by using individual and layers of nanospheres [19, 74]. This enhancement has been used to produce nanoscale holes on different substrates.

Münzer et al [19] employed this method using polystyrene spheres with a refractive index of 1.58 and diameters of 1.7 μm, 800 nm, and 320 nm for nanopatterning on glass and silicon (Si) surfaces. Nanoscale holes were produced on a Si wafer underneath of the polystyrene spheres. They showed through numerical simulations based on Mie theory that focusing on the sphere as an optical lens, as well as near-field effects and evanescent waves contribute to the intensity enhancement of the field for shaping these holes. It was shown numerically that for radiation of light (800 nm wavelength) over particles of 1.7 μm, 800 nm, and 320 nm in diameter, the enhancement of the field intensity (square of the electric field vector) can be as high as 30, 10, and 4 times that of the incident radiation, respectively. Additionally, the enhanced field is not focused at

the focal length calculated from geometrical optics (obtained using Eq. (3.1) and (3.2)), but instead on the surface of the particles. Wang et al. [75] also showed through analysis based on Mie Theory that a small particle can absorb incident energy near the optical resonance. The cross-section of the optical absorption of the particles can be much larger than the cross-section of the particles and increases inversely proportional to the imaginary part of the dielectric function. Furthermore, for nondissipative cases (i.e., the imaginary part of the dielectric function equals zero) the surface particle is characterized by an input and output windows of energy flux on the surface and allows the generation of sufficiently high electric and magnetic fields around the particle surface in the near-field region.

Theoppakuttai and Chen [20] produced nanopatterns on borosilicate glass (500 μm in thickness) by a Nd:YAG laser (1064 nm wavelength, 10 ns pulse duration) using silica (SiO_2) nanospheres of 640 nm in diameter and 1.39 refractive index. They shined a single pulse of a laser of 3 J/cm^2 from the backside of the glass sample. The direct field enhancement due to the spheres and near-field effects was utilized for patterning of the glass obtaining features of 350 nm in diameter spaced 640 nm between them. The silica nanospheres were placed on the glass surface by applying a colloidal suspension of dispersed nanospheres in de-ionized water and let dry on the glass sample. Later, they also reported [76] the formation of undulations on the glass surface or ripples on the glass when polarized laser with a fluence of 10 mJ/cm^2 was used. The ripples spacing was independent of the incident angle and silica sphere diameter, and their spacing was not always perpendicular to the laser polarization.

Battula et al. [77] produced nanoscale holes on silicon carbide (SiC) with a method similar to [20], but the laser beam was radiated on top of the solid spheres with fluences between 650 mJ/cm^2 - 6 J/cm^2. Silica spheres of 1.76 μm and 640 nm were used to create nanoscale holes with diameters around 150 to 450 nm and depths ranging from 70 to 220 nm depending on the laser energy.

2.2.2.2 Liquid microdroplets

The use of liquid droplets as optical lenses has attracted research interest [78, 79], especially for the dynamic and adaptive response that such devices can offer [80, 81]. When droplets have been used as lenses, the main parameters considered have been refractive index and curvature of the surface. The surface tension of the liquid restores the liquid to produce nearly perfect spherical shapes [82]. Normally the shape of droplet lenses has been constrained by its surface tension [78, 83]; however, artificial membranes can also be used [84, 85].

Even though droplet lenses can offer novel properties such as fast focal length changes through surface oscillation [21], their use as superlenses overcoming the diffraction limit for nanopatterning has been limited.

Duocastella et al. [22] in 2015 used a droplet lens of refractive index 1.5 for subwavelength laser nanopatterning. In their study microdroplets of 100 μm in diameter were first laser-printed (1027 nm wavelength, 450 fs pulse duration) using a laser energy of 8.5 μJ on a polydimethylsiloxane (PDMS) surface and they were later used as lenses to focus the same laser beam, but this

times with fluences between 3.5 - 30 nJ. They demonstrated that a droplet placed on a substrate provides the lensing effect due to the curvature and refractive index of the liquid, overcoming the diffraction limit and writing patterns that have sizes as small as one-fourth of the laser wavelength, i.e., 280 nm in diameter. However, the subwavelength focusing by their method [22] is not readily amenable to implementation in practice to produce thin films or nanodot arrays using nanoparticles since their method requires close proximity between the objective of the microscope and the object, and does not provide a convenient means of replacing the liquid droplet lens to supply fresh nanoparticles to the focused laser beam.

2.3 Laser material processing

2.3.1 Laser additive manufacturing

The use of laser and methods for guiding the focused beam have enabled processes in which material is joined or solidified to create three-dimensional (3D) objects. Additive manufacturing is a major technological breakthrough in engineering and manufacturing. There are many different technologies of additive manufacturing that uses lasers for adding material together to create 3D parts. Amongst these technologies are: Stereolithography (SLA), Selective Laser Sintering (SLS) and Laser Direct Casting (LDC) [86, 87].

Stereolithography: An Ultraviolet (UV) laser, normally a Helium-cadmium (He-Cd) laser of wavelength 325 nm is used to shape on a vat of liquid monomer causing it to polymerize. There-

fore, the resin is photochemically solidified by scanning the laser beam and a 3D part can be constructed by selectively hardening thin layers of the photopolymer.

Selective Laser Sintering: In this process, 3D parts are made by selectively sintering powders without melting. The source of heat for sintering comes usually from a CO_2 laser. The raw materials powders used in this process are composites, polymers such as nylon or polystyrene, metals such as steel, titanium, alloy mixtures. Also, two-component powders can be used, such as glass reinforced nylon and plastic coated metallic powders.

Laser Direct Casting: This process uses a powder feed system and a laser to create a melt pool of powder on top of a surface. The 3D parts are built by adding layers of materials. The material powders used are weldable metals such as use nickel, steel, cobalt, titanium, and alloys. The metallic powders are driven to a powder nozzle by a gas carrier. The heat source for creating the melt pool comes usually from CO_2 and solid-state lasers such as Nd:YAG. State-of-the-art machines include PLC powder feeder, 5-axis table positioning and laser source ranging from 500 to 6000 W. The metallurgical structure of 3D printed parts has epitaxial growth from layer to layer. The process needs to be shrouded in most metals or cast in an inert atmosphere such as argon.

2.3.2 Laser nanoparticle processing

Laser-assisted material processing of nanoparticles can be used in thin-film microelectronic and optical devices. The use of nanoparticles and subsequent laser sintering provides a unique means of depositing thin films on rigid and flexible substrates such as plastic, replacing conventional

techniques, such as sputtering, chemical vapor deposition and self-assembly deposition method. Several studies have employed lasers for nanoparticle sintering. Bet and Kar [23] employed laser nanoforming for thin-film deposition of silicon on plastic substrates and concluded that the particle size in the nanoscale range affects the thermodynamic properties of a material, particularly the melting temperature of nanoparticles is less than the melting temperature of the corresponding bulk material.

More recently, Yeo et al. [24] achieved nanolayer (400 nm) of silver film deposition on a polymer substrate using laser annealing process (Nd:YAG laser operating at 532 nm wavelength) with nanoparticles ranging between 30 to 50 nm. The resultant laser-annealed silver nanoparticle film showed superior electrical and mechanical properties and faster fabrication compared to thermally annealed samples. Park and Kim [25] used pulsed-laser sintering process (KrF excimer laser with a wavelength of 248 nm and pulsed duration 25 ns) for indium tin oxide thin-film deposition on a flexible substrate. They used nanoparticles of 20 nm and reported polycrystalline structures of 200 nm average grain size with a single laser pulse. Shah et al [26] employed pulsed laser sintering (wavelength 1064 nm, frequency 50 kHz) of tungsten micro- (1 to 5 μm) and nanoparticles (80 to 100 nm) for production of thin-film coating on a stainless steel substrate for solar thermal applications. Solar absorption up to 90% was reported at room temperature.

Laser sintering has also been combined with drop-on-demand printing for the production of metallic structures. Bieri et al. [88, 89] used deposition of droplets of gold nanoparticle suspensions (60 - 100 μm) by using a piezoelectric droplet generator and laser curing to obtain gold lines. They reported that the melting point for gold nanoparticles in the range of few nanometers lies be-

tween 300 - 400 °C versus 1064 °C for bulk material. Chung et al. [90] obtained a gold line of 8 μm in width by using the same deposition mechanism as in [88]. Nanoparticle ink (gold nanoparticles in toluene solvent) was printed on a glass substrate and sintered by a continuous Gaussian laser beam.

2.4 Relevance

Application of a new laser-assisted additive manufacturing process for deposition of microlayers of conductive and semiconductor material is relevant in fabrication of microelectronic and optoelectronic devices such as light-emitting diodes [91], solar cells, sensors, actuators, and even ultra-flexible electrodes for neuro-stimulators and prosthetics [92]. Most of the flexible electronic devices are based on organic polymers, i.e., intrinsically conducting polymers. These materials have the advantage that they can keep their electrical conductivity when deformed; however, the electrical connections in this devices are delicate and therefore have presented a limitation on the type of materials and applications [2]. On the other hand, inorganic metals and semiconductor materials, such as silver and silicon are known to have excellent conductive and semiconductor properties; however, these materials will not perform well under bending conditions. Nevertheless, the flexibility of materials increases when the material gets thinner, i.e., the lower the thickness, the higher is the strain required to initiate cracks in a film. Deposition of material through electrospray and subsequent laser sintering allows the fabrication of thin films of these inorganic materials. Therefore, offering a technological answer to aid the development of flexible electronics.

An approach to flexible electronics employs various techniques or processes to reduce the thickness of metal and semiconductor materials from hundreds of nanometers to few tens of micrometers in order to produce thin-film components. This solution involves processes such as photolithography, electron beam evaporation, spin coating, thermal curing, wet etching, plasma enhanced chemical vapor deposition and sputtering [93].

In the search for new solutions for the fabrication of flexible electronics, new materials have been investigated. This is the case of MXene material, which are two-dimensional inorganic compounds, consisting of few atoms thick layers of transition metal carbides, nitrides, or carbonitrides [94]. Recently, in this year An et al. [95] reported a technique to fabricate flexible MXene thin films. These flexible films were built by using an aqueous assembly process called layer-by-layer deposition, where layers of two-dimensional metal carbides ($Ti_3C_2T_x$ nanosheets) were applied in thin sheets on a glass substrate, layering the MXenes in between polymer sheets. Thus, a thin-film composite was built by depositing layers of MXene materials with polymers. The layers are joined together by electrostatic interaction between the layers of negatively charged MXenes and positively charged polyelectrolytes.

Another attractive means is additively manufactured electronics [96, 97, 98]. Additive manufacturing or direct manufacturing of electronics is based on multi-layer inkjet printing [99], nanoparticle inks [100, 101] and thermal curing [102, 103]. Semiconductor materials have been patterned on flexible substrates by conventional inkjet printing to promote nanoelectronics technology. For instance, Huang et al. [104] printed solutions of organic-encapsulated (alkanethiols) gold nanoparticles (1.5 - 5 nm in diameter) to create conductor patterns. The solutions were ap-

plied on a plastic substrate by micropipetting or inkjet printing. Following the evaporation of the solvent, the resulting films were thermally annealed. After this, the solution-deposited nanoparticles were transformed into conductive, continuous films. Ko et al [105] fabricated an organic field effect transistor using inkjet printing and low-temperature selective laser sintering. Carboxylate-functionalized polythiophene was used as the semiconducting material and gold lines were used as electrodes.

2.5 Conclusion

Flexible electronics are forecast to play a major role in the digital industry. For this reason, multiple researchers and high-technological companies are working on developing new solutions. An approach to flexible electronics employs various etching techniques to reduce the thickness of metal and semiconductor materials from hundreds of nanometers to few tens of micrometers. However, this method is not convenient for low-volume production and prototyping of electronics. Furthermore, additive manufacturing technology can be used for fabrication of either rigid or flexible electronics and is an appropriate solution due to its advantages in reducing waste production, freedom to design and innovate, and fabrication time.

Nanoparticles of semiconductors and metals are known to exhibit exceptional mechanical, electrical, and optical properties; however, it is difficult to manipulate and transform nanoparticles into two-dimensional and three-dimensional structures. Nanoparticles have been patterned by conventional inkjet printing of nanoparticle suspensions or nanoinks, but subsequent thermal curing is

needed to evaporate the solvents and to improve their electrical conductivity and adhesion to the substrate.

On the other hand, the radiation from a laser is amongst the finest spectral forms of radiation available. It can be used as a heat source at localized spots and its thermal penetration depth can be controlled in such a way that material can be sintered without melting the substrate. However, diffraction effects impose a fundamental limit on the minimum focal spot that can be achieved.

Superlenses have already been developed to overcome the diffraction limit. Metamaterials may be engineered to exhibit negative refraction, but they are inherently absorptive and narrowband. Additionally, they require close proximity between the objective and the object, which hinders its use in technical applications.

Finally, electrohydrodynamics provides means for sub-micrometer resolution in inkjet printing and also eliminate clogging problems compared to conventional nozzle-based inkjet technology.

For all the aforementioned arguments, the electrospray and superlens effect of microdroplets for laser-assited nanomanufacturing is investigated in this dissertation. This study includes investigation of electrospray as a mean of microdroplet generation, advantages of using microdroplet as nanoparticle carriers and their superlensing effect to focus a laser beam to sub-diffraction resolution and finally the implementation of this technology to realize nanodots (cluster of nanoparticles) and microlayers of semiconductor and conductive material.

CHAPTER 3
METHODS

3.1 Solution preparation

Electrospray and subwavelength focusing of a laser beam due to the superlens effect of microdroplets are combined to develop and study a new laser-assisted nanomanufacturing process for the deposition of nanoparticles into microlayers and discrete nanodots on rigid and flexible substrates. This technique has applications in the fields of microelectronics, optics, and conformal solar cells. An intermediate band solar cell based on silicon carbide (SiC) layers and silicon (Si) nanodots exceeds the Shockley-Queisser limit on the efficiency of a cell [106]. Silicon-germanium alloys are becoming an important semiconductor material for high-speed integrated circuits [107]. Zinc oxide (ZnO) can be used as the front contact for solar cells or of liquid crystal displays [108]. A metal such as silver (Ag), which exhibits the highest electrical conductivity of any metal, may be used as the metal back contact of these new solar cells.

Therefore, the experiments were conducted in this study using aqueous colloidal suspension of Si, SiC, Ge, ZnO and Ag nanoparticles and surfactant solutions without the presence of nanoparticles as listed in Table 3.1. The nanoparticle suspensions were prepared by dispersing the nanoparticles in de-ionized (DI) water and adding dispersant and surfactant to the mixture of the water and

nanoparticles. The mixtures were sonicated in a cup-and-horn-type ultrasonicator at 20 kHz for an hour. The surfactant and dispersant agents were sodium dodecyl sulfate (SDS) and sodium salt of poly-naphthalene sulfonic acid respectively. The viscosity, surface tension and electrical conductivity of the resulting suspensions were experimentally obtained using a Brookfield DVII + Pro viscometer, a SITA Dynotester bubble pressure tensiometer, and an Omega handheld conductivity tester, respectively. Table 3.1 shows the physical properties of the nanoparticle suspensions. The properties of these aqueous suspensions depend on the concentration of nanoparticle and surfactant, as it can be seen in Fig. 3.1, where the density and electrical conductivity of a suspension is presented as a function of the mass fraction as percentage by weight (wt%) of ZnO.

The nanoparticle suspensions used to conduct the experiments in this dissertation contained concentration of nanoparticles between 2 - 50 wt%. The stable suspension of these nanoparticles in DI water was attained by the help of a surfactant with concentrations between 6 - 16 mM and a dispersant agent with concentrations between 1 - 4 g/L. The average size of Si and SiC particles was 30 nm. The Ag particle size ranged between 20 - 30 nm. The average size of ZnO particles was 70 nm and the Ge particle size ranged between 0.1 - 40 μm.

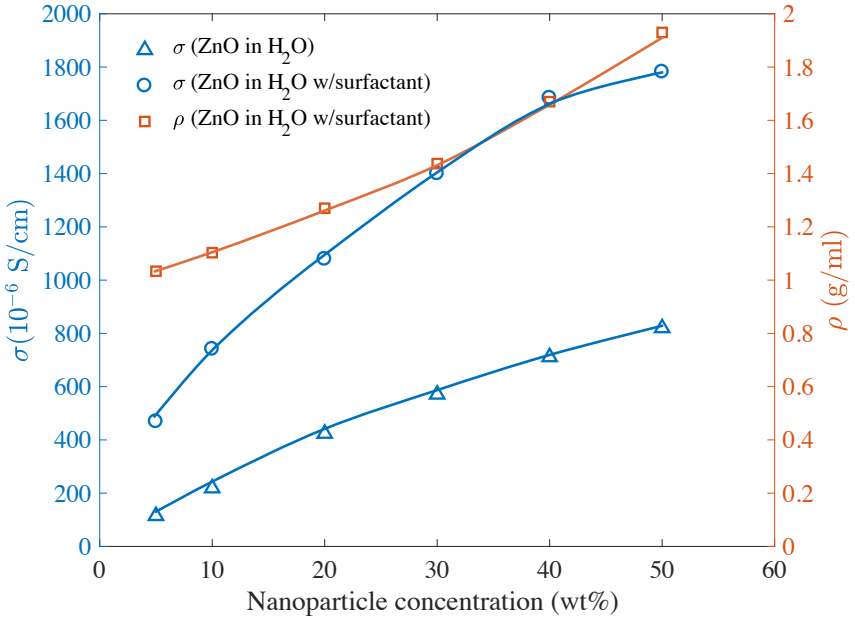

Figure 3.1: liquid density and electrical conductivity variation as a function of the mass fraction of ZnO nanoparticles in an aqueous suspension.

Liquid	Density ρ (g/ml)	Viscosity μ (10^{-3} Pa.s)	Conductivity σ (10^{-6} S/cm)	Surface tension γ (10^{-3} N/m)
Surfactant solution (SDS, 6mM)	1.000	1.08	394	53.3
Surfactant solution (SDS, 8mM)	1.000	1.10	595	49.8
Surfactant solution (SDS, 16mM)	1.000	1.13	1110.4	44.6
Si, 2 wt% in H_2O	1.010	1.48	991.6	46.7
Si, 5 wt% in H_2O	1.033	1.82	1391.6	48.2
Si, 10 wt% in H_2O	1.060	2.72	1411.2	47.1
SiC, 2 wt% in H_2O	1.051	1.56	484.0	47.7
SiC, 5 wt% in H_2O	1.127	4.79	545.0	48.5
SiC, 10 wt% in H_2O	1.193	12.05	582.0	59.9
Ge, 2 wt% in H_2O	1.023	1.36	718.2	47.2
Ge, 5 wt% in H_2O	1.064	1.56	797.8	47.5
Ge, 10 wt% in H_2O	1.130	1.95	898.4	47.6
Ge, 20 wt% in H_2O	1.263	2.77	938.0	48.0
ZnO, 10 wt% in H_2O	1.103	1.46	1141.0	45.1
ZnO, 30 wt% in H_2O	1.438	2.09	1400.0	52.4
ZnO, 50 wt% in H_2O	1.930	18.50	1782.0	54.3
Ag, 10 wt% in H_2O	1.073	1.42	938.0	46.8
Ag, 20 wt% in H_2O	1.153	1.71	1202.0	47.2

Table 3.1: Physical properties of nanoparticle suspensions in DI water.

3.2 Experimental setup

3.2.1 Electrospray of microdroplets

For the study of modes and scaling laws for electrospray of nanoparticle suspensions, the sonicated liquid was supplied at a flow rate, Q between 0.167 - 1.67 mm^3/s (10 - 100 μl/min) to a stainless steel capillary tube of inner and outer diameters 0.51 and 0.82 mm, respectively. An electrostatic field was created by applying a direct current positive voltage to the capillary, and an annular copper disk (extractor electrode) and an aluminum substrate (collector electrode) as the ground terminal as shown in Figs. 3.2 and 3.3. The inner and outer diameters and the thickness of the disk were 4.5, 38, and 0.5 mm, respectively, and the disk was coaxially situated 2 and 4 mm (H_1) below the tip of the capillary tube and 70 mm ($H_2 - H_1$) above the substrate surface. The applied voltage was varied to generate droplets from different electrospray modes, and their sizes and frequency of formation were recorded using high-speed photography (Phantom V12.1 camera). The high-speed camera and light source were aligned with the capillary and droplet ejection from the liquid meniscus. All experiments were carried out at $25 \pm 1^{\circ}$C and the system was allowed at least 30 min to reach the steady state of droplet formation before video recording any data.

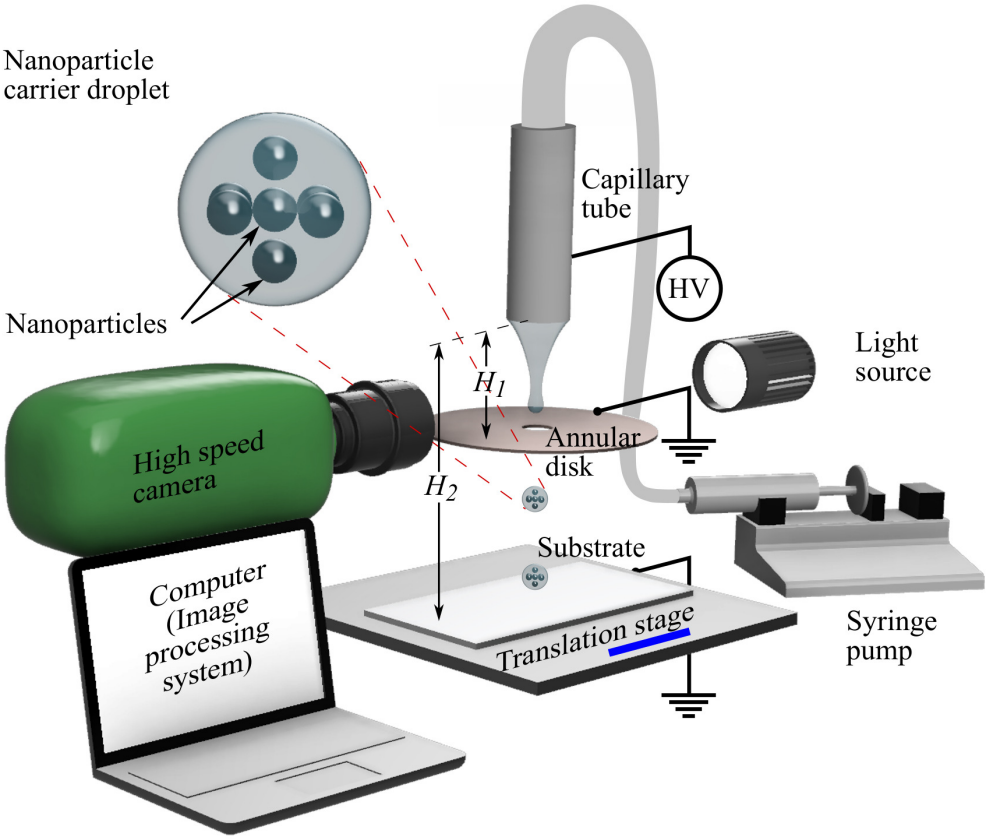

Figure 3.2: Schematic of experimental setup for deduction of droplet size and frequency of droplet formation from an electrospray.

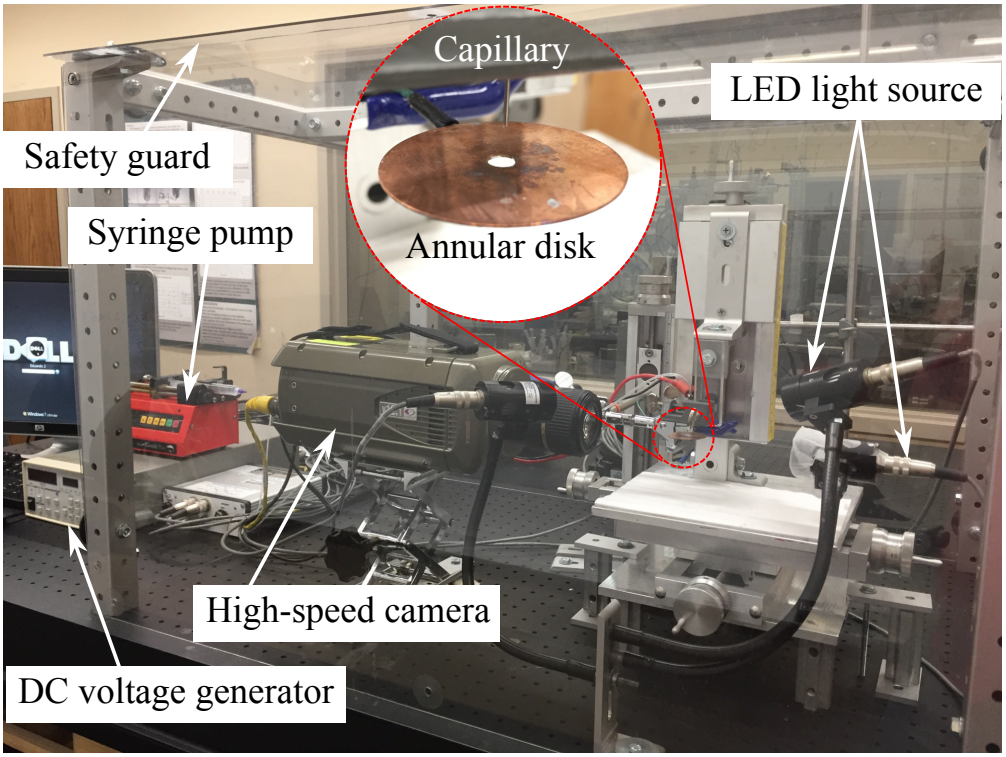

Figure 3.3: Experimental setup for deduction of droplet size and frequency of droplet formation from an electrospray.

3.2.2 Superlens effect of microdroplets

The electrospray is operated in microdripping mode to generate uniform monodisperse microdroplets at a steady rate of 320 droplets per second. The microdroplets were produced using an electrostatic field that was created by applying 3300 V between the capillary tube and the substrate as shown in Fig. 3.4. A pulsed Nd:YAG laser of wavelength 1064 nm was used as the input laser beam. An axicon lens and a biconvex lens were used to shape the Gaussian Nd:YAG laser beam to an annular cylindrical beam [109]. A hollow parabolic mirror focuses the annular cylindrical beam into an annular conical beam (laser cone) so that the diameter of the focal spot is 285 μm on the substrate surface (silicon wafer) and the apex of the laser cone interacts with the microdroplet near the substrate surface. An X-Y motorized stage was used to move the silicon substrate continuously at the speed of 0.1 mm/s during this study. The laser system was operated at the pulse repetition rate of 30 kHz and pulse length of 7 μs, and the average powers of the laser were selected as 5, 9, 13, 17, and 22 W. High-speed photography (Phantom V12.1 camera) was used for imaging the microdroplet generation, microdroplet heating process, evaporation of the liquid, and subsequent sintering of the nanoparticles. The subwavelength holes and nanofeatures were analyzed using optical profilometry (4D Technology NanoCam Sq), SEM microscopy and EDS analysis (Zeiss ULTRA-55 FEG SEM). Ultrasonication at 20 kHz for 10 min was used to clean the silicon substrate before and after the experiments. This procedure yields clean samples by removing the excess nanoparticles that are not completely sintered or any debris.

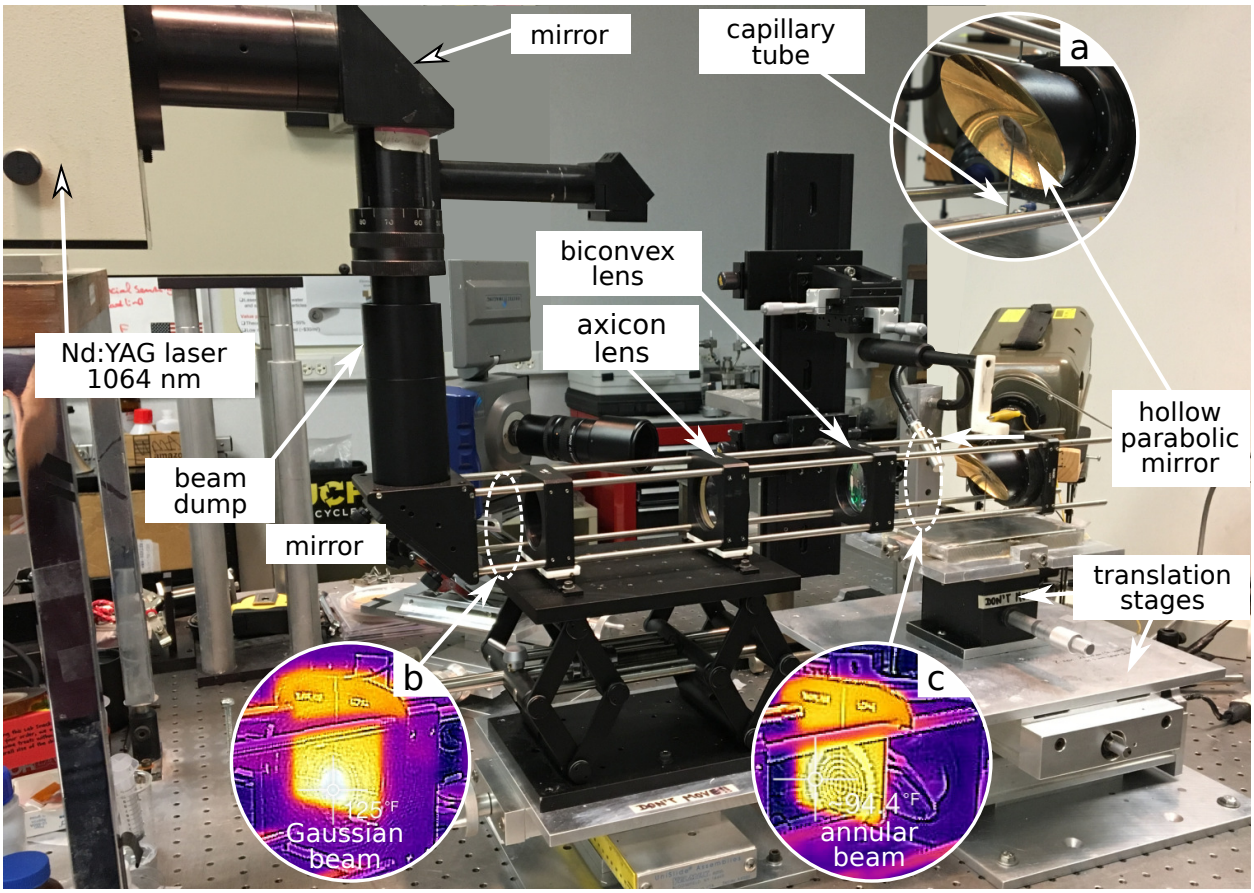

Figure 3.4: Experimental setup for investigation of superlens effect of electrospray microdroplets. (a) Alignment of the electrospray capillary with the focal point of the hollow parabolic mirror. (b) Infrared thermography of the Gaussian beam produced by the Nd:YAG laser. (c) Infrared thermography of the laser beam after it has been converted into an annular cylindrical beam.

3.3 Calculation of droplet size and frequency of droplet formation

For the measurement of the droplet size and the frequency of droplet formation, videos of 512 x 1024 pixels (spatial resolution of 5.5 μm/pixel) were recorded at different frame rates depending on the mode being recorded. The dripping, microdripping, and oscillating microdripping modes were recorded at 2000, 8000 and 11000 fps respectively. In general, 670 frames were captured at each applied voltage. Thus, each video records the ejection of several droplets. In addition, the entire set of experiments (i.e., $0 \leq \phi \leq 5000$V) was repeated at least three times for each nanoparticle suspension including the surfactant solution.

Using the video data, the volume of the droplets was calculated by image processing [110, 111]. Since the shape of the droplets was not perfectly spherical and varied with time during their free fall, a Riemann sum, i.e., the sum of slices of 1 pixel each, was used to compute the volume, $\forall = \sum_{i=1}^{N} \pi r^2$, under the assumption that the falling droplet is axisymmetric at all instances. Here, r_i is the radius of the i^{th} slice. The radius of each droplet was then determined as $r = \sqrt[3]{3\forall/4\pi}$. Finally, the average radius of the droplet was calculated as the mean value and its standard deviation was used to compute the uncertainty in the measurements.

The frequency at which the liquid meniscus oscillates at the tip of the capillary tube, i.e., the frequency of droplet formation was determined using the video image that recorded the growth of the meniscus apex as a function of time as shown in Fig. 3.5. The Fig. 3.5a represents the periodic stretching and contraction of the apex of the conical meniscus in the microdripping mode with the apex stretching to a fixed length at the time interval of approximately 3.2 ms. Two periods are

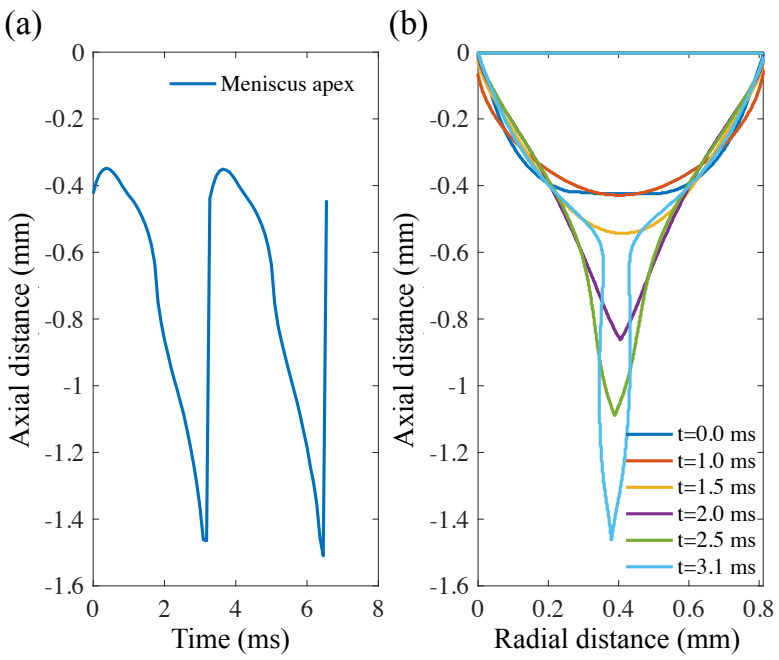

Figure 3.5: Image processing of meniscus contour. (a) Meniscus apex location as a function of time of electrospray operating in microdripping mode (Si, 5 wt% in H_2O, H_1 = 4 mm, ϕ = 4000 V). (b) Sequence of the meniscus contour of microdripping mode corresponding to case used in (a).

shown which consist in the formation of two monodisperse microdroplets at the time, $t = 3.1$ ms and $t = 6.4$ ms. Fig. 3.5b shows the deformation of the meniscus with the apex moving vertically at a fairly high speed of nearly 0.6 m/s, indicating that microdroplets can be dispensed at a high rate to deliver nanoparticles for high-speed manufacturing.

3.4 Calculation of diffraction-limited focal spot size

The focal spot size and focal length of the droplet lens can be estimated by assuming the nearly spherical droplets as a ball lens [112]. The effective focal length (FL_B) depends on the diameter of the lens and its refractive index. The FL_B is measured from the center of the lens. While the back focal length BFL_B is measure from the surface of the lens.

$$FL_B = \frac{n_l 2r}{4(n_l - 1)} \tag{3.1}$$

$$BFL_B = FL_B - r \tag{3.2}$$

where n_l and r are the refractive index and the radius of the lens, respectively. The numerical aperture (NA) is defined by the following equation,

$$NA = n_m \sin\theta \tag{3.3}$$

where n_m and θ are the refractive index of the medium and the maximal half-angle of the cone of light that can enter or exit the lens.

For the collimated incident laser and air surrounding the droplet ($n_m = 1$), the numerical aperture depends on the size of the lens, i.e., the diameter of the droplet ($2r$), the refractive index of the liquid droplet (n_l), and the diameter of the input source (D_{is}).

$$NA = \frac{1}{\sqrt{1 + 4\left(\frac{n_l 2r}{4D_{is}(n_l - 1)}\right)^2}} \tag{3.4}$$

Light of wavelength λ, traveling in a medium with refractive index n_m and converging to a spot with half-angle θ produces a spot with radius,

$$FS_B = \frac{\lambda}{2n_m \sin\theta} \tag{3.5}$$

Therefore, for the case analyzed here, i.e., droplets traveling through the laser cone in air and diameter of laser input source larger than that of the droplet, the focal spot size can be estimated by Eq. (3.6). Table 3.2 shows the focal length and the diffraction-limited focal spot of microdroplets when they act as spherical lenses.

$$FS_B = \frac{\lambda}{2}\sqrt{1+\frac{1}{4}\left(\frac{n_l}{n_l-1}\right)^2} \tag{3.6}$$

The multiple curved surfaces produced by nonuniform heating are assumed as a cluster of individual lenses for the calculation of the focal spot size. Photographs of the laser-droplet interaction (Fig. 3.6a) are used to extract the outer air-liquid interface by using image processing in Matlab (Fig. 3.6b). In order to get the radius of curvature and diameter of the entrance of light of each lens, image processing was employed. A total of fifty vertices were extracted from the binary image (see green contour in Fig. 3.6b). Next, a polygon is fitted with these vertices. The curvature (k) of each vertex of the polygon is calculated by using its neighboring vertices (left and right neighbor) along with the entrance of light (l_e), which is assumed as the distance between the left and right neighbor. Finally, the radius of curvature of each curved surface is the reciprocal of the curvature ($1/k$). The set of radii of the curved surfaces obtained from this method produces negative, positive and infinity large radii. Thus, the curved surfaces act as convex lenses, concave lenses and flat surfaces of infinite radius. Only the finite convex radii are used for the calculations since they are the only

Liquid	wavelength λ (nm)	refractive index n_l	droplet radius r (μm)	focal length FBL_B (μm)	focal spot FS_B (nm)
Ge, 0 wt% in H_2O	1064	1.324	36.3	38	1210
Ge, 2 wt% in H_2O	1064	1.337	38.1	38	1183
Ge, 5 wt% in H_2O	1064	1.356	37.9	34	1144
Ge, 10 wt% in H_2O	1064	1.391	37.7	29	1085
Ge, 20 wt% in H_2O	1064	1.471	37.5	21	986
Si, 5 wt% in H_2O	1064	1.380	39.8	32	1102
Si, 20 wt% in H_2O	1064	1.571	40.3	15	905

Table 3.2: Geometrical focusing of microdroplets acting as spherical lenses.

surfaces that focus the incoming laser onto the substrate. Fig. 3.6c shows the calculation procedure. Lines protruding from the contour denote the normal to each curved surface. Lines of red color are used for convex surfaces, representing the convergence of the laser radiation in a given direction. Lines of blue color are used for concave surfaces, which will diverge or defocus the laser radiation. The length of each line is proportional to the curvature (k) and inversely proportional to the focal length (FL_G).

The height of droplets on the solid surface is in the order of tens of microns for most of the cases in this study. Fig. 3.6c shows a maximum height and maximum spread diameter of approximately 50 μm and 300 μm, respectively. The radii of curved surfaces are in the range of 1.1 - 42.3 μm.

The focal length can be calculated from the Gaussian lens formula [63],

$$FL_G = (n_l - 1)\left(\frac{1}{R_1} - \frac{1}{R_2} + \frac{(n-1)b}{n_l R_1 R_2}\right) \tag{3.7}$$

where FL is the focal length, b is the thickness of the lens, R_1 is taken as $1/k$ and $R_2 = \infty$ for the planar surface at the bottom of the droplet. Finally, the focal spot size can be estimated as,

$$FS_G = \frac{\lambda}{2n_l \sin\left(\tan^{-1}\left(\frac{l_e}{2FL_G}\right)\right)} \tag{3.8}$$

Figure 3.6d shows a histogram of the frequency of curved convex surfaces and their corresponding focal spot size for the case shown in c. The minimal focal spot size calculated is approximately 400 nm for a laser with wavelength 1064 nm. The value of focal spot sizes ranges between 400 - 510 nm with focal lengths between 3.2 - 12.2 μm. Section 5.2 will discuss the superlensing effect of microdroplets and how focal spots significantly smaller than those produced by these curved surfaces, as well as those listed in Table 3.2 may be achieved.

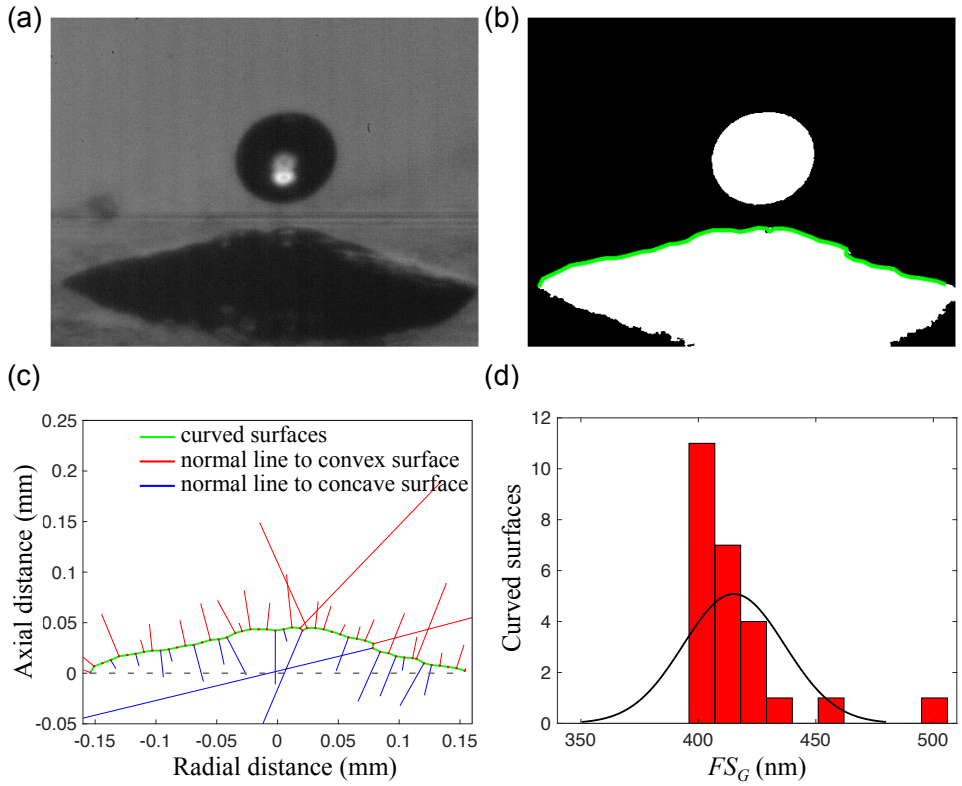

Figure 3.6: (a) Photograph of the curved surface of a droplet due to nonuniform heating. (b) Extraction of the contour of the curved surface from a binary image. (c) Calculation of line curvature of an approximated polygon. (d) histogram of the frequency of curved convex surfaces and their corresponding focal spot size.

CHAPTER 4
MODES AND SCALING LAWS FOR ELECTROSPRAY OF NANOPARTICLE SUSPENSIONS

4.1 Introduction

The printing or deposition of the semiconductor materials requires a steady supply of a fixed amount of nanosuspension, which is achieved by driving the suspension through a nozzle. This can be performed by using conventional techniques based on piezoelectric devices [113, 99]. Electrohydrodynamics (EHD) is another promising technique to achieve sub-micrometer resolution in jet printing and also eliminate the clogging problem compared to conventional nozzle-based inkjet technologies [5]. These advantages are due to the unique process physics in electrospray for producing droplets of diameters smaller than the orifice of the nozzle, since the droplets can be formed and ejected from the apex of a conical meniscus instead of the tip of the nozzle. To implement this technique in practice, however, the process physics need to be understood and the technical challenges have to be overcome. Some of these problems are difficulties in preparing the nanosuspensions, uniformity, and stability of the suspensions, optimizing their thermomechanical and electrical properties, nonuniformities in the printed microstructures due to coffee-ring effects, and early stages of research in semiconductor printing.

Electrospray of nanoparticles provides a convenient way of producing nanoparticle patterns. In this technique, nanoparticles are dispersed in water with an appropriate surfactant, which readily produces a viscous suspension called nanoink, and this nanosuspension can become increasingly viscous at high concentrations [114, 115, 116]. Deposition of nanoparticles using this ink in electrosprays can promote the fabrication of a variety of energy and electronic devices such as conformal solar cells, sensors, and actuators. This novel nanoparticle dispensing technique can also be used to fabricate masks for nanolithography, nanopillar arrays for photonic crystals, and nanodot arrays for plasmonic surfaces. Electric field-driven microdroplets can be used for thin film deposition [29, 30], drop-on-demand printing [31], and microencapsulation [54, 55, 56].

Electrospraying of semiconductor materials has been studied in recent years for depositing thin films, such as copper-indium-diselenide films for solar cell [7], ZnO-based thin film transistors [6], etc. as it was described in section 2.2.2 of Chapter 2. However, the effect of various properties of the nanosuspensions, such as viscosity, surface tension, and electrical conductivity, on the mode of droplet formation needs to be studied to understand the stable operation of the EHD process for practical applications.

Direct printing of semiconductor materials using electrospray has the potential to significantly lower the cost of producing semiconductor devices compared to the conventional multistep method of photolithography and chemical processing. Two major steps in the new electrohydrodynamics (EHD) method are printing and solidification [96]. This Chapter presents the research done on the conical meniscus regime that appears following the dripping mode and generates the microdripping mode at low flow rates. The objective of this Chapter is to delineate the transition of these modes,

as well as the determination of the size of droplets and frequency of droplet formation from an electrospray operated in microdripping mode.

4.2 Electrospray mode transition of microdroplets with semiconductor nanoparticle suspension

Electrosprays operate in several modes depending on the flow rate and electric potential. This allows the generation and deposition of droplets containing nanoparticles into discrete arrays when an appropriate electrospray mode is employed. This section focuses on the delineation and transition of electrospray modes when microdroplets are loaded with semiconductor nanoparticles. This is achieved by studying several nanosuspensions at low viscosity and high electrical conductivity.

The electrospray generates microdroplets carrying nanoparticles at desired concentrations and deposits a wet layer on the substrate, which can be subsequently evaporated to produce thin films or discrete array of nanodots. In electrosprays, the detachment of droplets from the tip of a capillary tube occurs due to the balance of the electrodynamic and surface tension forces acting on the fluid. An electrostatic field between the capillary tube and an extraction electrode (Fig. 3.2) in the vicinity of the tube alters the mode of detaching the droplets, resulting in different fluid behavior such as dripping, microdripping, spindle, multispindle, and cone-jet spray mode [34, 10, 40, 117]. Thus, the electro-capillary interaction provides an additional mechanism to generate different modes for the fluid dynamic response of the droplets.

The electrical conductivity and the flow rate of the liquid affect the droplet diameter [45, 8, 9, 118]. This is due to the fact that the electrical conductivity of the nanosuspension affects the cone geometry by inducing electrical tangential stresses [119, 120]. The presence of semiconductor nanoparticles inside the droplets, particularly the electrical conductivity of the nanomaterials, will influence the transition of the microdroplet modes. This is because the polarizable materials can interact with the electrostatic field more energetically than the aqueous liquid medium itself. In addition, the viscosity affects the shape of the cone by resisting its deformation and thus promotes a stable cone-jet spray mode. A fluid of higher viscosity also has the additional advantage of decreasing the jet diameter [121, 122]. The nanosuspensions used in this study are listed in Table 4.1. These liquids were selected for their high conductivity and low viscosity but with a reasonable variation in surface tension. The Reynolds number is calculated as $Re = \rho u_c R_i / \mu$, where, ρ, u_c, R_i, and μ are the density of the fluid, the characteristic velocity, the inner radius of the capillary tube at the tip, and the viscosity of the fluid. Experiments were carried out at low Reynolds numbers to investigate the modes of nanosuspensions in laminar electrospray of droplets.

4.2.1 Experimental results

Different electrospray modes, such as dripping, microdripping, and oscillating microdripping were observed, as shown in Fig. 4.1. In all modes, the gravity and electric fields stretch the meniscus downward while the surface tension force and viscous force oppose the stretching. In the dripping mode (Fig. 4.1a), the droplets are formed from a hemispherical or ellipsoidal meniscus at the tip

of the capillary tube, whereas the field-induced stretching of the fluid creates a conical meniscus in the other modes (Fig. 4.1b,c). The electric field stretches these cones to a critical dimension and pinches off the elongated liquid filament that subsequently deforms into a spherical droplet to achieve a state of minimum surface energy. In the dripping mode, a small secondary droplet can be observed above each large droplet (Fig. 4.1a). This tiny droplet is formed due to the stretching at the neck between the meniscus and the large droplet. The neck detaches as an isolated narrow liquid filament that eventually reshapes into the secondary spherical droplet. In each mode, the meniscus goes through a sequence of deformation to produce the droplets as shown in Fig. 4.1, and the sequence repeats after the detachment of the droplets. As a reference time for this type of periodic sequence, $t = 0$ refers to the time at which the first meniscus shape is formed in the dripping mode (Fig. 4.1a), microdripping mode (Fig. 4.1b), and oscillating microdripping mode (Fig. 4.1c).

In the microdripping mode, the conical meniscus is axisymmetric with the tip of the cone on the axis of the capillary tube, and spherical droplets are vertically ejected toward the substrate through the annular copper disk electrode. A stable mechanism is established in this mode, which produces a steady stream of uniform microdroplets (Fig. 4.1b) that drop in the vertically downward direction. This mode is, therefore, suitable for depositing discrete arrays of nanodot, which is a cluster of nanoparticles, to produce advanced optoelectronic and microelectronic devices at a high speed. As the voltage is increased, the cone-tip oscillates in a plane around its axisymmetric position like a pendulum (Fig. 4.1c), and microdroplets are ejected from the cone-tip when the tip is at the circumference of the meniscus. The frequency of these oscillations varies from 150

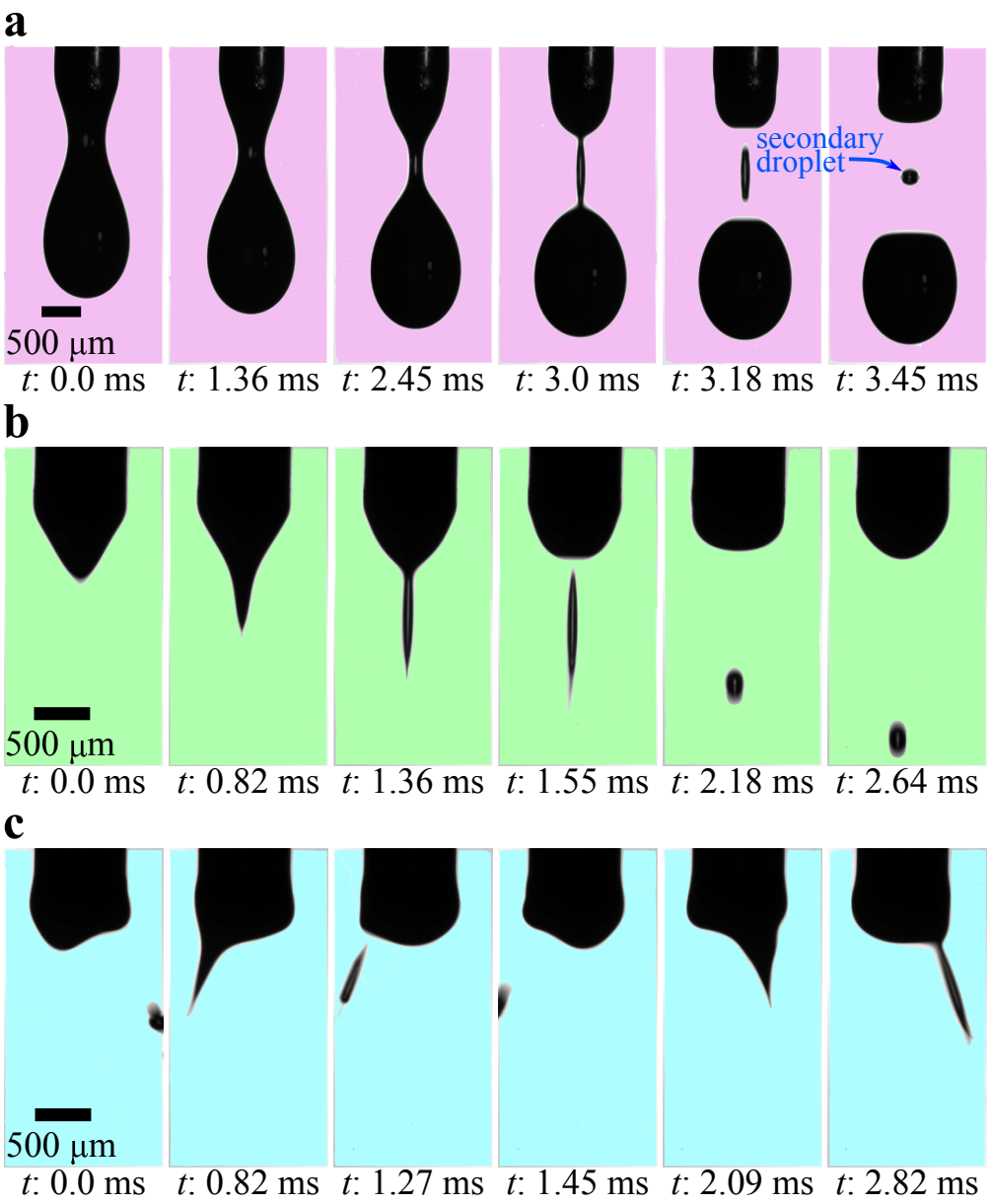

Figure 4.1: Droplet formation from the capillary tube under the action of an electric field. (a) Dripping mode of Si, 5 wt% in H_2O ($H_1 = 4$ mm, $\phi = 2.5$ kV, and $Q = 1.67$ mm^3/s). The main droplet is formed along with a secondary droplet. (b) Microdripping mode of Si, 5 wt% in H_2O ($H_1 = 4$ mm, $\phi = 4$ kV, and $Q = 1.67$ mm^3/s). Uniform monodisperse droplets are generated from the conical meniscus. (c) Oscillating microdripping mode of Si, 5 wt% in H_2O ($H_1 = 4$ mm, $\phi = 5$ kV, and $Q = 1.67$ mm^3/s,). The conical meniscus oscillates in a plane ejecting drops in two directions.

Liquid	$^{(e)}r_0$ (mm)	u_c (m/s)	ε_r	Re	Ca	Bo
Surfactant solution (SDS, 16mM)	1.21	0.267	1.08	61.21	0.029	0.222
Si, 2 wt% in H_2O	1.18	0.278	1.07	49.12	0.035	0.202
Si, 5 wt% in H_2O	1.19	0.278	1.10	41.09	0.031	0.204
Si, 10 wt% in H_2O	1.13	0.273	1.11	27.61	0.083	0.209
SiC, 2 wt% in H_2O	1.19	0.277	1.04	38.29	0.048	0.203
SiC, 5 wt% in H_2O	1.19	0.267	1.04	14.48	0.139	0.220
ZnO, 10 wt% in H_2O	1.29	0.292	1.09	24.25	0.041	0.190

Table 4.1: Relevant parameters of nanoparticle suspensions in DI water.

$^{(e)}$Drop radius in the absence of electric field (i.e. $E = 0$) from experiements.

Hz for ZnO, 10 wt% suspension to 250 Hz for Si, 2 wt% suspension. Consequently, the droplets are obliquely directed toward the substrate in two different directions. At low electric fields up to the microdripping mode, the electric energy is sufficiently low and the liquid molecules and nanoparticles in the meniscus are polarized in a regular pattern aligned in the vertical direction, resulting in a stable symmetric meniscus that produces a steady vertical stream of droplets. As the electric field increases, the polarized energy in the liquid molecules and nanoparticles increases and these polarized states interact with each other, resulting in an unstable asymmetric meniscus that creates the oscillating microdripping mode.

Figure 4.2 shows the size distribution of ejected droplets for the nanosuspension of 5 wt% SiC in DI water in the microdripping (Fig. 4.2a) and the oscillating microdripping (Fig. 4.2b) modes respectively. It can be seen that the average radius of the droplets, which is computed as the mean value, is larger for the microdripping mode (102 μm) than for the oscillating microdripping mode (63 μm). However, the microdroplets are produced with a very narrow standard deviation of 9 μm in the former mode compared to the relatively large standard deviation of 43 μm in the latter mode. The average radii of droplets are shown in Fig. 4.3a with the corresponding uncertainty in the measurements for different nanosuspensions and different voltages up to 5 kV applied to the capillary tube. Two sets of data in the literature [10, 123] are also provided in Fig. 4.3b. The average droplet size decreases as the applied voltage increases. An increase in the electric field due to increasing voltage causes breakage and subsequent fragmentation of the droplet when the electric field is sufficiently large, which causes a reduction in droplet radius. Although the drop size decreases with increasing voltage, the size distribution will broaden as shown in Fig. 4.2 and

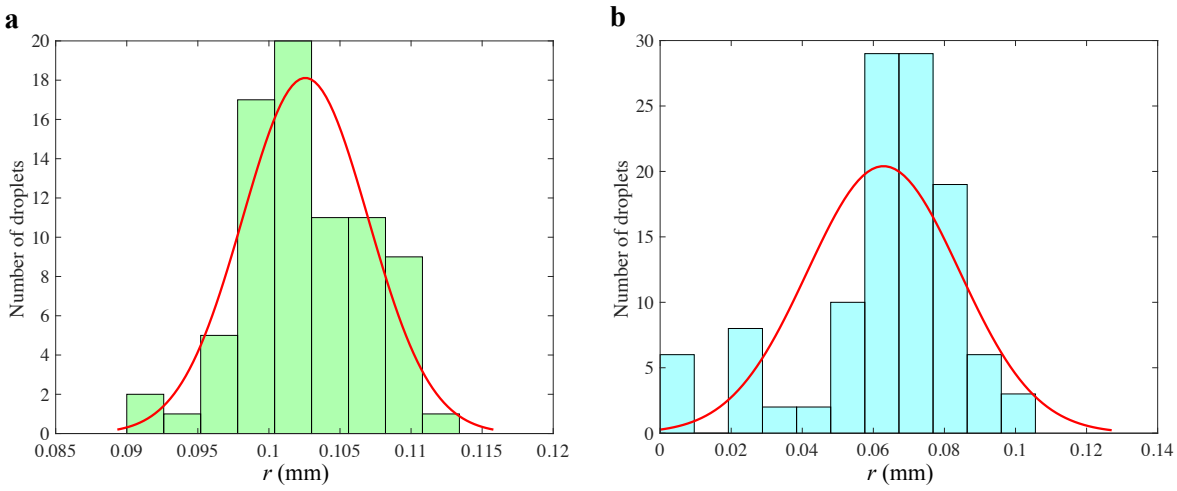

Figure 4.2: Example of size distribution of ejected droplets. (a) Histogram of the radius of ejected droplets for SiC, 5 wt% in H_2O in microdripping mode ($H_1 = 2$ mm, $\phi = 3$ kV, and $Q = 1.67$ mm^3/s). (b) Histogram of the radius of ejected droplets for SiC, 5 wt% in H_2O in oscillating microdripping mode ($H_1 = 2$ mm, $\phi = 4.5$ kV, and $Q = 1.67$ mm^3/s). The modes are color coded corresponding to Fig. 4.1.

the electric repulsion between ejected droplets will become significant. The region between the dripping and microdripping modes is a mixed mode regime where either large or small diameter is possible depending on the nanosuspensions. However, for all suspensions, microdripping occurs after this mixed mode, which highlights the importance of knowing the characteristic voltage at which microdripping occurs.

It should be noted in Fig. 4.3a that the drop size for different suspensions spreads over a wide band as a function of voltage. The spread in the data can be collapsed into a single curve as a function of a nondimensional parameter called the electric capillary number, Ca_e [124, 125]. The data

in both Figs. 4.3a and 4.3b are fitted into a single curve in Fig. 4.4, i.e., $Ca_e = E^2\varepsilon_0\varepsilon_r R_o/\gamma$, where E, ε_0, ε_r, R_o, and γ are the externally applied electric field, the electrical permittivity of vacuum, characteristic relative permittivity for each aqueous suspension, the outer radius of the capillary tube, and the surface tension of the suspension respectively. The characteristic relative permittivity is defined as $\varepsilon_r = 1 + \sigma/\varepsilon_0\omega$ based on the Lorentz model for the interaction of electromagnetic waves in dielectric materials [126], where σ is the electrical conductivity of each aqueous suspension and ω is a characteristic frequency taken as c/L where c and L are the speed of light in air and the distance from the center of the capillary tip to the inner edge of an annular disk electrode.

The expression for E in Ca_e was determined as $E = E_1 + E_2$ for the three-electrode system of this study by superposition of solutions. E_1 is the electrostatic field between the capillary tube and the disk, and E_2 is the electrostatic field between the tube and the substrate. The tube was connected to the positive polarity, and the disk and substrate were connected to a ground terminal. E_1 was determined using $E_1 = \sqrt{2}\phi/R_o ln(4H_1/R_o)$, and E_2 using $E_2 = \sqrt{2}\phi/R_o ln(4H_2/R_o)$, where ϕ is the electric voltage and H_2 is the distance from the center of the tip of the capillary tube to the substrate. Note that Jones and Thong [127] derived the expression of the electrostatic field for a two-electrode system consisting of a thin cylinder with rounded tip of positive polarity and a large semi-infinite solid as the ground terminal and, therefore, $E = E_2$ for the droplets produced by the two-electrode system [10]. The electric capillary number varies in the range $0 \leq Ca_e \leq 6$ for the cases analyzed in this study.

The droplet radii of different types of suspension are found to follow a unique trend as a function of the electric capillary number (Fig. 4.4) for a given flow rate of the suspension through

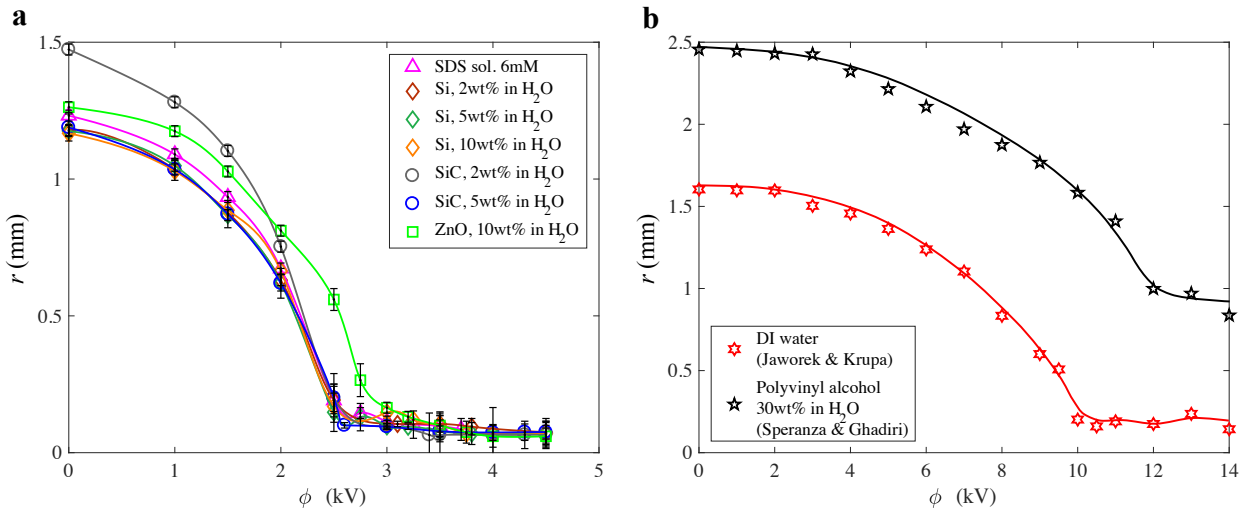

Figure 4.3: Droplet size vs applied electrical voltage. (a) Markers represent the average droplet radius as a function of the applied voltage between the capillary tube and the earthed electrodes ($H_1 = 2$ mm and $Q = 1.67$ mm^3/s). Error bars show the uncertainty of the measurements with a confidence interval of 95%. Solid curves are produced by curve fitting the experimental results. (b) Other investigators' data. Jaworek & Krupa's results (red stars) are adapted from their Fig. 3a. Speranza & Ghadiri's results (black stars) correspond to their electrode configuration C. Solid curves are produced by curve fitting the experimental data.

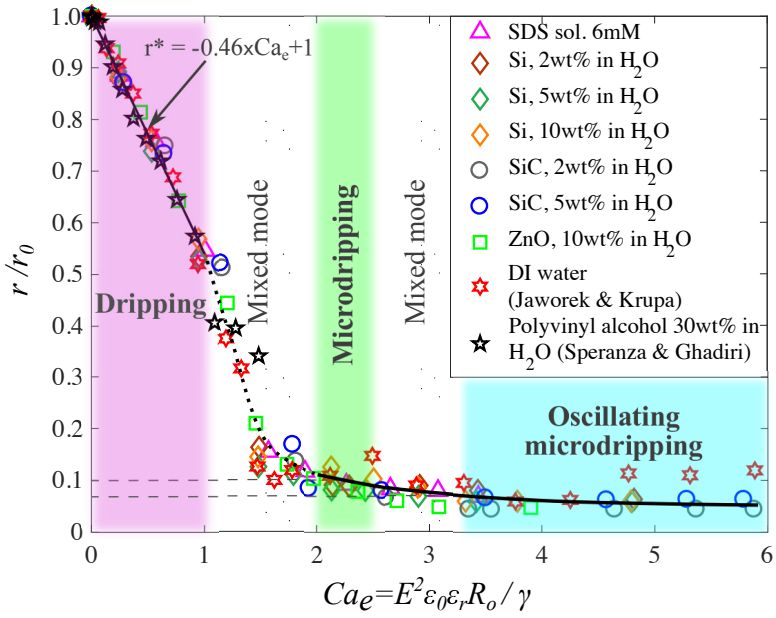

Figure 4.4: Dimensionless size of droplets vs electric capillary number. Results from Figs. 4.3a and 4.3b are nondimensionalized with respect to the droplet radius in the absence of electric field and displayed as a function of the electric capillary number. Transition between dripping and microdripping modes occurs at $Ca_e \approx 1.0$ and the transition between microdripping and oscillating microdripping modes occurs at $Ca_e \approx 2.5$. The modes are color coded corresponding to Fig. 4.1.

the capillary tube. The effect of the inertial force is neglected since the flow rate is very low and the densities of the aqueous suspensions and velocities are of the same order (Table 3.1 and 4.1). Fig. 4.4 clearly classifies the transition of droplet modes into two basic regimes: ellipsoidal and conical meniscus regimes based on the shape of the meniscus at the tip of the capillary tube. While ellipsoidal meniscus causes the dripping mode, the conical meniscus produces microdripping and oscillating microdripping modes depending on the electric capillary number.

The mechanism of droplet formation in the EHD process depends on the electrical and gravity forces, which tend to detach the droplets from the meniscus, and the surface tension and viscous forces that resist the detachment of the droplets. The relative influence of these forces on the droplet size is determined by the nondimensional parameters: electric capillary number ($Ca_e = E^2\varepsilon_0\varepsilon_r R_o/\gamma$), Capillary number ($Ca = \mu u_c/f\gamma$), and Bond number ($2r_0^2\rho g/3\gamma$), each appearing as a ratio of the respective force to the surface tension force (it will be discussed in detail in section 4.3). In the dripping mode, the viscous effects are negligible for the fluids tested in this study. Therefore, the nondimensional radius of droplets, r^*, can be modeled as a linear function of Ca_e with slope m in the dripping mode, such as $r^* = 1 + mCa_e$ which satisfies the condition $r = r_0$ when the electric field E or the electric capillary number Ca_e is zero. Since the maximum value of r^* is 1, the slope m will be negative which is empirically found to be $m = -0.46$ from Fig. 4.4 in the range $0 \leq Ca_e \leq 1$. Consequently, the expression for r^* is, $r^* = 1 - 0.46Ca_e$ in this mode. All the liquids of this study are observed to be in the dripping mode up to $Ca_e = 1$ at which point the electrical and surface tension forces are exactly balanced. Also at this point, the radius r^* reduces from 1 to approximately 0.5 which corresponds to approximately 1 to 0.5 mm. This mode is, however,

observed in the region slightly after $Ca_e = 1$ for certain suspensions such as SiC 2 wt%, SiC 5 wt%, and ZnO 10 wt%, and a new mode called the microdripping mode appears slightly before $Ca_e = 2$ for the suspensions Si 2 wt%, Si 5 wt%, and Si 10 wt%. This region of $1 \leq Ca_e \leq 2$ is designated as the "mixed mode" region in this study since both the dripping and microdripping modes coexist in this region with the droplet radius varying approximately from 0.5 mm to 0.1 mm. The scaling law of Fig. 4.4 also conforms to other investigators' data using low conductivity liquids such as DI water without any suspension [10] and 30 wt% polyvinyl alcohol in water [123].

Immediately after the mixed mode region, the conical meniscus regime is observed with the microdripping mode occurring first, followed by oscillating microdripping mode with an increase in Ca_e. In addition, all the suspensions of this study exhibited the microdripping mode over a narrow range $2 \leq Ca_e \leq 2.5$. The droplet radius varies from $0.1r_0$ to $0.07r_0$ corresponding to approximately 100 μm to 70 μm for a flow rate of 1.67 mm^3/s (100 μl/min), which indicates that the drop size is nearly constant. However, the velocity of the droplets is larger than in the dripping mode and, therefore, the viscous effects are expected to be significant in the microdripping mode. Although the viscous effects are not perceptible for r^* in Fig. 4.4, they are found to influence the frequency of droplet formation as shown in Figs. 4.5 and 4.6. In the region $2.5 \leq Ca_e \leq 3.3$, the microdripping mode is observed at slightly after $Ca_e = 2.5$ for certain suspensions, such as SiC 2 wt%, SiC 5 wt%, and ZnO 10 wt%, and a new mode called the oscillating microdripping mode appears slightly before $Ca_e = 3.3$ for the suspensions Si 2 wt%, Si 5 wt%, and Si 10 wt%. This range of Ca_e is, therefore, designated as the second mixed mode region where either microdripping or oscillating microdripping mode can be observed depending on the suspension.

The transition between any two modes is based on the shape of the meniscus at the tip of the capillary tube, particularly the ellipsoidal and conical shapes observed during the experiments in this study (Fig. 4.1). The ellipsoidal meniscus causes the dripping mode in which the gravity and surface tension forces are dominant and the effect of the electric field is relatively low. The conical meniscus produces microdripping and oscillating microdripping modes in which the electric field and surface tension forces are dominant and the effect of the gravity force is relatively low. Since the size of ejected droplets is significantly affected by the shape of the meniscus, the transition to microdripping is noticeable by a change in the slope of the r^* versus Ca_e data. This type of change in the slope is gradual in Fig. 4.4 at the transition boundaries of the microdripping and oscillating microdripping modes since the variation in the radii of the droplets is very small between these modes. However, the transition boundaries between the microdripping, second mixed mode, and oscillating microdripping regions were discerned by observing the changes in the shape of the meniscus as presented in Fig. 4.1. Based on the experimental observation, the oscillating microdripping mode was observed beyond $Ca_e \approx 3.3$ for all the nanosuspensions tested in this study. The mechanism of mode transition is a complex physical process involving various electrohydrodynamic forces and the meniscus instability.

This type of mode-shifting at higher voltages can be attributed to two effects: (i) The electrostatic field interacts with the materials of low and high conductivities, such as dielectrics, polar surfactant molecules, n-type and p-type semiconductors and metals, differently due to their difference in polarizability. The distributions of the polarized nanoparticles and polar liquid molecules are expected to be asymmetric in the azimuthal direction since the nanoparticles and the molecules

do not need to be distributed symmetrically in the original suspension. The effect of this asymmetric distribution becomes significant when the electric field increases, giving rise to asymmetric force components to induce the oscillating microdripping mode; and (ii) The repulsive Coulomb force between charged particles produces tangential stress on the conical surface of the meniscus.

More polarization energy is stored in the meniscus at higher voltages and, therefore, smaller droplets are formed so that the total mechanical energy, i.e., the surface formation energy, of all the droplets balances the electrical energy. Figure 4.4 also shows that the droplet size does not change significantly at higher values of Ca_e, which indicates that the droplets have reached a state at which maximum surface energy is stored in each droplet. The critical radius in this study refers to the radius at which the microdripping mode begins. From Fig. 4.4, this critical radius is $r^* = 0.1$ that occurs at $Ca_e \approx 2$ for all the semiconductor suspensions at a flow rate of 1.67 mm^3/s.

An increase in the applied voltage will increase the frequency of droplet formation, N_d, i.e., the number of droplets produced per unit time, at higher electric fields as evident in Fig. 4.5. The frequency of droplet formation, which is plotted as a function of the applied voltage in this figure, spreads over a wide band for a given voltage. To examine the effect of Ca_e on the droplet formation frequency bandwidth, the nondimensional frequency of droplet formation is presented in Fig. 4.6 as a function of Ca_e. Since the viscosity, as well as other parameters such as the flow rate and density of the liquid, affect the frequency of droplet formation, the capillary number (Ca) is used to parametrize the data. A nondimensional frequency of droplet formation is defined as $(N_d R_i^3/Q)^{1/3}$, where Q is the volumetric flow rate. In Fig. 4.6, for a given Ca_e, the frequency of droplet formation decreases as Ca increases. The 5 wt% SiC nanoparticle suspension, which has

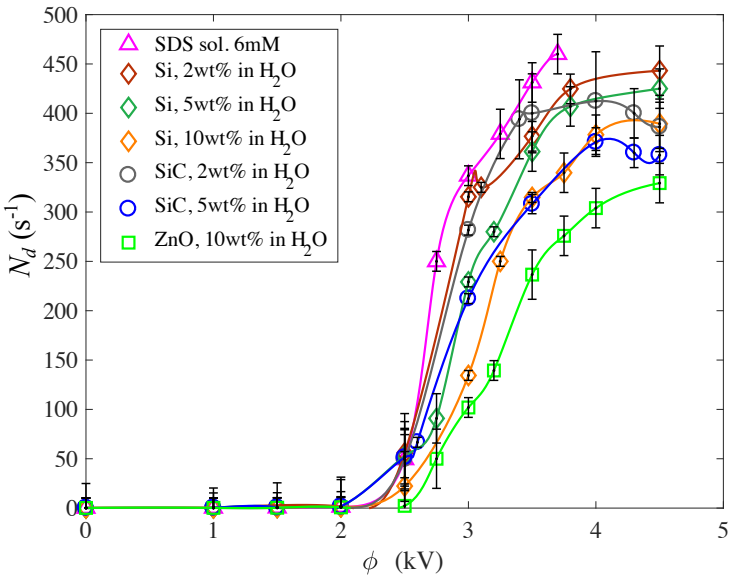

Figure 4.5: Frequency of droplet formation vs applied electric voltage. Markers represent the average frequency as a function of the applied voltage between the capillary tube and the earthed electrodes ($H_1 = 2$ mm and $Q = 1.67$ mm^3/s). Error bars show the uncertainty of the measurements with a confidence interval of 95%. Solid curves are produced by curve fitting the experimental data.

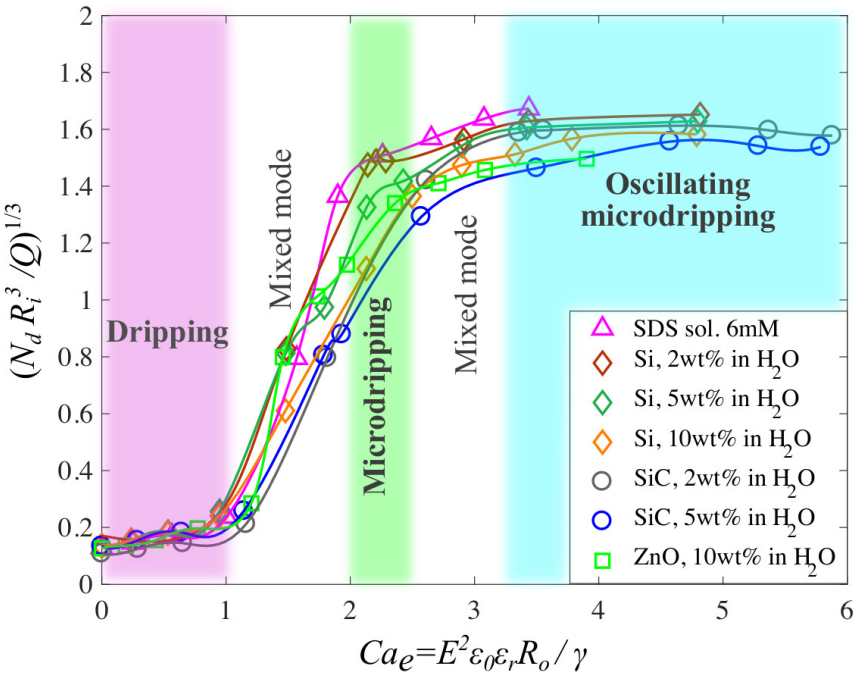

Figure 4.6: Dimensionless frequency of droplet formation vs electric capillary number. The frequency changes abruptly at the transition between dripping and microdripping mode. Fluids with high capillary number tend to have lower frequency at a given electric capillary number due to viscous effects. The modes are color coded corresponding to Fig. 4.1.

the highest Ca yields the lowest frequency of droplet formation. On the other hand, the 16 mM SDS solution, which has the lowest Ca yields the highest frequency of droplet formation. This trend in the frequency of droplet formation is due to an increase in viscosity (i.e. increase in the nanoparticle concentration) that dampens the growth of perturbations within the cone [82]. Thus viscosity delays the breakage of the meniscus in the microdripping and oscillating microdripping modes due to strong bonding of the liquid molecules and nanoparticles. However, viscosity does not affect the droplet size significantly in the dripping mode as shown in Fig. 4.4 where the data are plotted as a function of Ca_e which is independent of viscosity. This means that the viscous effects become more significant in affecting the dynamics of the conical meniscus.

In summary, therefore, modes of nanosuspensions containing semiconductor nanoparticles have been studied in laminar electrospray of droplets. A suitable microdripping mode has been observed, which can be utilized for depositing monodisperse microdroplets via electrospray. Fig. 4.7 shows a patterning of monodisperse microdroplets by the electrospray in microdripping mode. This technique allows an innovative approach for manufacturing energy, optical and electronic devices. A regime map is provided for identifying the limits to operate the EHD process under the microdripping mode to achieve uniform monodisperse microdroplets. An increase in nanoparticle concentration increases the liquid viscosity, which dampens the growth of perturbation and delays the jet breakup in the microdripping mode. However, viscosity does not affect the drop size in the dripping mode. For a given flow rate, the transition between ellipsoidal and conical meniscus regimes is found to occur at $Ca_e \approx 1.0$. The dripping mode occurs for $Ca_e < 1$ when the droplet size strongly depends on the electric capillary number ($r^* = -0.46Ca_e + 1$) compared

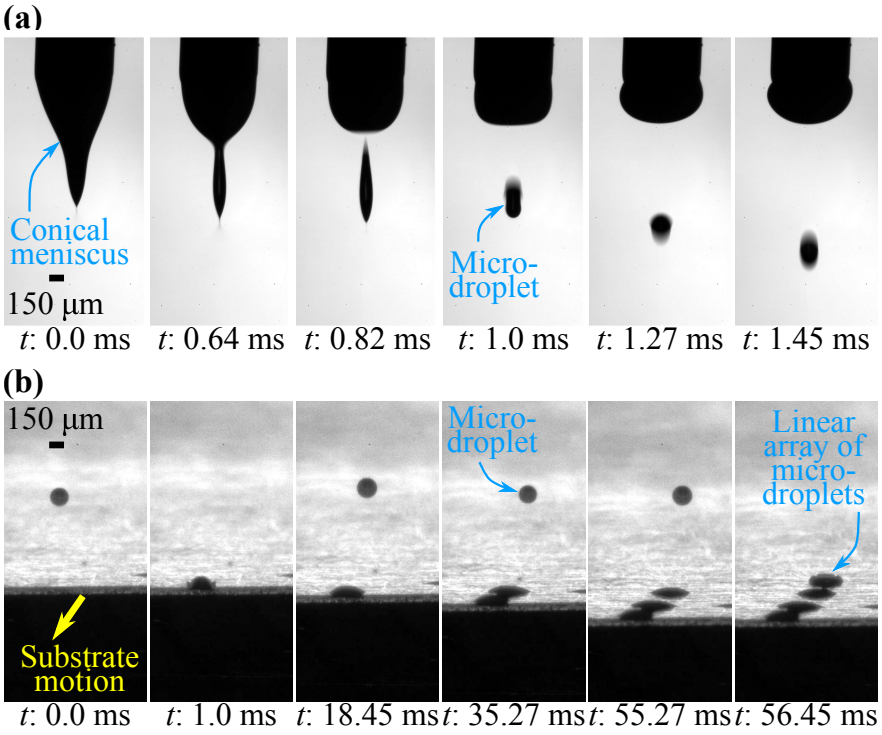

Figure 4.7: Patterning of monodisperse microdroplets of a suspension of Si 10 wt% in H_2O by the electrospray in microdripping mode. (a) Sequence of the detachment of a microdroplet from the electrified conical meniscus. (b) Patterning of a linear array of microdroplets on a moving substrate at a constant speed.

to the droplets of a nearly constant radius at $r^* = 0.1$ and $r^* = 0.07$ generated in microdripping and oscillating microdripping modes at a flow rate $Q = 1.67$ mm^3/s. Thus, the average droplet size can be determined using these results if the variables that define the electric capillary number and the radius of the droplet (r_0) in the absence of electric field are known. Electrical conductivity affects the transition between microdripping and oscillating microdripping modes. The onset of oscillating microdripping mode occurs first for suspensions with higher conductivity. Ejection of uniform microdroplets in the microdripping mode is observed in the range $2.0 \leq Ca_e \leq 2.5$ and the oscillating microdripping mode is reached at $Ca_e \geq 3.3$ for all the nanoparticle suspensions of this study.

4.3 Scaling laws for electrospray of semiconductor nanoparticle suspension in dripping and microdripping modes

In inkjet printing, the production of fine monodisperse droplets from a precursor suspension is of interest. These suspensions can have high viscosity and high density due to high particle concentration [114, 115]. Electrospray offers a viable method for the emission of small droplets from the detachment of liquid filaments deriving out of an elongated meniscus (Fig. 4.7a) caused by the action of an electric force; and patterning of the precursor suspension using the emitted droplets from the electrospray can be effected by moving the substrate at a constant speed (Fig. 4.7b). However, proportionality relations are needed, especially because they can be very useful to designers since

microdripping occurs in a very narrow range for a wide range of fluids with different physical properties.

In the previous section, several suspensions with varying properties were experimentally investigated to delineate the transition of the dripping, microdripping, and oscillating microdripping modes based only on the electric Capillary number (Ca_e). Only low viscosity and high electrical conductivity were studied, which allowed the estimation of the droplet diameter in terms of only Ca_e. For low Ca_e (lower voltage), the dripping mode was found to occur with linearly decreasing droplet diameter. Three key findings were made: 1) The dripping mode transitioned into microdripping mode in the range of $2.0 \leq Ca_e \leq 2.5$ after which the oscillating mode appeared. The microdripping regime is narrow but is essential for sintering nanoparticles on the substrate. 2) The microdripping mode provided the smallest and near-uniform droplet size (≈ 0.1 times the initial diameter) for all the suspensions; 3) The viscous effects, which are less important in the dripping mode, appeared to be important in the microdripping mode even for low viscous suspensions.

Since the microdripping mode is a stable method to generate uniform droplets carrying semiconductor particles for deposition on substrates, this section will focus on experiments and modeling of high viscosity suspensions having high electrical conductivity. Here, scaling laws that predict the droplet radius and frequency of droplet formation as a function of the electric capillary number, viscous capillary number and Bond number are presented.

4.3.1 Scaling analysis

Electrospray in the dripping mode has negligible inertial and viscous effects [128, 123], while in the microdripping mode the viscous effects affect the conical meniscus at the tip of the capillary tube from which the droplets are detached. Since both operation modes are inherently quasi-static for a constant flow rate, a steady state force balance is applied only at the onset of detachment to obtain a simple scaling law for the dripping and microdripping modes. The droplet grows up to the steady-state value and detaches from the nozzle, and this process repeats in a periodic manner to ensure the discharge of droplets at certain frequencies. The forces present on the droplet at the onset of detachment from the meniscus are: the hydrodynamic forces, i.e., viscous, and interfacial forces; the gravitational force and the electric force (Fig. 4.8a). The force balance is applied at the moment these forces are balanced and it is valid for either the ellipsoidal and conical meniscus, i.e., dripping and microdripping mode. However, different conditions must be applied for each mode, thus, yielding to different expressions that estimate the droplet radius as a function of nondimensional parameters for each regime.

The electric force on the droplet is estimated as, $F_{Electric} = S\varepsilon_0\varepsilon_r E^2/2$, where S, ε_0, ε_r, and E are the surface area of the droplet ($S = 4\pi r^2$), electric permittivity of vacuum, characteristic relative permittivity of each aqueous suspension, and the externally applied electric field [125]. The characteristic relative permittivity is defined as $\varepsilon_r = 1 + \sigma/(\varepsilon_0\omega)$ based on the Lorentz model for the interaction of electromagnetic waves in dielectric materials [125, 126], where σ and ω are the electrical conductivity of each aqueous suspension and characteristic frequency taken as c/L

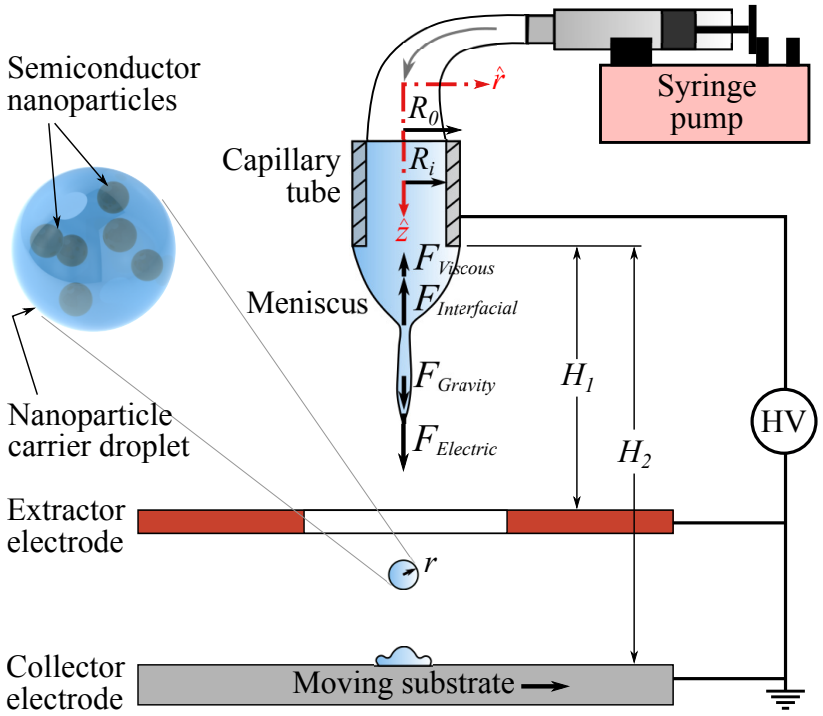

Figure 4.8: Schematic of the experimental setup. Fundamental force balance is applied at the onset of droplet detachment.

Semiconductor nanosuspension	$^{(c)}r_0$ (mm)	$^{(e)}r_0$ (mm)	u_c (m/s)	ε_r	Ca	Bo	Ca_e
Si, 2 wt% in H_2O	1.20	1.18	0.278	1.15	0.035	0.202	0 - 2.91
Si, 5 wt% in H_2O	1.21	1.19	0.278	1.21	0.031	0.204	0 - 2.90
Si, 10 wt% in H_2O	1.19	1.13	0.273	1.21	0.083	0.209	0 - 3.21
SiC, 2 wt% in H_2O	1.19	1.19	0.277	1.07	0.048	0.203	0 - 2.61
SiC, 5 wt% in H_2O	1.20	1.19	0.267	1.08	0.139	0.220	0 - 2.57
SiC, 10 wt% in H_2O	1.19	1.23	0.32	1.09	0.279	0.151	0 - 2.69
ZnO, 10 wt% in H_2O	1.25	1.29	0.292	1.17	0.041	0.190	0 - 3.08
ZnO, 30 wt% in H_2O	1.07	1.08	0.261	1.21	0.055	0.204	0 - 2.88
ZnO, 50 wt% in H_2O	1.05	1.07	0.232	1.27	0.405	0.254	0 - 2.92

Table 4.2: Relevant parameters of semiconductor nanosuspensions in DI water. $^{(c)}$Drop radius in the absence of electric field, calculated using Eq. (4.2). $^{(e)}$Drop radius in the absence of electric field from experiments.

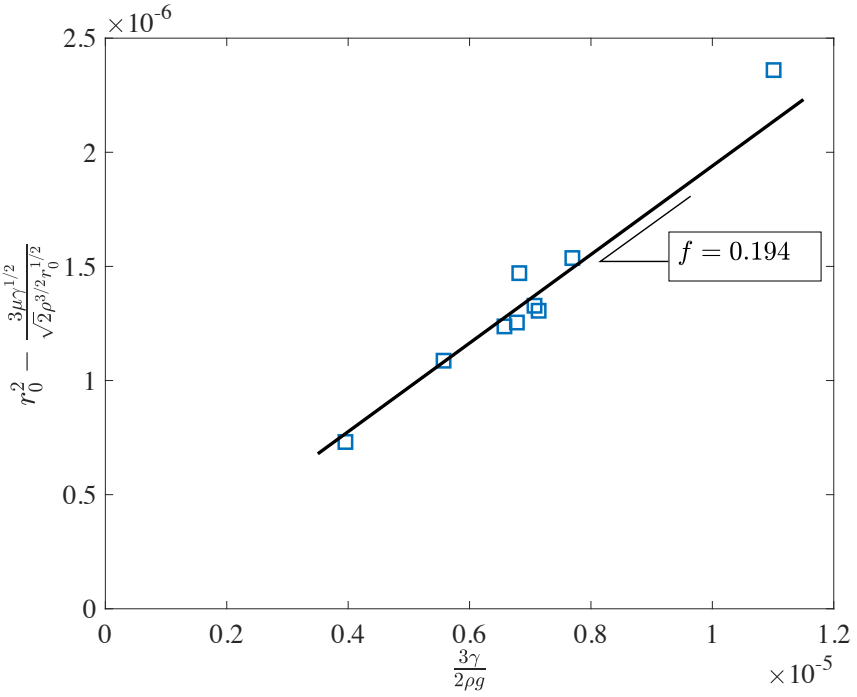

Figure 4.9: Experimental factor f from experimental data.

where c and L are the speed of light in the air and the distance from the center of the capillary tip and the inner edge of the extractor electrode. Here, r represents the average droplet radius based on the volume. The applied electric field is estimated as $E = E_1 + E_2$ by superposition of solutions for the three-electrode system of this study, where E_1 and E_2 are the electric fields between the capillary tube and 1) the extractor electrode and 2) the collector electrode. $E_1 = \sqrt{2}\phi/R_0 ln(4H_1/R_0)$ and $E_2 = \sqrt{2}\phi/R_0 ln(4H_2/R_0)$, where ϕ is the applied electric voltage [127]. The gravitational force is $F_{Gravity} = 4\pi r^3 \rho g/3$, where ρ and g are the fluid density and gravitational acceleration. The surface tension force restores the deformed droplet into a sphere after this moves away from the electrodes: $F_{Interfacial} = 2\pi w\gamma$, where $(2\pi w)$ and γ are the circumference of the meniscus in the neck area and the surface tension, and w can be taken as a function of r, i.e. $w = fr$, where f is a correction factor [123, 129]. The viscous force is the shearing force at the neck of the hanging liquid mass that depends on the liquid viscosity, μ, the rate of shear strain, and the surface area produced by the arc length of liquid neck $(2\pi r)$ and a characteristic viscous length, l. The shear rate $(\partial u/\partial y)$ is scaled as (u_c/l). Thus, the viscous shearing force is $F_{Viscous} = \mu u_c 2\pi r$. [130] u_c is estimated by considering an energy balance between the inertia and surface energy per unit area, which yields $u_c = \sqrt{2\gamma/r_0\rho}$, where r_0 is the radius of the largest droplet formed by gravity, surface tension and viscous forces just before detachment from the capillary tip in the absence of an electric field (i.e., $E = 0$). From Fig. 4.8a, $(F_{Electric} + F_{Gravity}) = (F_{Interfacial} + F_{Viscous})$ or $2\pi r^2 \varepsilon_0 \varepsilon_r E^2 + 4\pi r^3 \rho g/3 = 2\pi r f\gamma + 2\pi r\mu u_c$, from which

$$r = \frac{\sqrt{(\varepsilon_0 \varepsilon_r E^2)^2 + \frac{8}{3}\rho g(f\gamma + \mu u_c)} - \varepsilon_0 \varepsilon_r E^2}{\frac{4}{3}\rho g} \tag{4.1}$$

From Eq. (4.1), the radius r_0 is obtained as $r_0 = \sqrt{3(f\gamma + \mu u_c)/2\rho g}$. Using this expression of r_0 and noting that u_c depends on r_0, the following algebraic equation is obtained for determining r_0 in terms of the physical properties of the droplets.

$$r_0^{5/2} - \frac{3f\gamma}{2\rho g} r_0^{1/2} - \frac{3\mu\gamma^{1/2}}{\sqrt{2}\rho^{3/2}} = 0 \tag{4.2}$$

where, the correction factor was empirically found to be $f = 0.194$ (Fig. 4.9). The values of r_0 calculated using Eq. (4.2) and determined from experimental data are listed in Table 4.2.

Now the normalized drop size, ($r^* = r/r_0$) is obtained from Eq. (4.1) and it becomes,

$$r^* = \sqrt{1 + \frac{1}{4}\frac{(\varepsilon_0\varepsilon_r E^2)^2}{\frac{2}{3}\rho g(f\gamma + \mu u_c)}} - \frac{1}{2}\frac{\varepsilon_0\varepsilon_r E^2}{\sqrt{\frac{2}{3}\rho g(f\gamma + \mu u_c)}} \tag{4.3}$$

Rewriting Eq. (4.3) in terms of nondimensional parameters, electric capillary number (ratio of electric to surface tension force): $Ca_e = E^2\varepsilon_0\varepsilon_r R_0/\gamma$; Bond number (ratio of the gravity to surface tension force): $Bo = 2r_0^2\rho g/3\gamma$, and capillary number (ratio of viscous to surface tension force), $Ca = \mu u_c/f\gamma$,

$$r^* = \sqrt{1 + \frac{r_0^2}{4R_0^2}\frac{Ca_e^2}{Bo(1+Ca)}} - \frac{r_0}{2R_0}\frac{Ca_e}{\sqrt{Bo(1+Ca)}} \tag{4.4}$$

The electric force and the surface tension force are balanced when $Ca_e = 1$ and around this value, the transition between dripping and microdripping mode starts [38].

For the dripping mode, Eq. (4.4) can be rewritten as follows after binomial expansion when $r_0^2 Ca_e^2/4R_0^2 Bo(1+Ca) < 1$:

$$r^* = 1 - \frac{r_0}{2R_0}\left(1 - \frac{r_0}{4R_0}\frac{Ca_e}{\sqrt{Bo(1+Ca)}} + ..\right)\frac{Ca_e}{\sqrt{Bo(1+Ca)}} \tag{4.5}$$

For the microdripping mode, Eq. (4.4) is written as

$$r^* = \frac{r_0}{2R_0}\frac{Ca_e}{\sqrt{Bo(1+Ca)}}\sqrt{1+\frac{4R_0^2}{r_0^2}\frac{Bo(1+Ca)}{Ca_e^2}} - \frac{r_0}{2R_0}\frac{Ca_e}{\sqrt{Bo(1+Ca)}} \tag{4.6}$$

which can be simplified as follows by binomial expansion when $4R_0^2Bo(1+Ca)/r_0^2Ca_e^2 < 1$:

$$r^* = \frac{R_0}{r_0}\left(1-\frac{R_0^2}{r_0^2}\frac{Bo(1+Ca)}{Ca_e^2}+..\right)\frac{\sqrt{Bo(1+Ca)}}{Ca_e} \tag{4.7}$$

Thus, defining the coefficients δ_1 and δ_2 as $(r_0/2R_0)(1-r_0Ca_e/4R_0\sqrt{Bo(1+Ca)}+...)$ and $(R_0/r_0)(1-R_0^2Bo(1+Ca)/4r_0^2Ca_e^2+...)$ respectively, the normalized drop size can be predicted as shown in Eq. (4.8) and (4.9), where these coefficients are to be determined empirically.

$$r^* = 1-\delta_1\frac{Ca_e}{\sqrt{Bo(1+Ca)}} \quad ; \text{Dripping} \tag{4.8}$$

$$r^* = \quad \delta_2\left(\frac{Ca_e}{\sqrt{Bo(1+Ca)}}\right)^{-1} \; ; \text{Microdripping} \tag{4.9}$$

Next, the number of emitted droplets from the meniscus is estimated to be $N_d = 3Q/4\pi r^3$ and is normalized as $N_d^* = (N_d r_0^3/Q)^{1/3}$. Thus, N_d^* for dripping and microdripping mode is determined as Eq. (4.10) and (4.11) respectively.

$$N_d^* = \quad \left(\frac{3}{4\pi}\right)^{1/3}\left(1-\frac{\delta_1\, Ca_e}{\sqrt{Bo(1+Ca)}}\right)^{-1} \tag{4.10}$$

$$N_d^* = \left(\frac{3}{4\pi}\right)^{1/3}\frac{Ca_e}{\delta_2\,\sqrt{Bo(1+Ca)}} \tag{4.11}$$

It should be noted that the force balance contains four different forces where the gravity force is given as an exact term, and a correction factor f is introduced for the interfacial force. This factor is found from the experimental data as shown in Fig. 4.9. However, the other two forces,

i.e., electric and viscous, represent estimated expressions. To account for these two approximations and the higher order terms neglected in the binomial expansions (Eq. (4.5) and (4.7)), δ_1 and δ_2 are introduced as correction factors in Eq. (4.8) and (4.9). In order to test the applicability of the group in Eq. (4.8)-(4.11), nine suspensions of varying viscosities and electrical conductivities over a wider range are tested by increasing the voltage.

4.3.2 Experimental results

It should be noted that all suspensions were made by dispersing the semiconductor nanoparticles [silicon (Si), silicon carbide (SiC), and zinc oxide (ZnO)] in de-ionized (DI) water with a surfactant [sodium dodecyl sulfate (SDS)] and dispersant (sodium salt of poly-naphthalene sulfonic acid) and sonicating the resulting mixture for 1 hr at an ultrasonic frequency of 20 kHz. The physical properties and relevant parameters of these suspensions are listed in Table 3.1 and 4.2. All samples, especially those suspensions with high nanoparticle concentration (e.g., ZnO, 50 wt% in DI water), display shear thinning yield stress behavior at low shear rates. However, at relatively high shear rates, the hydrodynamic interactions between the dispersed particles and medium are predominant, leading to Newtonian behavior. The values of the shear rate for the occurrence of Newtonian flow was determined from experimental data on the relative viscosity vs. shear rate. The value at which the suspensions start to display Newtonian behavior was found to vary from 50 s^{-1} to 60 s^{-1}. Using the Hagen-Poiseuille flow model within the capillary tube, $\dot{\gamma} = 2Q/\pi R_i^3$, where $\dot{\gamma}$ and Q are the average shear rate and the volumetric flow rate. The volumetric flow rate of 1.67 mm^3/s was

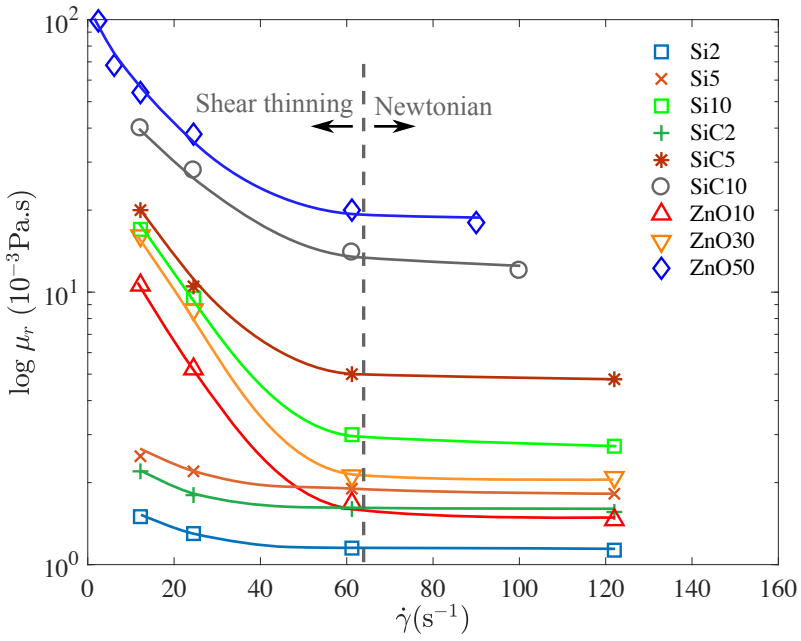

Figure 4.10: Relative viscosity of semiconductor nanosuspensions versus shear rate. The numeral suffixes denote wt% of the semiconductor materials.

found to yield an average shear rate of 64 s^{-1}, beyond which the fluid is Newtonian as seen from the experiments in Fig. 4.10. This agrees with experimental observations in the microdripping mode, where lower volumetric flow rates than 1.67 mm^3/s cause the tip of the capillary tube to clog gradually until the fluid is completely stopped since the suspensions exhibit a pseudoplastic behavior manifesting their higher viscosity. Only with higher flow rates, i.e., higher shear rates, all nanoparticle suspensions surpass the shear-thinning region to behave as a Newtonian fluid as it can be seen in Fig. 4.10.

The droplet radius observed in this study is between $1.3 - 0.65$ mm and $74 - 150\mu$m with formation rates between 0.2 - 1.5 and 100 - 650 droplets per second for the flow rate 1.67 mm^3/s in the dripping and microdripping mode, respectively.

In the dripping mode, the droplets are formed from a hemispherical or ellipsoidal meniscus, while the electric field-induced stretching of the fluid develops a conical meniscus called the Taylor cone. A neck develops between the meniscus and a pendant liquid filament at the end, which becomes thinner with time and eventually collapses releasing a droplet. This droplet ejection process is periodic and monodisperse. In the microdripping mode (Fig. 4.11), the conical meniscus and hence the ejected droplet are relatively small, as are the gravity force and Bond number. For the high viscosity fluid, the electric force stretches the liquid to form the meniscus and the liquid filament, while the viscous friction prevents the elongation of the liquid filament, and the surface tension force first resists the formation of this pendant filament, but once the droplet is detached, the restoring force of the capillary effects turns the spindle-shape liquid filament into a spherical droplet. The relative influence between the viscous and interfacial force is quantified by *Ca*, i.e., the strength of the viscous force becomes more evident for suspensions with higher *Ca*. Higher characteristic velocity leads to higher *Ca*, resulting in a conical meniscus rather than a hemispherical one. In contrast, the velocity is lower in the dripping mode and the evolution of the ellipsoidal meniscus is weakly influenced by the *Ca*. Thus, the effect of viscosity is minimal in the dripping mode, however, in the microdripping mode, the droplet size increases slightly with increasing viscosity and the apex of the meniscus stretches more in highly viscous suspensions (Fig. 4.11).

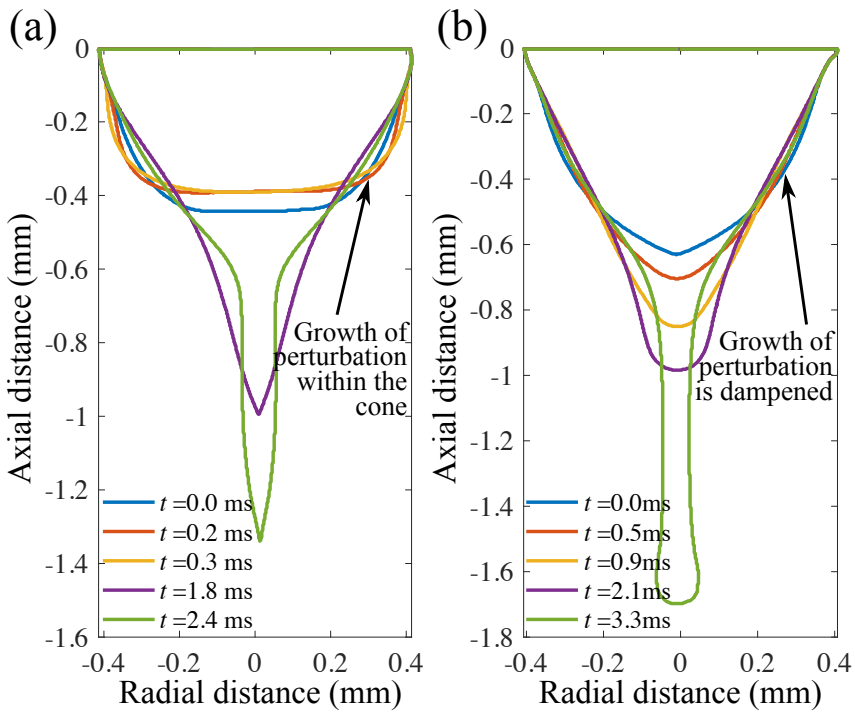

Figure 4.11: Comparison of the sequence of growth of the image-processed conical meniscus due to the action of an electric force. (a) Microdripping of low viscosity suspension (Si 10 wt% in H_2O, $Ca = 0.083$, $\phi = 4$ kV). (b) Microdripping of high viscosity suspension (SiC 10 wt% in H_2O, $Ca = 0.279$ $\phi = 5$ kV).

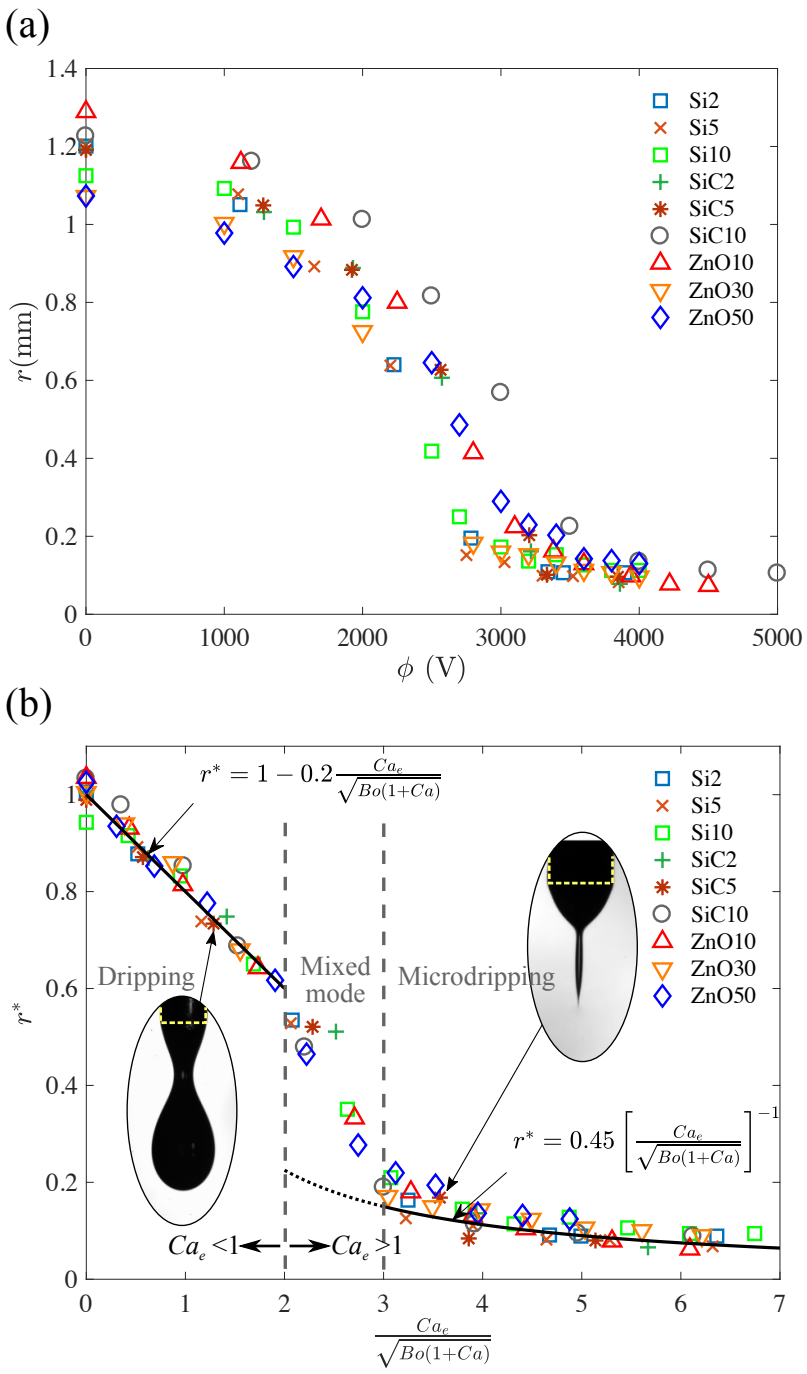

Figure 4.12: Size of emitted droplets. (a) Drop size vs applied electric voltage. (b) Normalized drop size vs the ratio $Ca_e/\sqrt{Bo(1+Ca)}$. Markers represent the experimental data, while the solid lines are the theoretical prediction of Eq. (4.8) and (4.9) for dripping and microdripping mode, respectively. $\delta_1 = 0.2$ (Eq. (4.8)) and $\delta_2 = 0.45$ (Eq. (4.9)) for $Q = 1.67$ mm^3/s.

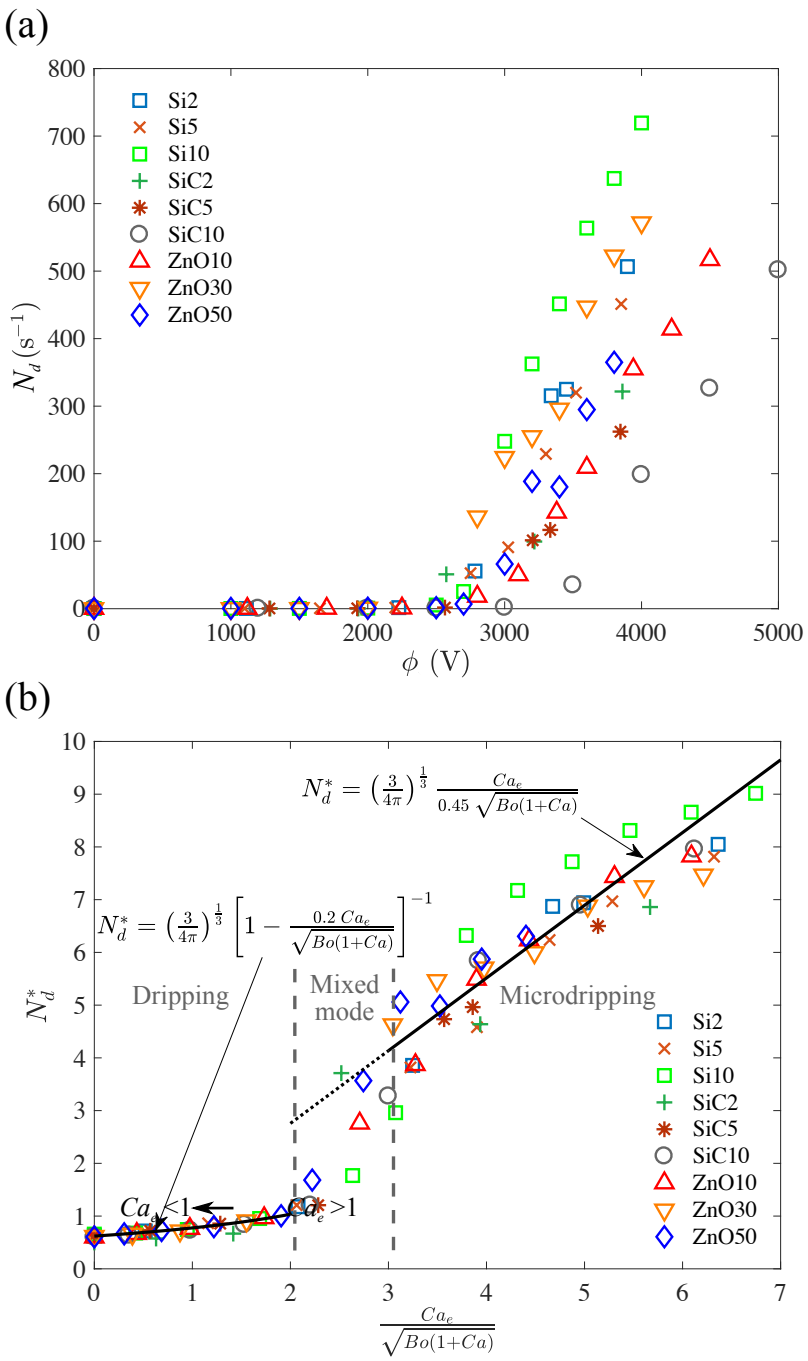

Figure 4.13: Number of emitted droplets. (a) Frequency of droplet formation vs applied electric voltage. (b) Nondimensional frequency of droplet formation vs the ratio $Ca_e/\sqrt{Bo(1+Ca)}$. Markers represent the experimental data, while the solid line is the theoretical prediction of Eq. (4.10) and (4.11).

Viscosity affects the shape of the cone by resisting its deformation and thus promotes a stable microdripping mode.

In general, the capillary forces increase the neck radius to minimize the curvature of the liquid-air interface, while the gravity and electric force stretch the interface until they balance the viscous friction and capillary force. The scaling considerations provided in Eq. (4.8) and (4.9) fit the data well (Fig. 4.12) showing that r^* is a linearly decreasing function of $Ca_e/\sqrt{Bo(1+Ca)}$ in the dripping mode in the range $Ca_e/\sqrt{Bo(1+Ca)} < 2$, and a hyperbolic function for $3 < Ca_e/\sqrt{Bo(1+Ca)} < 7$. This suggests that this group of parameters arising from physical considerations based on force balance is the appropriate parameter for this problem for a wide range of viscosity and electrical conductivity. The regime between the dripping and microdripping modes is characterized as mixed mode because here the suspensions can be in either mode. Otherwise, for a given suspension and a set of physical properties, dripping mode smoothly transitions into microdripping mode where $r^* \approx 0.1$ is measured.

The frequency of droplet formation increases with higher electric voltages (Fig. 4.13a). This frequency is influenced by the formation of the conical meniscus, which occurs at different voltages for different suspensions, i.e., at 2500 V for Si, 10 wt% in DI water and 3500 V for SiC, 10 wt% in DI water. This is also the reason for different frequencies of droplet formation at a given electric voltage for different suspensions. For example, for the above two suspensions, 200 and 650 droplets per second are ejected from the capillary tube respectively at 4000 V. The nondimensional frequency of droplet formation, N_d^*, correlates well as a function of the ratio between the electric capillary number and the Bond and capillary number. The nondimensional meniscus frequency or

frequency of droplet formation has a gradual slope for $Ca_e/\sqrt{Bo(1+Ca)} < 2$, while it behaves linearly when the electric force is dominant over the other forces, i.e. when $Ca_e/\sqrt{Bo(1+Ca)} > 3$ as shown in Eq. (4.11). This change in slopes occurs due to the formation of the conical meniscus, i.e. beyond $Ca_e/\sqrt{Bo(1+Ca)} = 2$. N_d^* is almost linear (Fig. 4.13b) and compares well with the theoretically obtained expressions in Eq. (4.10) and (4.11).

In summary, experiments were performed for a wide range of the relevant parameters such as Bo, Ca, and Ca_e as listed in Table 4.2. This was done for a number of suspensions with a wide range of physical properties, voltages from 0 to 5000 V and for a constant flow rate. The droplet size and frequency of droplet formation for different suspensions obtained from experiments spread over a wide band as a function of voltage (Figs. 4.12a and 4.13a). The spread in the data can be collapsed into single curves by employing convenient nondimensional parameters (Figs. 4.12b and 4.13b) as it has been also achieved for analogous problems [131]. The model also shows that the radius is linearly decreasing with respect to this parameter in the dripping mode (Eq. (4.8)) and has an inverse relationship in the microdripping mode (Eq. (4.9)). Based on the nondimensional plots of the experimental results in Fig. 4.12b, we are able to determine the correction factors δ_1 and δ_2 for the dripping and microdripping modes respectively. The nondimensional frequency of droplet formation also predicts the experimental results well as shown in Fig. 4.13b for the same values of δ_1 and δ_2.

Furthermore, electrohydrodynamic inkjet printing of semiconductor nanoparticle suspensions can be accomplished by the operation of an electrospray in microdripping mode and is more efficient than conventional inkjet printing. The effect of the physical properties on the droplet size

and frequency of droplet formation is more precisely described by the relative influence of all the acting forces. A theoretical model has yielded a parameter, $Ca_e/\sqrt{Bo(1+Ca)}$ which accounts for all the acting forces. Results for all suspensions with a wide range of viscosity show that r^* can be correlated using this parameter in both dripping and microdripping modes. The same parameter also correlates the normalized frequency of droplet formation as an increasing function in the microdripping mode. Viscosity affects the shape of the cone by resisting its deformation and thus promoting a stable microdripping mode. Reduction in surface tension decreases the drop size in dripping and microdripping modes. However, the capillary size and electrical conductivity have minimal effect on the size of the ejected droplets. Based on the analysis, it is possible to design the electrospray to produce uniform monodisperse droplets by manipulating the voltage at the electrode, for any desired nanoparticle concentration of a suspension to be sintered on a substrate.

CHAPTER 5
SUBWAVELENGTH FOCUSING BY MICRODROPLETS FOR LASER-ASSISTED ADDITIVE MANUFACTURING

5.1 Introduction

Two technological breakthroughs of the last decade have been subwavelength focusing of a laser beam using a superlens based on metamaterials, and patterning of semiconductor materials to produce flexible electronics. A novel interdisciplinary mechanism of interaction between lasers and microdroplets is discussed in this Chapter to achieve subwavelength focusing and deposit nanoparticles on a silicon wafer and flexible substrates such as plastics and papers. This technology can potentially be implemented for roll-to-roll manufacturing of optoelectronic components such as light-emitting diodes [91] and solar cells [2], sensors, actuators, and ultra-flexible electrodes for neuro-stimulators and prosthetics [92]. Semiconductor materials have been patterned on flexible substrates by conventional inkjet printing to promote nanoelectronics technology [3, 4], but the inkjet-printed films require substantial annealing to improve their electrical conductivity by evaporating the organic ink material. Since the deposition process discussed in this dissertation utilizes aqueous suspension of nanoparticles, i.e., aqueous ink, and a laser beam, the nanoparticles are sintered and simultaneously annealed by the beam as the deposition occurs.

Subwavelength focusing of the laser beam is necessary to print nanodots smaller than the laser wavelength, or subwavelength features such as a nanohole in a substrate. The ability to achieve subwavelength focusing is limited by the diffraction effect of light, as it was described in Chapter 2 (Eq. (2.13)). A slab of negative refractive index metamaterial, which is an unconventional alternative to a lens, has the power to focus and achieve smaller focal spot diameters [12, 13, 15]. The objective of those studies has been to overcome the diffraction limit for imaging objects in the nanometer scale, demonstrating very high resolutions of $\lambda/6$ [13, 14] and $\lambda/20$ [15]. However, passive negatively refracting materials have the disadvantage of being inherently dissipative. With positive refraction, the ability to achieve subwavelength focusing has been analyzed for the perfect lens effect of Maxwell's fish eye in both two-dimensional [16] and three-dimensional [17] media.

Photonic nanostructures [69, 70], random nanoparticles [18, 71], solid microspheres [19, 20], and liquid droplets [21, 22] have been utilized to resolve subwavelength features. A droplet placed on a substrate provides the lensing effect due to the curvature and refractive index of the liquid, overcoming the diffraction limit and writing patterns that have sizes one-fourth of the laser wavelength [22]. The subwavelength focusing by their method [22] is not readily amenable to implementation in practice to produce thin films or nanodot arrays using nanoparticles since their method requires close proximity between the objective of the microscope and the object, and does not provide a convenient means of replacing the liquid droplet lens to supply fresh nanoparticles to the focused laser beam.

It has already been discussed in Chapter 4 that the electrohydrodynamics of microdroplets generate electrosprays in several modes depending on the feed rate of microfluidic nanoparticle sus-

pensions and the externally applied electric field. This Chapter will discuss a method that utilizes these electrosprayed microdroplets for subwavelength focusing of laser beams in a manufacturing technique as illustrated in Fig. 5.1.

5.2 Subwavelength focusing by microdroplet superlens

In this study, a new microdripping mode was used [38], in which the interaction between the microdroplets and laser beam was stable. Microdroplets of nanoparticle suspension enable depositing germanium (Ge) and silicon (Si) nanodots on a silicon substrate, and microdroplets of water produce tiny holes of remarkably small diameter $\lambda/10$. Each microdroplet serves the dual role as a nanoparticle carrier to the substrate and as a superlens that focuses the laser beam to a subwavelength diameter. An axicon lens and a biconvex lens are used to shape a Nd:YAG Gaussian laser of wavelength 1064 nm into an annular beam of nearly uniform radial irradiance distribution. A special hollow parabolic mirror is used to focus the annular laser beam while microdroplets are injected into the hollow beam through the hole in the mirror. The laser beam is focused by the mirror to form a hollow laser cone and refocused by the microdroplet superlens during the laser-droplet interactions in the vicinity of the apex of the cone near the substrate surface. Laser heating of the droplets evaporates the water and sinters the nanoparticles to form microlayers on the substrate. The laser-droplet interactions can be implemented for depositing thin films, lines and regular arrays of microdots as well as nanodots. This process is shown in Fig. 5.1(a-c).

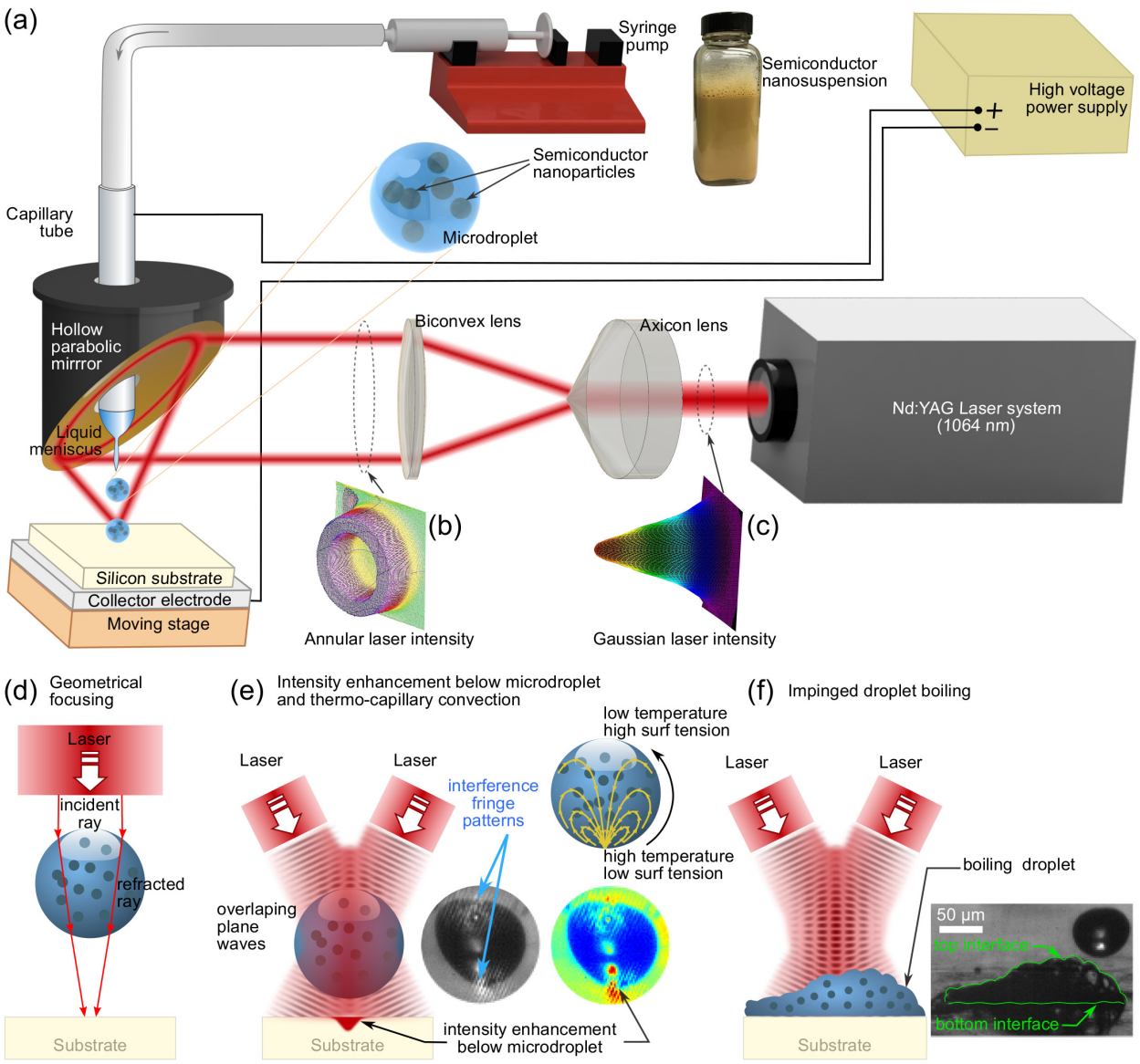

Figure 5.1: Concept of microdroplet superlens of dual role carrying nanoparticles and subwavelength focusing. (a) Schematic representation of setup used to achieve subwavelength focusing of the laser beam using microdroplet superlens. (b) Measured intensity profile of the annular laser beam. (c) Gaussian laser intensity from the Nd:YAG laser. (d) Geometrical focusing of the beam when the microdroplet acts as an optical lens. (e) Incident laser at the top of the microdroplet and intensity enhancement below the same microdroplet. (f) Incident laser at the interface of the boiling droplet after its impingement on the substrate.

Figure 5.1 illustrates the concept of a microdroplet superlens of dual role carrying nanoparticles for subwavelength focusing. Fig. 5.1a shows a schematic representation of the experimental setup (shown in Fig. 3.4) used to achieve subwavelength focusing of laser beam using microdroplet superlens. A Nd:YAG laser system produces a laser beam ($\lambda = 1064$ nm). An electrospray is operated in microdripping mode to generate uniform monodisperse microdroplets. An axicon lens and a biconvex lens are used to shape a Gaussian to an annular beam. A hollow parabolic mirror focuses the annular beam at the microdroplet impingement spot. An X-Y motorized stage is used to move a silicon substrate continuously and a micrometer vertical translation stage is used to move the substrate in the Z-direction, so that the laser spot size can be varied depending on the kind of substrate used. Figs. 5.1b and 5.1c show the measured intensity profile of the annular laser beam and the Gaussian laser intensity from the Nd:YAG laser. Fig. 5.1d describes the geometrical focusing of the beam when the microdroplet acts as an optical lens. Fig. 5.1e shows the incident laser at the top of the microdroplet and the intensity enhancement below the same microdroplet. A photograph displays the fringe patterns caused by the interference of the focused annular laser. The intensity enhancement at the bottom of microdroplet is shown by image processing of the droplet photograph. The temperature at the bottom of microdroplet is increased and this promotes thermo-capillary convection within the droplet. Finally, Fig. 5.1f displays the incident laser at the interface of the spreading droplet after its impingement on the substrate. A top and bottom interfaces are formed with radii much smaller than the radius of the microdroplet.

In this process, the diffraction limit is overcome by the near-field optics effect [66] involving the laser-microdroplet interactions. The radii of the microdroplets vary from 10 to 70μm with

the average radius of 35 to 40μm depending on the nanosuspensions tested (see Table 5.1). The interference due to superposition at the apex of the conical hollow laser beam produces an irradiance distribution which is proportional to $J_0^2(k\dot{r})$ similar to a Bessel beam, where, k, $\dot{r}$, and J_0 are the spatial angular frequency or wavenumber, radial coordinate, and first kind Bessel function of order zero, respectively. In addition, the curvature of the microdroplet surface concentrates the electromagnetic field like a lens [75, 73] and, therefore, enhances the laser irradiance (Fig. 5.1d). Consequently, the laser irradiance varies inside the droplets in both transverse and longitudinal directions due to the interference and focusing effects respectively, resulting in nonuniform heating with significant temperature variation in the droplets. This heating mechanism promotes Marangoni convection [132], inducing nanoparticle advection as shown in Fig. 5.1e. Also, the refractive index varies spatially due to nonuniform temperature distribution, affecting the focusing capability of the droplets. The nonuniform heating of the droplet leads to nonuniform surface evaporation, deforming the original smooth surface into multiple curved surfaces of small radii of curvature (Fig. 5.1f).

Figure 5.2 shows: (a) the stretching of the electrified meniscus and formation of monodisperse microdroplet. The interaction between the hydrodynamic forces, i.e., inertial, viscous, and interfacial forces; and the electric force detaches a small volume of liquid drop compared to the size of the capillary tube [38]. (b) histogram of the radius of ejected microdroplets for surfactant solution containing no nanoparticles. The size of these droplets ranges from 10 μm to 70 μm with an average size and standard deviation of 36.3 μm and 9.3 μm respectively. (c) temporal view of the laser-droplet interaction as the droplet travels toward a silicon substrate for a laser beam of

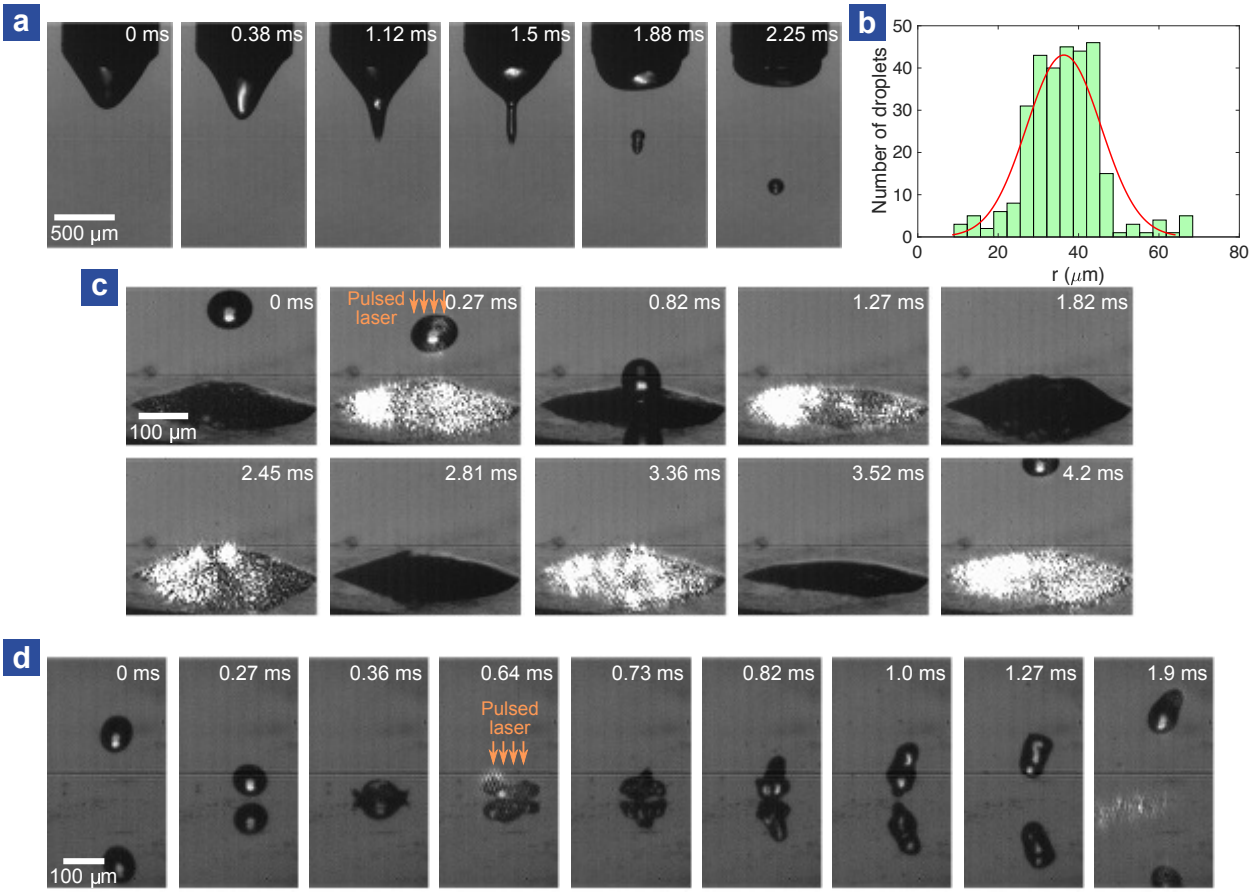

Figure 5.2: High speed imaging of microdroplet-laser interaction. (a) Droplet formation from the capillary tube under the action of an electric field (3300 V). Electrospray operated in microdripping mode. (b) Histogram of radius of droplets generated in microdripping mode for DI water with surfactant concentration of 8mM (Ge0) at a flow rate of 10 μl/min. Average droplet radius, 36.3 μm (mean value) and standard deviation of 9.3 μm. (c) Sequence of droplet impingement and laser interaction on silicon substrate at laser power of 17 W. The spreading droplet boils due to laser heating. (d) Rebound of droplet on the same substrate when the laser power is increased at 22 W.

Semiconductor nanosuspension	ρ (g/ml)	μ (10^{-3} Pa.s)	σ (10^{-6} S/cm)	γ (10^{-3} N/m)	r (μm)
Ge, 0 wt% in H_2O	1.0	1.10	595.0	49.8	36.3
Ge, 2 wt% in H_2O	1.023	1.36	718.2	47.2	38.1
Ge, 5 wt% in H_2O	1.064	1.56	797.8	47.5	37.9
Ge, 10 wt% in H_2O	1.130	1.95	898.4	47.6	37.7
Ge, 20 wt% in H_2O	1.263	2.77	938.0	48.0	37.5
Si, 5 wt% in H_2O	1.033	1.82	1391.6	48.2	39.8
Si, 20 wt% in H_2O	1.123	4.72	1512.4	50.1	40.3

Table 5.1: Physical properties and relevant parameters of semiconductor nanosuspensions used for the study of microdroplet superlens.

power 17 W and diameter 285 μm on the substrate surface. The interference fringes caused by the overlapped electromagnetic waves of the conical laser beam can be seen as bright spots in some of the photographs captured with a high speed camera operating at the spectral range 350 - 950 nm. The fringes were visible only during the time the pulsed laser was on. The bright spot inside the droplet suggests that the laser cone was refocused by the droplet acting as Maxwell's fish eye lens.

Subwavelength features are not produced at very low laser powers due to insufficient energy to create holes or deposit nanodots. Above the threshold laser power, the droplets begin to boil

and the subwavelength holes and nanodots are perceptible under a microscope. More rapid boiling occurs at moderate laser powers and secondary droplets begin to emerge from the boiling droplet as the laser power is increased further. The secondary droplets are caused by the blowout of vapor bubbles into the ambient. These vapor bubbles are formed during the boiling process due to heterogeneous nucleation at the surface of the suspended nanoparticles or the solid substrate. Therefore, the deformation of the top and bottom surfaces (Fig. 5.1f) of the impinged droplets are significantly influenced by the boiling rate of the liquid.

Above the critical laser power, the substrate surface is excessively heated by the laser and the interfacial tension at the substrate-droplet interface changes significantly, resulting in a restricted spreading of the droplets on the substrate surface. The incident droplet loses its kinetic energy by viscous dissipation and friction with the substrate as it spreads upon impact on the substrate. However, due to changes in the surface tension at high substrate temperatures, the droplet spreads partially with a minimal deformation of the original spherical shape of the incident droplet and subsequently retracts back to its original shape and bounces in the upward direction [133, 134, 135]. This rebound of the droplets may be due to localized rapid vaporization of the liquid at the point of contact between the droplet and substrate, resulting in the Leidenfrost effect [136, 137].

Due to insufficient energy at low laser powers and non-sticking capability of droplets at high laser powers, subwavelength focusing needs to be accomplished in a narrow range of the laser power for creating nanostructures as illustrated in Fig. 5.3. Fig. 5.3a shows scanning electron microscopic (SEM) images of the manifold of subwavelength holes within a larger crater on a Si substrate. These features were obtained using microdroplets of a surfactant solution containing

no semiconductor nanoparticles. The subwavelength holes of diameters varying from 100 nm to 200 nm inside the crater indicate the superlens effect of the droplets. The diameter of the crater, which is approximately 5 μm, suggests that the original laser cone has been refocused by the microdroplets to a very small diameter. The effect of microdroplets containing semiconductor nanoparticles is presented in Fig. 5.3b, showing the SEM images of a linear array of Ge nanodots on a Si substrate for a suspension of 5 wt% Ge in DI water. Similarly, Fig 5.3c shows the SEM images of Si nanodots deposited on a Si substrate for a suspension of 5 wt% Si in DI water. The diameter of the nanodots varies from 100 nm to 500 nm. The results in Figs. 5.3a, 5.3b, and 5.3c were obtained with an input laser power of 17W.

The depth of the subwavelength holes is limited to small depths of nanometer scales because the irradiance of the evanescent waves decreases exponentially and becomes negligible within approximately half of a wavelength away from the bottom surface of the boiling droplet. For instance, the depth of the subwavelength holes in Fig. 5.3a is found to be approximately 120 nm. Also, a rim is formed by the resolidification of the Si melt around the entrance of the hole and this rim protrudes approximately 30 nm above the original substrate surface. These results, which were obtained using the optical profiling feature of a laser interferometer, are shown in Fig. 5.4. Finally, a process chart, showing the range of laser power for producing subwavelength features is presented in Fig. 5.5 for microdroplets containing Ge of 0 wt% (i.e. surfactant solution only), 2 wt%, 5 wt%, and 10 wt% in DI water.

In the case of microdroplets containing no nanoparticles, the occurrence of subwavelength focusing may be due to a particular variation of the refractive index inside the droplet so that the

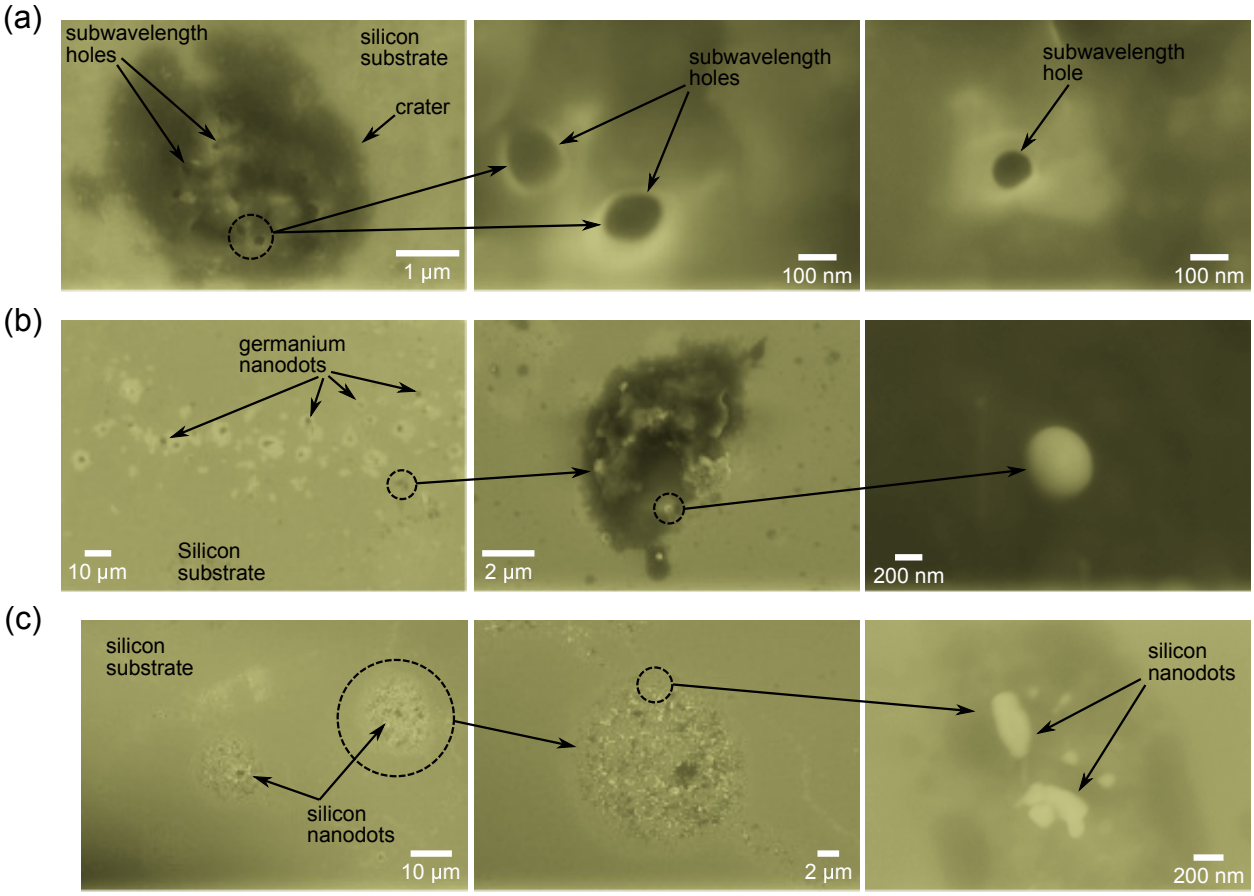

Figure 5.3: Subwavelength holes and nanodots on a silicon substrate. (a) SEM images of the subwavelength holes on Si substrate. Features were realized by superlens microdroplet of a surfactant solution without the presence of any semiconductor nanoparticles and an input laser power of 17 W. Existence of a manifold of subwavelength holes ranging between 100 nm to 200 nm contained inside a crater. (b) SEM images of a linear array of Ge nanodots. Features were produced by microdroplets of suspension of Ge, 5 wt% in DI water and input laser power of 17 W. (c) SEM images of deposition of Si nanodots (cluster of nanoparticles). Features range from 100 nm to 500 nm and were produced by microdroplets of suspension of Si, 5 wt% in DI water and an input laser power of 17W.

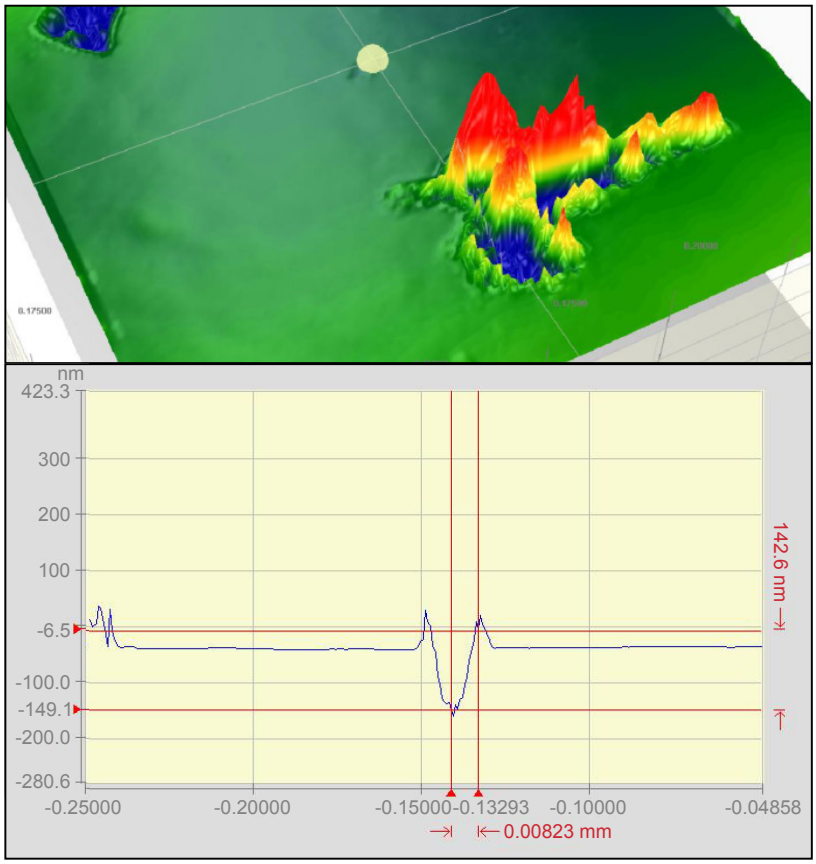

Figure 5.4: Optical profiling of feature shown in Fig. 5.3a with a laser interferometer. Three-dimensional surface measurement shows the presence of tiny indentation. The depth of the crater is approximately 120 nm and a rim formed from recast silicon protrudes approximately 30 nm above the original substrate surface.

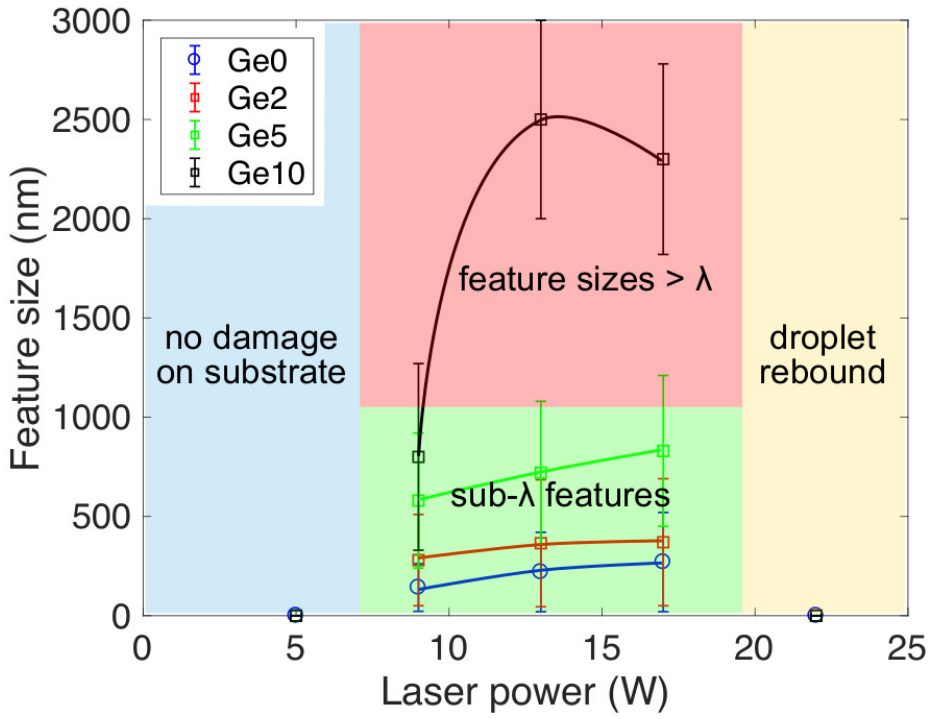

Figure 5.5: Feature sizes as a function of the input laser power for microdroplets containing a concentration of Ge of 0 wt% (surfactant concentration of 8mM), 2 wt%, 5 wt%, and 10 wt% in DI water. The numeral suffixes denote wt% of Ge.

droplet acts as Maxwell's fish eye lens [138] for a particular profile of the refractive index or a Lüneberg lens [139] for another form of the index profile (Fig. 5.6a). These lenses are known to enable perfect focusing with unlimited resolution within the approximation of geometrical optics to produce focal spot diameter not limited by the optical wavelength. The resolution of these lenses is free of known Abbe's limitation. Also, an infinite number of the refractive index profiles has been identified [139] to produce this type of perfect lens effect. Perfect focusing with positive refractive index materials has been analyzed for light rays since 1854 [138], but only recently the wave description of light has been shown to validate the perfect lens effect of Maxwell's fish eye in both two-dimensional [16] and three-dimensional [17] media.

In the case of microdroplets containing nanoparticles, the scattering of light by the nanoparticles can produce evanescent waves that converge to a point to induce subwavelength focusing [18]. A single nanoparticle scatters the electromagnetic wave of the incident laser beam into multiple waves of different wave vectors. These waves, in turn, are scattered multiple times by the surrounding nanoparticles, resulting in a manifold of various wave vectors consisting of both propagating and evanescent waves of different phases for each wave vector (Fig. 5.6b). The propagating waves are generated when the surfaces of constant amplitude and constant phase coincide. If this condition is not satisfied, evanescent waves are produced and their amplitudes decrease exponentially so that the amplitude becomes negligible within a distance of approximately twice the wavelength of each wave. These waves interfere on the substrate surface in the near field and produce subwavelength spatial modes, resulting in a speckle interference pattern of nonuniform irradiance distribution that generates the observed subwavelength features in this study. The subwavelength

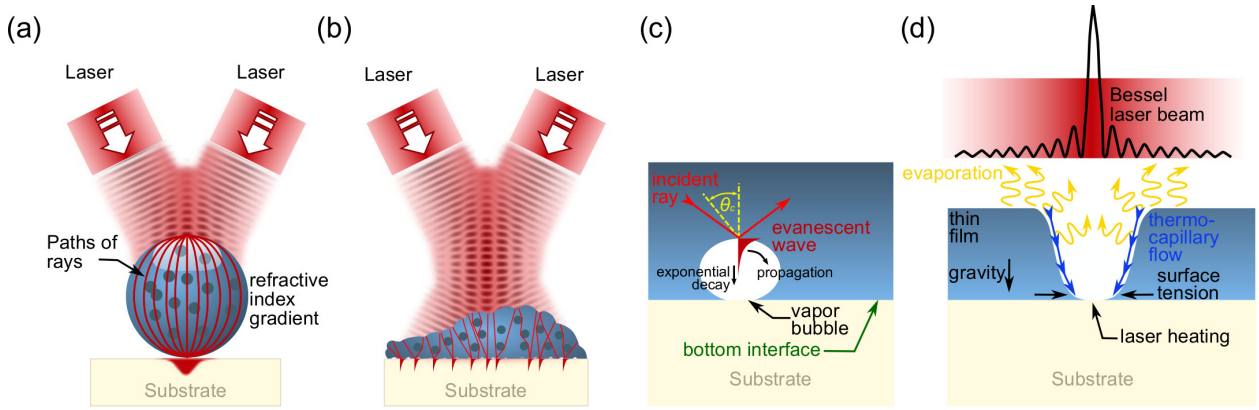

Figure 5.6: Schematic representation of possible mechanisms yielding to subwavelength focusing of the incoming laser beam. (a) Subwavelength focusing due to a particular variation of the refractive index inside the droplet. The droplet acts as a Maxwell's fish eye lens. (b) Subwavelength focusing when the plane wave is scattered by the nanoparticles. A manifold of different wavevectors is generated containing propagating and evanescent waves. (c) Subwavelength focusing caused by the evanescent waves originated due to total internal reflection when the angle of incidence of the ray is greater than the critical angle. Vapor bubbles are generated due to heterogeneous nucleation at the substrate during the droplet boiling process. The evanescent waves propagate along the interface and decay exponentially in the normal. (d) Microfluidic cooling mechanism.

focusing, however, may also be due to Maxwell's fish eye lens. Such a lens can be formed by the nanoparticles lying as a layer on the substrate surface and the liquid occupying the interstitial spaces between the particles as the microdroplet is being evaporated by the laser beam. This heterogeneous structure may give rise to an appropriate refractive index distribution to act as a two-dimensional perfect lens since planar heterostructures such as air holes in silicon [140] and silicon pillars on silica [141] have been shown to modify the index profile.

Another optical effect for the observed subwavelength nanostructures may be the total internal reflection at the interface between a vapor bubble and the surrounding liquid with the vapor bubble having lower refraction index than that of the liquid. The vapor bubbles are formed due to laser heating and heterogeneous nucleation at the substrate surface. The curved liquid surface (Fig. 5.6b) can bend various rays of the laser beam into different angles so that certain bundle of rays may incident on some of the bubbles at a supercritical angle which is larger than the critical angle (θ_c) for total internal reflection (Fig. 5.6c). Under this condition, evanescent waves are generated and these waves decay exponentially with distance into the bubble but they propagate along the bubble-liquid interface on both sides of the laser incidence point to reach the silicon substrate. These two counter-propagating evanescent waves may interfere to produce a high irradiance spot at the point of contact between the bubble and the substrate. Since the wavelength of evanescent waves is much shorter than that of the incident laser beam, the diameter of the high irradiance interference spot is expected to be much smaller than the focused spot diameter of the original laser beam. By this mechanism, the evanescent waves can produce subwavelength features such as $\sim$100 nm diameter

holes in the silicon substrate when the microdroplets do not carry any nanoparticles (Fig. 5.3a), or ∼500 nm silicon nanodots when the microdroplets carry nanoparticles (Figs. 5.3b, 5.3c).

In addition to the above-mentioned optical effects for subwavelength focusing, we postulate a new mechanism involving the effect of microfluidic cooling by the liquid of the droplet that may also contribute to the formation of the observed subwavelength features on the substrate surface (Fig. 5.6d). The nonuniform irradiance distribution of a Bessel laser beam promotes localized evaporation of the droplet with much higher evaporation rate in a small region around the center of the laser beam than the peripheral low irradiance region. Due to this nonuniform evaporation, a vapor-filled cavity of small diameter can form in the central region of the beam and this cavity is surrounded by liquid. Under this microfluidic environment at the substrate surface, the liquid flows towards the vapor cavity to cool down the substrate and thus constraints the laser heating of the substrate to a very small area which may be of subwavelength-diameter. The flow of liquid may be induced by three types of force: the gravitational force due to the height of the liquid film, the interfacial force due to interfacial tension between the liquid and the substrate, and the thermo-capillary force due to temperature gradient of the surface tension at the vapor-liquid interface (Fig. 5.6d). This mechanism of limited laser heating can produce subwavelength holes (Fig. 5.3a) or Ge and Si nanodots (Figs.5.3b and 5.3c).

5.3 Thin-film deposition and characterization

The ability of a microdroplet to carry nanoparticles and simultaneously act as a superlens makes the process of Fig. 5.1 versatile. This process is not restricted to depositing just nanodots since the process can be scaled to producing thin films if the processing conditions are changed.

Thin layers of germanium (Ge), silicon (Si), and silver (Ag) were deposited with ranges from approximately 5 to 100 μm in thickness on flexible and rigid surfaces . Nanoparticles of these materials were sintered and attached onto substrates, such as Si wafer, textured cardstock, and polyimide film. The range of laser power was varied between 5 - 17 W, while the laser beam diameters on the substrate surface was varied between 285 μm - 3 mm depending on the type of nanoparticle and substrate used. The flow rate of suspensions used in these cases ranged from 50 to 100 μl/min and the substrate speed from 0.1 to 1 mm/s.

5.3.1 Thin-film deposition on flexible and rigid substrates

A thin line of Ge is deposited on a silicon substrate as shown by the SEM image in Fig. 5.7. This line is approximately 50 μm wide and was produced by depositing a new layer after the previous one for three times using microdroplets of 10 wt% Ge suspension in DI water at a flow rate of 50 μl/min and an input laser power of 17 W. Larger thin films can also be deposited on textured flexible substrates such as cardstock material as shown in Figs. 5.8a through 5.8e. The inherent advantage of this technique allows a localized heating without affecting the entire work substrate.

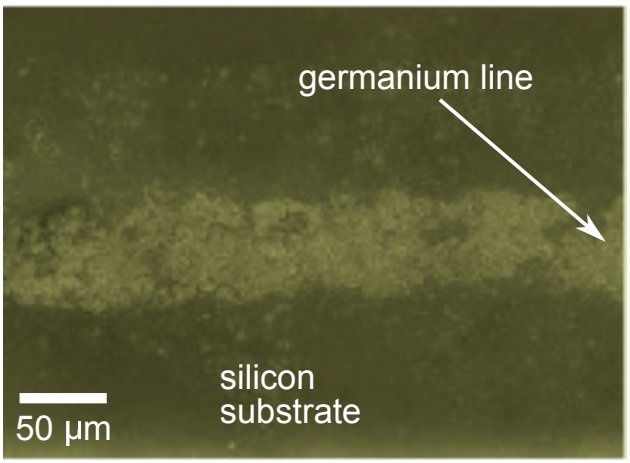

Figure 5.7: Deposition of a Ge microlayer on a smooth Si substrate. SEM image of a microlayer of Ge on Si substrate realized by the laser electrospray system. Feature of approximately 50 μm wide produced by the deposition of microdroplets of suspension of Ge, 10 wt% in DI water at flow rate of 50 μl/min and an input laser power of 17 W. The microlayer was constructed depositing a new layer after the previous one for three times.

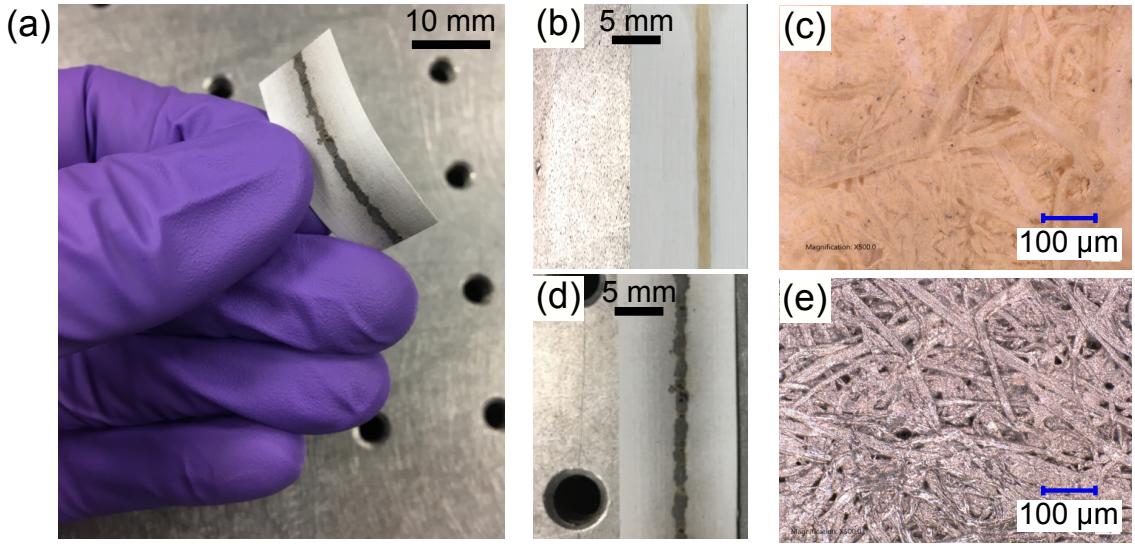

Figure 5.8: Deposition of lines of nanoparticles on a textured substrate. (a) Bending test of a line of Ag deposited on a textured substrate (cardstock). (b), (c) Deposition of a Si line on textured cardstock. Feature of approximately 2 mm wide produced by the deposition of microdroplets of suspension of Si, 20 wt% in DI water at flow rate of 100 μl/min and an input laser power of 8 W. (d), (e) Deposition of Ag line on textured cardstock. Feature of approximately 2 mm wide produced by the deposition of microdroplets of suspension of Ag, 20 wt% in DI water at flow rate of 100 μl/min and an input laser power of 13 W.

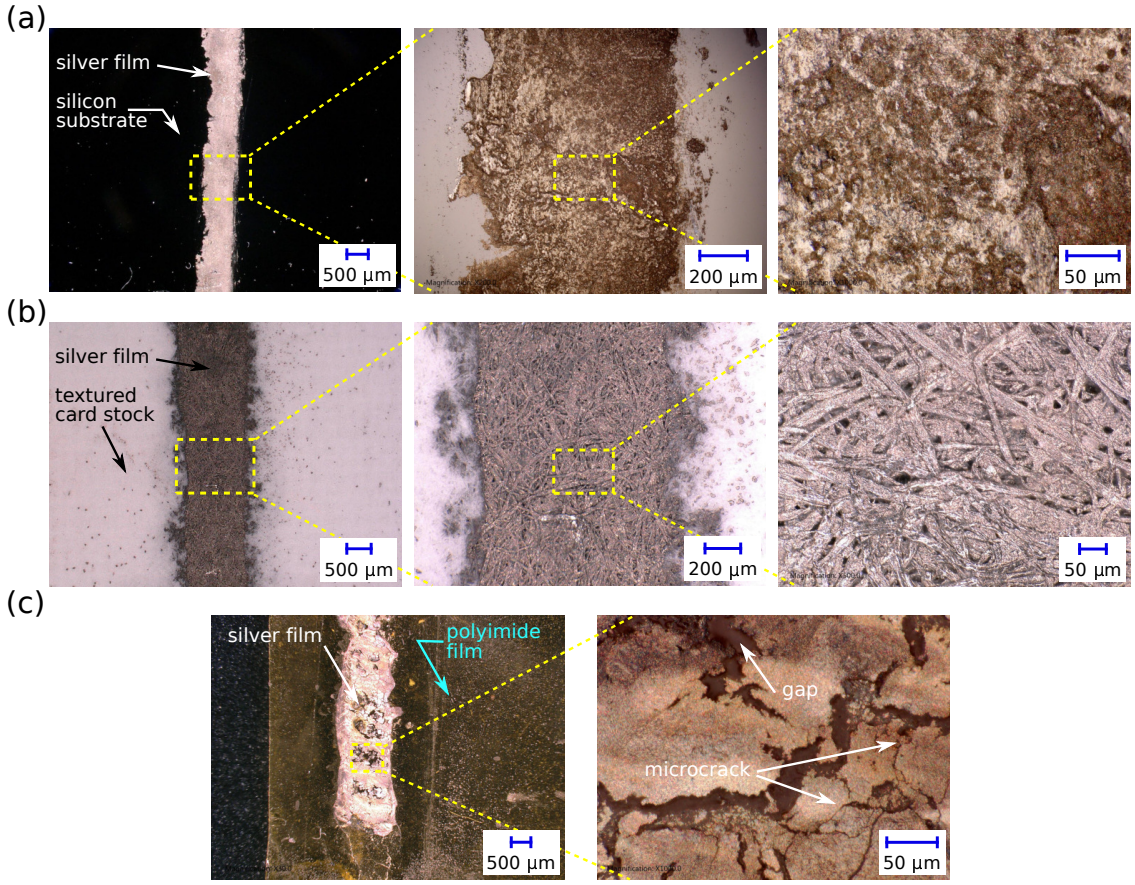

Figure 5.9: Deposition of Ag on different types of substrates. (a) Photomicrographs of deposition of silver on rigid silicon substrate. (b) Photomicrographs of deposition of Ag on textured cardstock substrate. (c) Photomicrographs of deposition of Ag on flexible polyimide film.

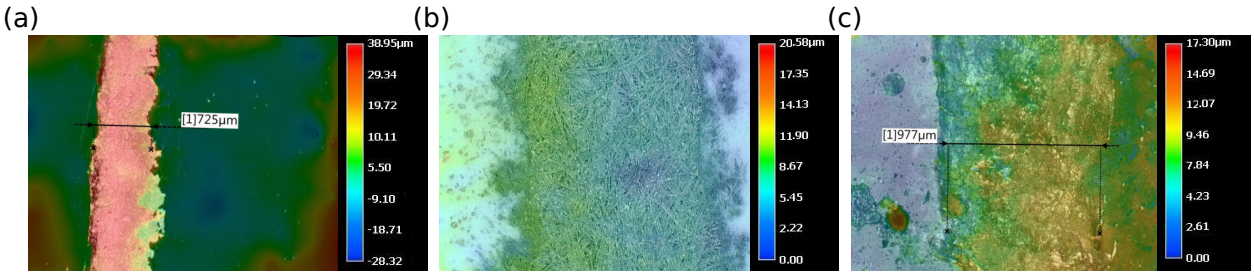

Figure 5.10: Three-dimensional construction of Ag deposition on (a) Si substrate. (b) cardstock substrate, and (c) polyimide film.

Moreover, conductive material can also be patterned in the form of microlayers. Continuous conductive lines are realized by depositing microdroplets of silver nanoparticle suspensions produced by the electrospray in microdripping mode and simultaneous laser heating in the power range of 5 to 17 W.

Figure 5.9 shows the deposition of silver nanoparticles on different types of substrates. Microdroplets with average size between 90 to 150 μm were deposited at frequency between 400 to 420 droplets per second. Fig. 5.9a presents photomicrographs of deposition of silver on a silicon wafer of thickness 275 μm. This solid line was built by depositing multiple layers of silver. The process was repeated a total of 4 times to ensure that the silver nanoparticles got attached to this substrate. Additionally, ultrasonication at 20 kHz for 10 min was used to clean the silicon substrate after the experiment was finished in order to remove the excess nanoparticles that were not completely sintered during the fabrication process. Fig. 5.9b exhibits the deposition of nanoparticles on a flexible textured cardstock of thickness 305 μm. For this case, the size of the droplets was increased

compared to that of a silicon substrate and the laser had to be defocused to produce a laser spot size of approximately 3 mm in diameter. This was needed in order to provide faster substrate cooling and a lower power intensity on the cardstock to prevent it from burning. The silver nanoparticle deposition creates a coating on the fibers rather than a solid uniform layer; however, the result is a conductive line (see Table 5.2). Fig. 5.9c shows deposition of nanoparticles on a flexible polyimide film of thickness 30 μm. This substrate was the most challenging for this laser deposition process, because of the nature of this material. The polyimide film, also known as kapton, is a strong electrical insulator and possesses hydrophobic properties. These two properties oppose a smooth and regular deposition of nanosuspension microdroplets, since the generation process is based on the electric field between the capillary tube and the substrate; and on the spread of droplets to form a uniform liquid film. Nonetheless, nanoparticles were added to the flexible film, however irregularities, such as gaps and microcracks were present on the thin film depositions. This kind of irregularities increase significantly the resistivity of the microlayers as it can be seen in Table 5.2.

Figure 5.10 shows a three-dimensional construction of silver deposition on a silicon wafer, cardstock, and polyimide film. The color range in these figures denote the height of the film deposition of nanoparticles. The deposition on a silicon rigid substrate has a thickness of approximately 16 μm. The deposition on flexible substrates, i.e. cardstock and polyimide have thicknesses of approximately 20 μm and 14 μm, respectively. For the deposition on flexible substrates, the thermal penetration depth within the nanoparticles was less than thickness of the solid layer, so there was no damage to the textured cardstock and polyimide substrate.

5.3.2 Thin-film deposition on large areas

Thin films of larger surface area were also constructed by depositing lines next to each other to form a horizontal plane and by depositing a new layer after the previous one, thus following a technique similar to a 3D printing process. Fig. 5.11 shows a deposition of Ag on a Si substrate. The feature is approximately 15 mm x 15 mm x 70 μm thick and was produced by depositing microdroplets of suspension of Ag 20 wt% in DI water at flow rate of 50 μl/min and an input laser power of 13 W. The film was constructed by depositing 60 lines next to each other every 250 μm and depositing a total of eight vertical layers. It can be observed from the images that the sintered Ag nanoparticles form beads like weld beads.

Figure 5.12 shows a deposition of Si nanoparticles on a Si wafer. The feature is approximately 15 mm x 15 mm x 25 μm thick and was produced by depositing microdroplets of suspension of Si 20 wt% in DI water at flow rate of 50 μl/min and an input laser power of 17 W. The film was constructed by depositing 60 lines next to each other every 250 μm and depositing a total of eight vertical layers (similar to the procedure used to build the Ag film). The photomicrographs of the Si film show crystallites of sizes between 18 - 23 μm.

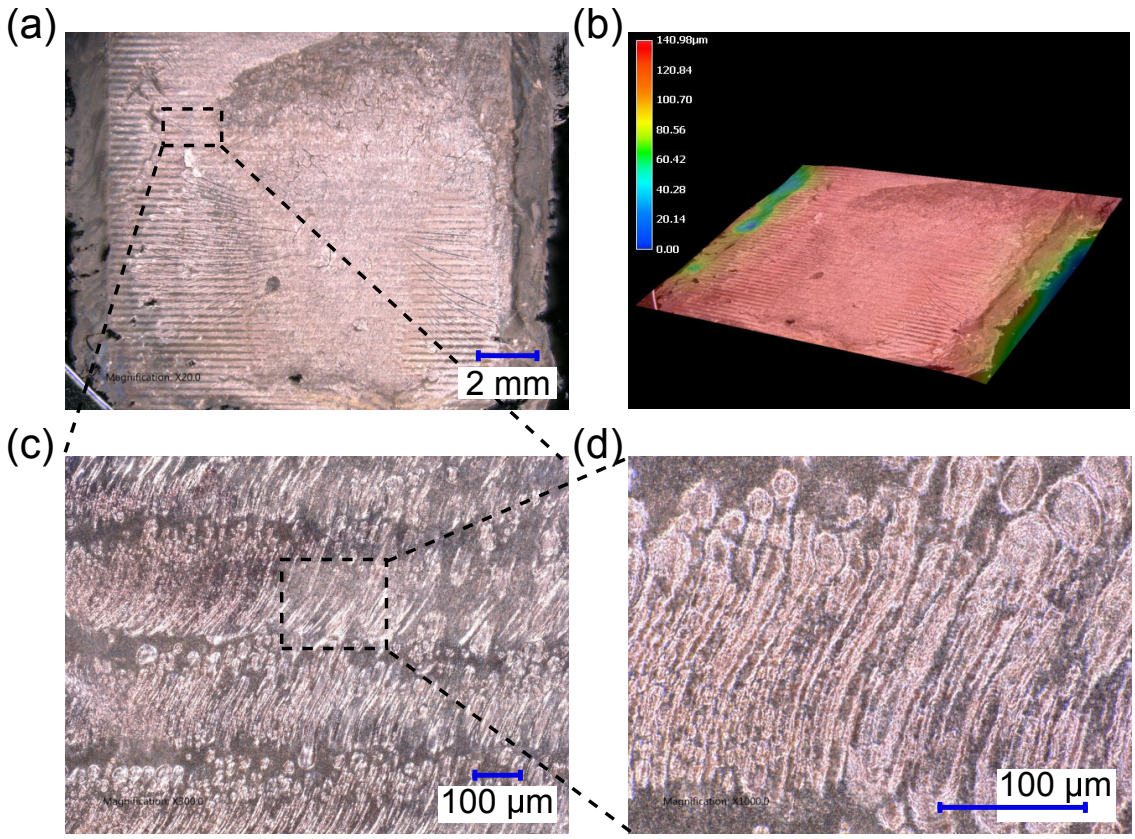

Figure 5.11: Deposition of a thin film of Ag on a Si substrate. (a) Thin film of Ag on Si substrate realized by the laser electrospray system. Feature of approximately 15 mm x 15 mm x 70 μm thick produced by the deposition of microdroplets of suspension of Ag, 20 wt% in DI water at flow rate of 50 μl/min and an input laser power of 13 W. The film was constructed by depositing 60 lines next to each other every 250 μm and depositing a new layer after the previous one for eight times. (b) Three-dimensional construction of film shown in a. (c), (d) Photomicrographs of the film shown in a at higher magnifications. Sintered nanoparticles form beads like weld beads.

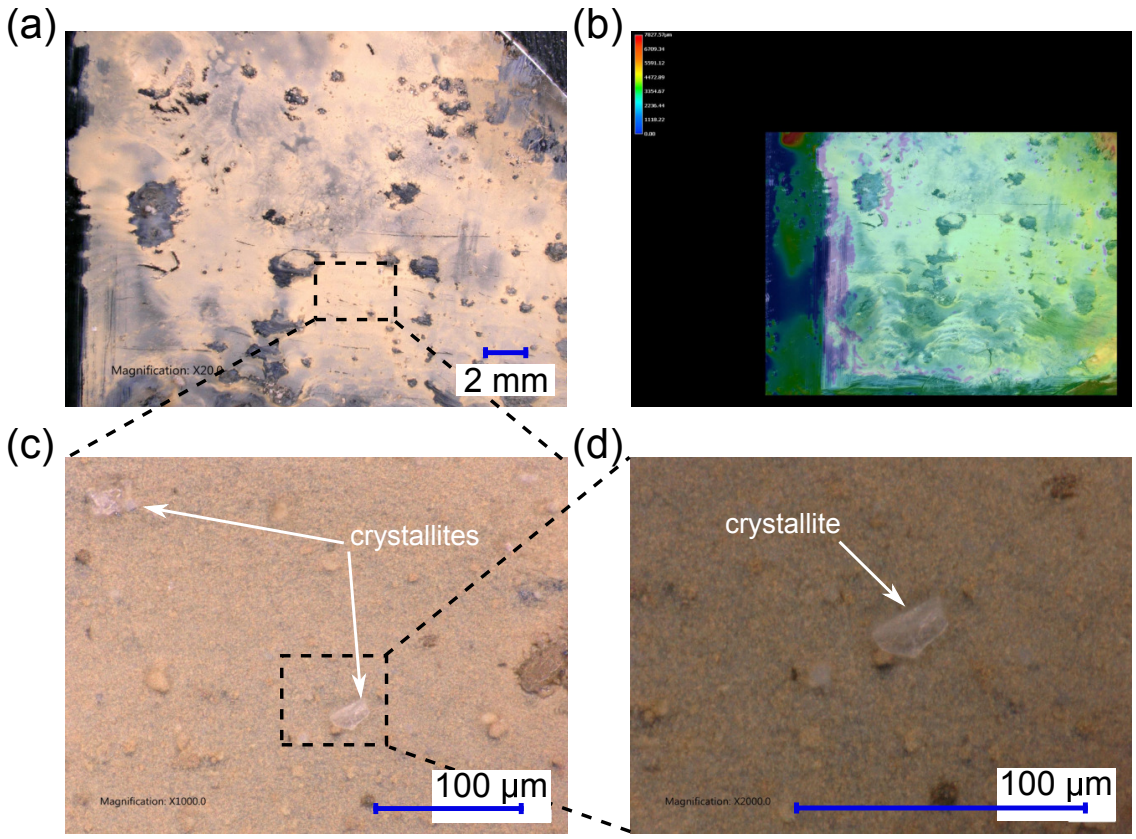

Figure 5.12: Deposition of a thin film of Si on a Si substrate. (a) Thin film of Si on Si substrate realized by the laser electrospray system. Feature of approximately 15 mm x 15 mm x 25 μm thick produced by the deposition of microdroplets of suspension of Si, 20 wt% in DI water at flow rate of 50 μl/min and an input laser power of 17 W. The film was constructed by depositing 60 lines next to each other every 250 μm and depositing a new layer after the previous one for eight times. (b) Three-dimensional construction of film shown in a. (c), (d) Photomicrographs of the film shown in a at higher magnifications showing 18 - 23 μm sized crystallites on the film.

5.3.3 Microstructural characterization and laser-sintered nanoparticles

Figures 5.13a and 5.13b is a compositional analysis of a Ge line by an energy-dispersive X-ray spectroscopy (EDS), showing the presence of carbon (C), oxygen (O), sodium (Na), Ge and Si, and confirming the deposition of Ge by the laser electrospray process. The presence of C is due to the carbon tape used to attach the sample to the sample holder of the SEM instrument. The presence of O may be due to the surrounding atmosphere since the deposition experiment was performed in an open atmosphere, or due to the native oxide SiO_2 on the Si substrate. The source of Na is traced to the surfactant (sodium dodecyl sulfate) and dispersant (sodium salt of poly-naphthalene sulfonic acid) that were used to keep the Ge nanoparticles suspended in DI water. Figs. 5.13c and 5.13d are SEM images at a higher magnification displaying the microstructures of the Ge line, where a solid line of Ge is deposited on a Si substrate by sintering Ge particles of size ranging from 100 nm to 40 μm by laser sintering the particles but not melting the substrate. Due to this wide range of the particle size in the initial suspension, the Ge film exhibits nanostructures as well as microstructures in Fig. 5.7d.

Figure 5.14 shows SEM images of the sample shown in Fig. 5.12a at different magnifications, where the formation of a nanoformed Si film can be observed. These SEM images show a continuous coalesced film. The heating caused by the laser provokes the interfacial fusion of the 30-nm Si nanoparticles to form clusters and finally the film. The sample was sputtered with gold for 30 seconds before taking SEM images.

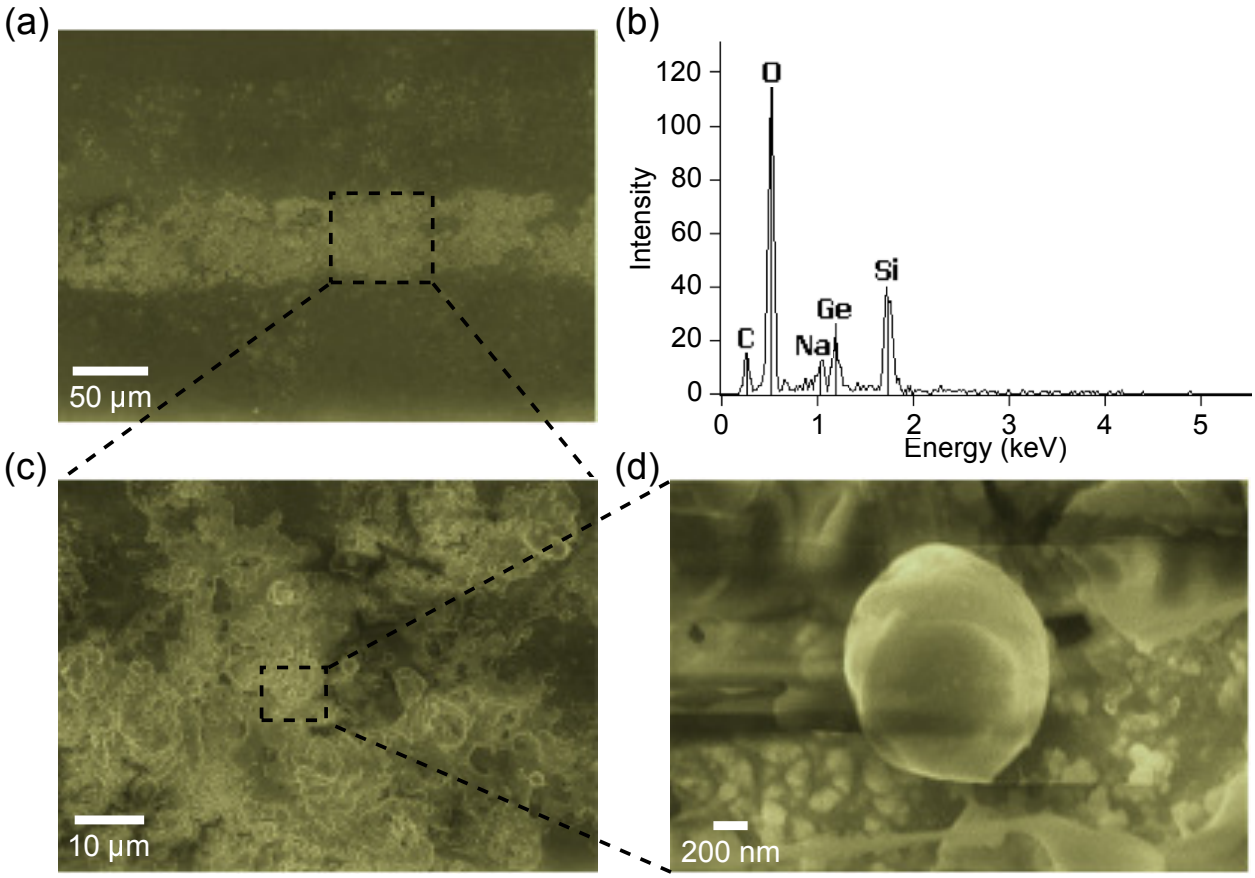

Figure 5.13: Deposition of a Ge microlayer on a smooth Si substrate. (a) SEM image of a microlayer of Ge on Si substrate realized by the laser electrospray system. Feature of approximately 50 μm wide produced by the deposition of microdroplets of suspension of Ge, 10 wt% in DI water at flow rate of 50 μl/min and an input laser power of 17 W. The microlayer was constructed depositing a new layer after the previous one for three times. (b) EDS analysis of the nanoformed germanium shown in a. (c), (d) SEM images at a higher magnification.

Figure 5.15 shows SEM images of the sample shown in Fig. 5.11a at different magnifications, where the formation of a nanoformed Ag film can be observed. Images at a higher magnification show a continuous coalesced film. The heating caused by the laser induces the interfacial fusion of the 25-nm Ag nanoparticles to form clusters and finally the film. An EDS analysis (Fig. 5.16) confirms the presence of Ag on the sample. The spectrum shows the predominance of Ag over other elements such as Si and O.

Sintering of nanoparticles is enhanced as the power of the laser beam is increased. Fig. 5.17 shows optical photomicrographs of thin films of Ag of approximately 20 μm thick (Fig. 5.18) constructed under the same conditions, but varying the power of the laser used to evaporate the liquid and sinter the nanoparticles. The sample that was treated with a lower laser power shows less uniformity on the surface compared to the sample treated with higher laser power. This non-uniformity of the films may be caused by the shrinkage during the sintering process when the liquid is evaporated. Figs 5.17a, b, and c present samples processed at 5, 9, and 13 W, respectively. Smoother texture of the film was achieved as the laser power was increased. These observations are in agreement with similar techniques based on pulsed laser sintering processes [25, 142]. Therefore, the degree of coalescence depends on the laser power.

Furthermore, examination of the samples in SEM (Fig. 5.19) show that the interfacial fusion of the nanoparticles is improved by increasing the heat input. Figs. 5.19a, b, and c correspond to the thin films constructed with laser power of 5, 9, and 13 W, respectively. The latter case being the most continuous coalesced film. It can be observed that as the power laser is magnified, the individual area of the nanoparticles is reduced, thus, decreasing the porosity of the thin layer. The

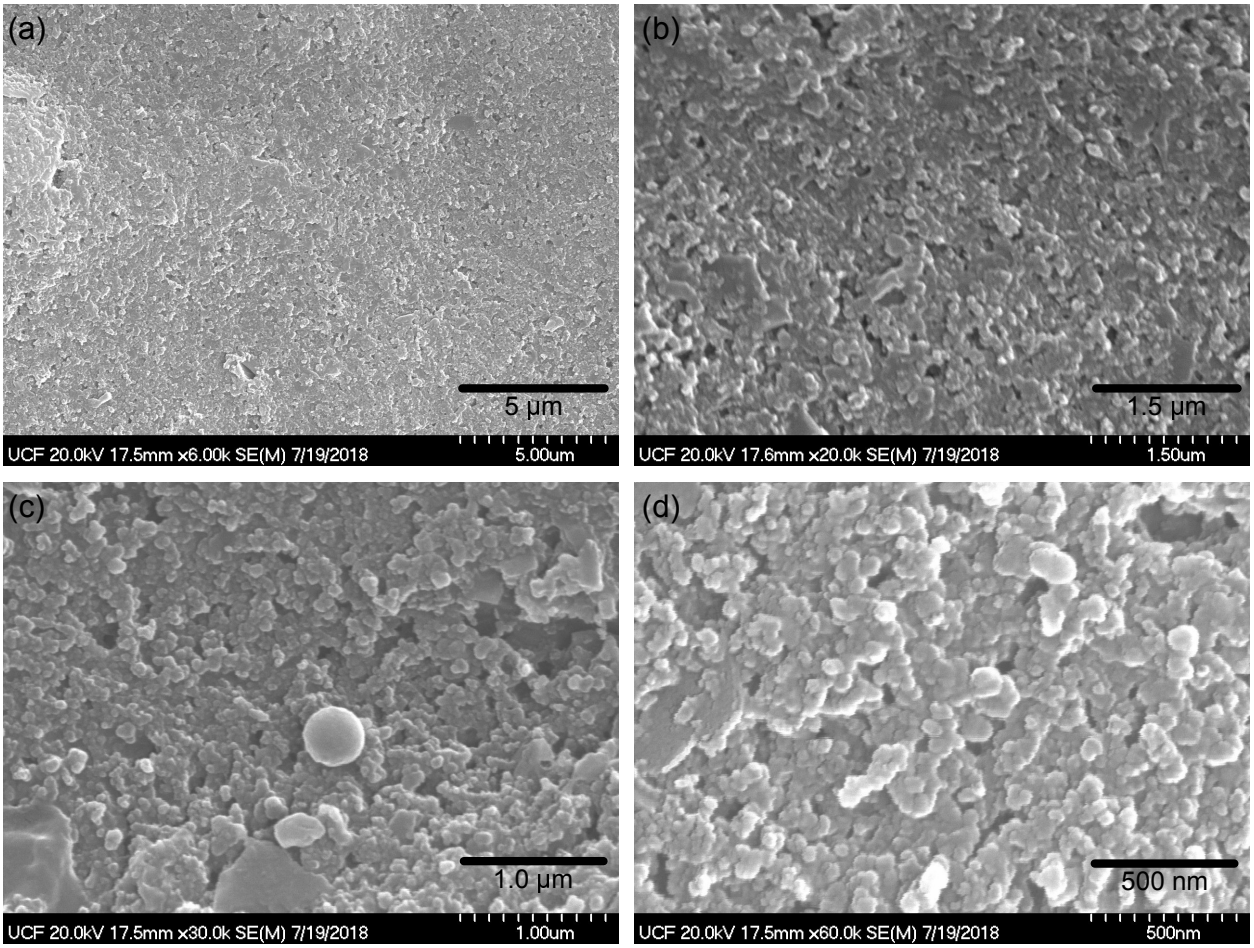

Figure 5.14: SEM images of a nanoformed Si film on a Si substrate. (a) Image of the Si film at low magnification. (b), (c), (d) Images at a higher magnification. Coalescence of 30-nm nanoparticles form clusters and the film due to the action of the laser.

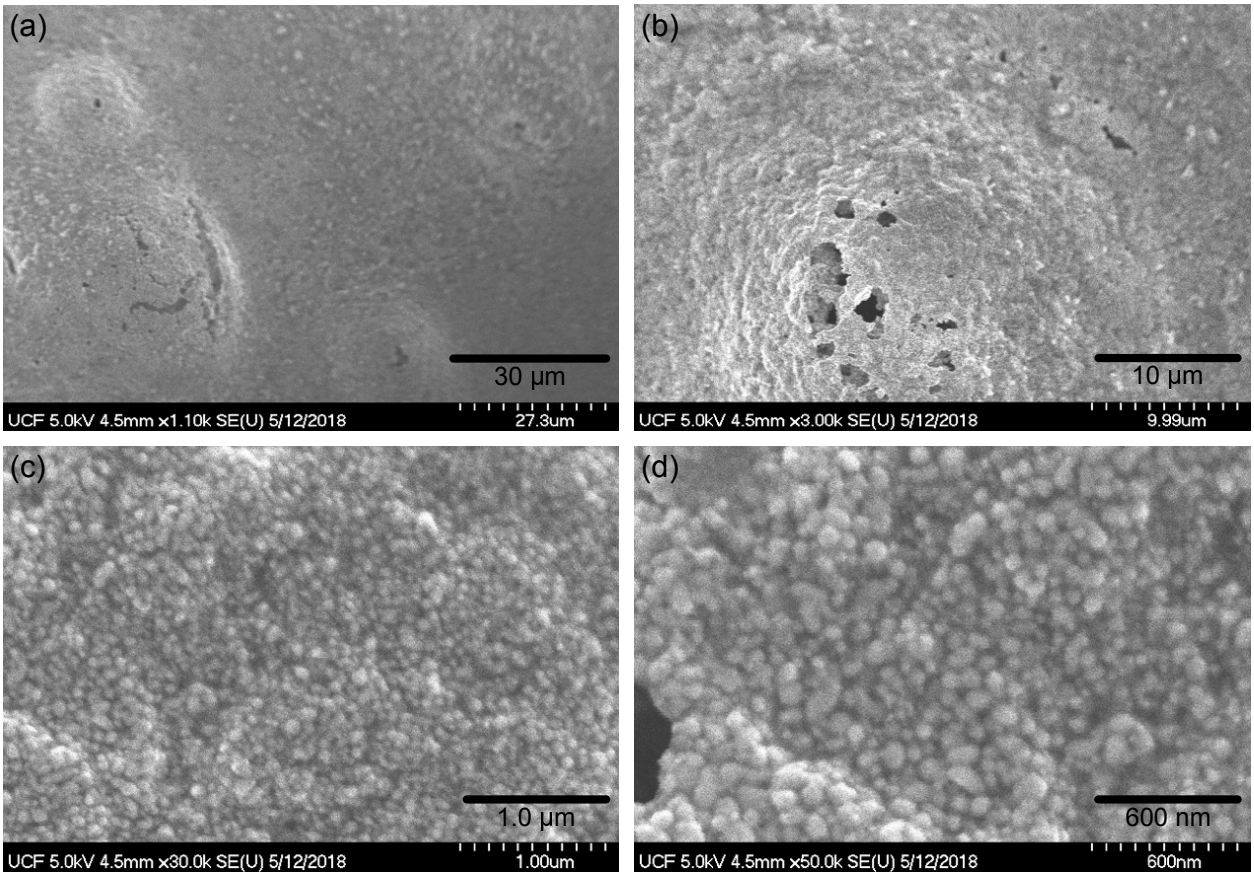

Figure 5.15: SEM images of a nanoformed Ag film on a Si substrate. (a) Image of the Ag film at low magnification. (b) Formation of micropores during the laser sintering process. (c), (d) Images at a higher magnification. Coalescence of 25-nm nanoparticles form clusters and the film due to the action of the laser.

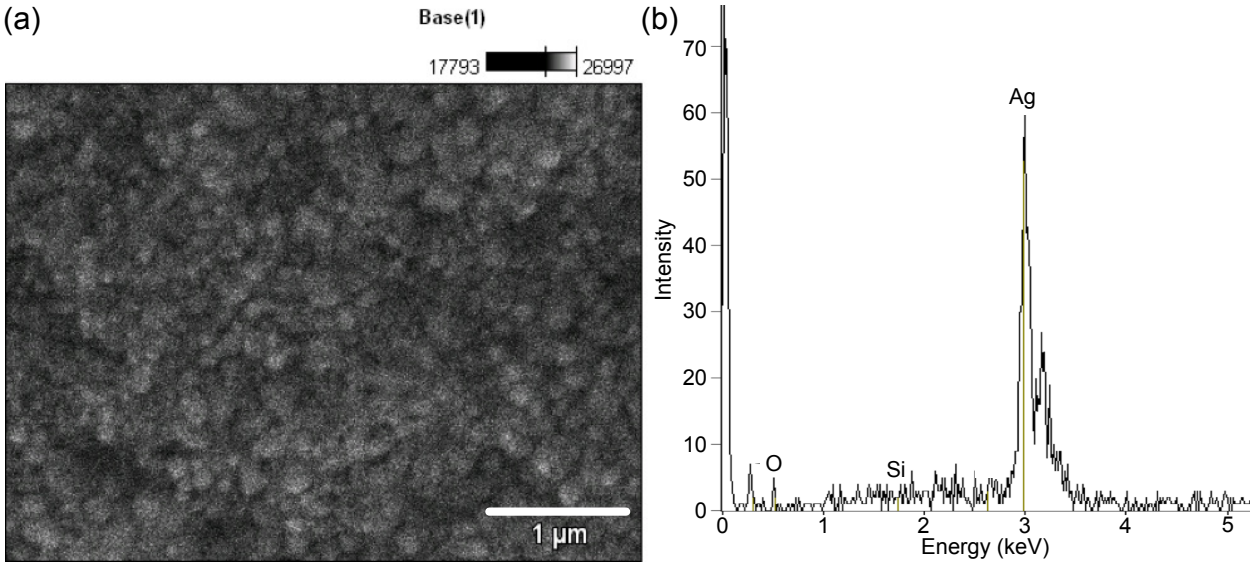

Figure 5.16: EDS analysis of a nanoformed Ag film on a Si substrate. (a) Image of the sample. (b) EDS spectrum of the sample shown in a.

grain size of the sintered layers is estimated by analyzing the SEM images and ranges between 50 - 500 nm.

Thin films of nanoparticles were constructed scanning the laser at speeds in the order of $\sim$1 mm/s. Lowering the scanning speed below 0.1 mm/s at the same laser power caused the layers to crack and to subsequently break into fine portions of sintered material that could easily be peeled off the substrate.

5.3.4 Electrical characterization of thin films

The resultant laser-sintered silver nanoparticle film showed good electrical and mechanical properties with a faster fabrication time when compared to thermal cured samples. The resistivity of laser-sintered silver for the silicon substrate, cardstock, and polyimide film is calculated to be 1.52 x 10^{-6} Ωm, 2.58 x 10^{-4} Ωm, and 0.14 Ωm, respectively. Although high when compared with that of the bulk material at 20 °C, i.e. 1.629 x 10^{-8} Ωm [143], the silver film on a silicon substrate compares well with the resistivity of that of thermal cured silver, e.g, 1.10 x 10^{-6} Ωm for deposition of silver ink on glass and thermal curing at a temperature of 140 °C for 30 min [144].

Table 5.2 shows the resistivity of silver obtained by depositing nanoparticles on the fly at a speed of 1 mm/s using the method described in this study and results obtained by others on similar substrates using different methods of deposition and subsequent thermal curing. The values for resistivity for thermal cured silver are adapted from other studies [144, 145]. $^{(*)}$ corresponds to a film of 1 cm x 1 cm x 12 μm thick, formed by doctor blading silver ink on a glass substrate and

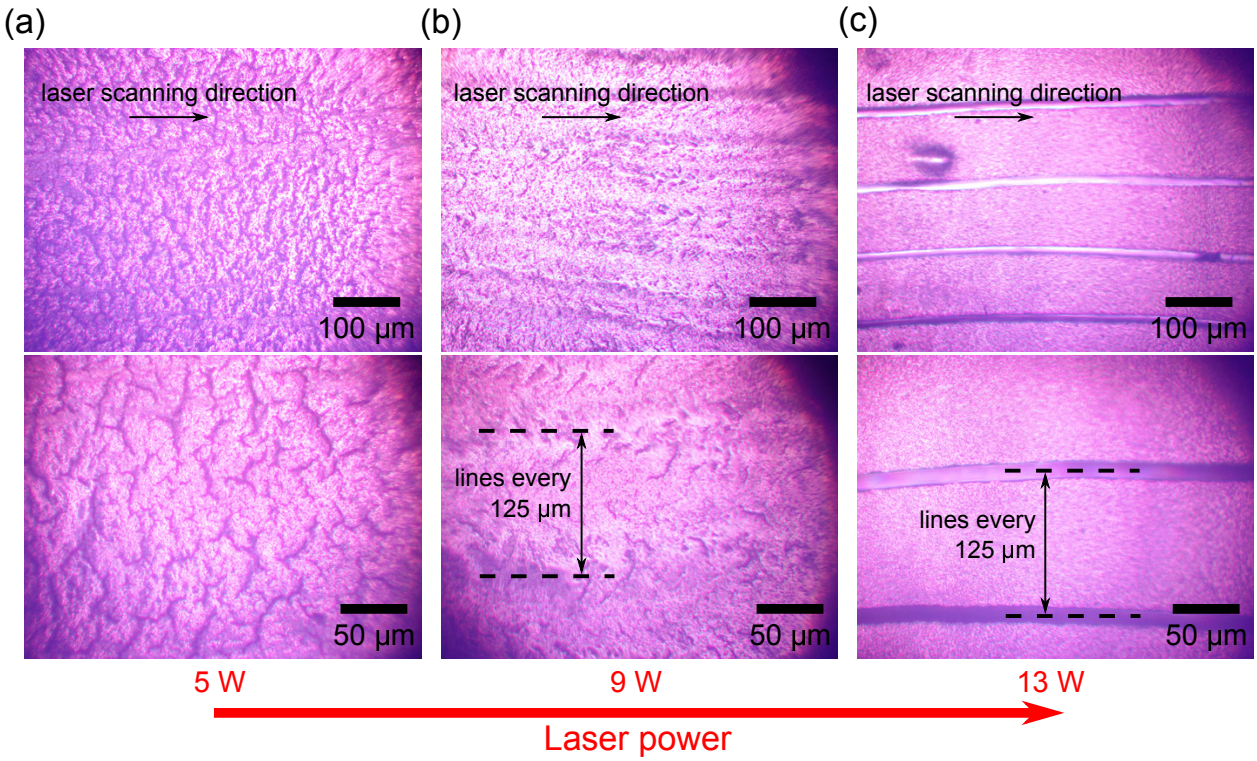

Figure 5.17: Photomicrographs of thin films of Ag that were constructed under the same conditions, but varying the laser power. Scanning speed of the laser at 1 mm/s, diameter of the beam 285 μm, and power of (a) 5 W, (b) 9 W, and (c) 13 W at low and high magnifications in an optical microscope.

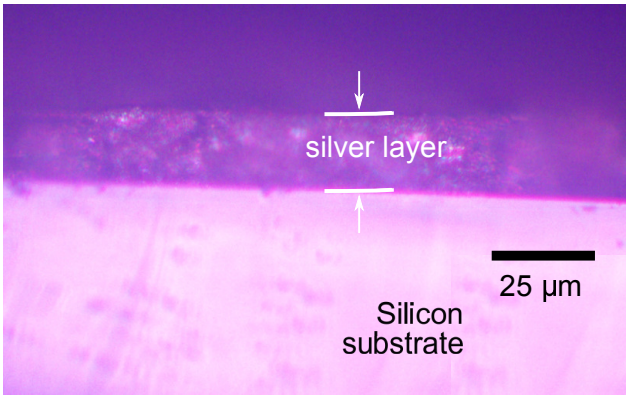

Figure 5.18: Photomicrograph of the cross section of Ag film deposited on top of a Si substrate. The microlayer of approximately 20 μm in thickness was constructed by scanning the laser of 13 W at a speed of 1 mm/s.

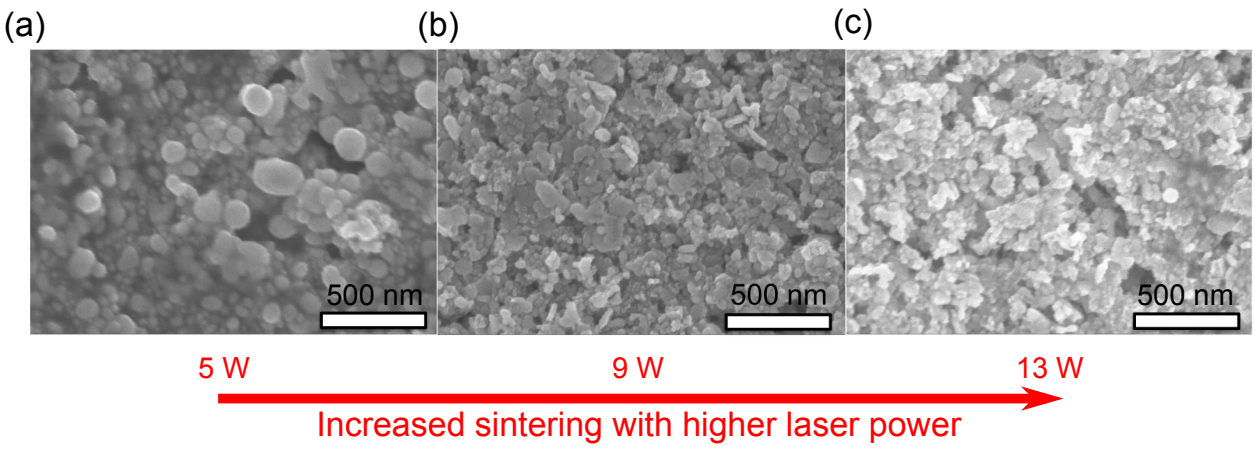

Figure 5.19: SEM images of thin films of Ag that were constructed under the same conditions, but varying the laser power. Scanning speed of the laser at 1 mm/s, diameter of the beam 285 μm, and power of (a) 5 W, (b) 9 W, and (c) 13 W.

subsequent annealing at 140 °C for 30 min [144]. (**) corresponds to a film of 620 μm x 1.5 mm x 20 μm thick, formed by a roller ball pen on Xerox paper and dried at room temperature for 24 hours in air [144]. (***) corresponds to a silver ink pattern of 15 μm thick on polyimide (thickness 125 μm), produced by screen printing method and subsequent thermal curing at 120 °C for 30 min [145].

The effect of the laser power on the electrical resistivity of thin films is shown in Table 5.3. The three cases presented in this table correspond to films of 13 mm x 13 mm x 25 m thick of silver nanoparticles sintered on a silicon substrate. The samples were sintered at laser power of 5, 9, and 13 W and a laser beam diameter of 285 m. Results show that as the laser power is increased, the sheet resistance and therefore the electrical resistivity of the samples decreases. The electrical resistivity of thin films was measured using a four-probe technique. It should be noticed that dehydration in desiccator for 24 hours at 120 °C did not decrease the resistivity significantly. Therefore, the films were already sintered at the moment of characterization.

5.4 Summary

It has been demonstrated in this Chapter, an interdisciplinary mechanism to achieve subwavelength focusing in a laser process. In this process, microdroplets perform dual roles of carrying nanoparticles and simultaneously acting as superlenses for subwavelength focusing. The microdroplets are generated from a suspension of nanoparticles using an electrospray technique and the superlens characteristic of these microdroplets is attributed to three optical phenomena such as Maxwell's

Thin film	Deposition conditions	Electrical resistivity (Ωm)		
		As-deposited line	Annealed sample	Bulk material
Ag on Si	laser power: 13 W spot size: 0.285 mm flow rate: 50 μl/min	1.52×10^{-6}	$^{*}1.1 \times 10^{-6}$ (30 min at 140 °C)	1.629×10^{-8}
Ag on cardstock	laser power: 13 W spot size: 3.0 mm flow rate: 100 μl/min	2.58×10^{-4}	$^{**}4.13 \times 10^{-6}$ (24 hr at 25 °C)	1.629×10^{-8}
Ag on polyimide film	laser power: 9 W spot size: 3.0 mm flow rate: 100 μl/min	0.14	$^{***}1.05 \times 10^{-6}$ (30 min at 120 °C)	1.629×10^{-8}

Table 5.2: Comparison of the electrical resistivity of the silver nanoparticle thin films treated under various conditions and bulk material.

$^{(*)}$ film of 1 cm x 1 cm x 12 μm thick, formed by doctor blading Ag ink on a glass substrate and subsequent annealing at 140 °C for 30 min [144]. $^{(**)}$ film of 620 μm x 1.5 mm x 20 μm thick, formed by a roller ball pen on Xerox paper and dried at room temperature for 24 hours in air [144]. $^{(***)}$ Ag ink pattern of 15 μm thick on polyimide (thickness 125 μm), produced by screen printing method and subsequent thermal curing at 120 °C for 30 min [145]

Thin film	Deposition conditions	Sheet resistance (Ω.cm^{-2})	Electrical resistivity (Ω.m)
Ag on Si	laser power: 5 W spot size: 0.285 mm flow rate: 50 μl/min	13	2.30x10^{-4}
Ag on Si	laser power: 9 W spot size: 0.285 mm flow rate: 50 μl/min	1.9	3.40x10^{-5}
Ag on Si	laser power: 13 W spot size: 0.285 mm flow rate: 50 μl/min	0.46	8.28x10^{-6}

Table 5.3: Comparison of the sheet resistance and electrical resistivity of thin films of silver that were constructed under the same conditions, but varying the laser power.

fish eye lens or Lüneberg lens, evanescent waves by laser scattering, and evanescent waves by the total internal reflection principle. A microfluidic cooling effect can also contribute to creating subwavelength features. While this process is demonstrated to produce subwavelength holes and nanodots, the process is scalable to produce thin lines and microlayers of semiconductor materials by an additive manufacturing technique. Results show that tiny features with high resolution can be created by squeezing a laser beam of wavelength $\lambda = 1064$ nm into subwavelength regions up to $\lambda/10$, thus overcoming the diffraction limit. This process extends the application of infrared lasers to the production of nanostructures and features, and, therefore, provides a novel technology for nanomanufacturing.

Moreover, the deposition of silver thin films on rigid and flexible substrates has been achieved through a nanoparticle electrospray laser deposition process. The use of nanoparticles and simultaneous laser sintering provides a unique means of depositing thin films on various types of substrates. Although the electrical resistivity of the samples produced by this process is lower in comparison with that of the bulk material, the resistivity of silver films created on a silicon substrate compare well with those produced by thermal annealing. The resultant laser-sintered silver nanoparticle microlayers deposited on a solid silicon wafer showed good electrical and mechanical properties with a faster fabrication time when compared to thermal cured samples. In the deposition on flexible substrates, the thermal penetration depth within the nanoparticles was less than the thickness of the solid layer, so there was no damage on the textured cardstock substrate and polyimide film. To prevent the flexible films from burning, the laser intensity needs to be lowered by defocusing the laser. This also hinders the effectiveness of the laser sintering process, thus,

yielding higher electrical resistivity as it is shown in Table 5.2. Nonetheless, the time in which nanoparticles can be sintered is vastly superior, with depositions on the fly at speeds up to 1 mm/s.

CHAPTER 6
CONCLUSION

Modes of nanosuspensions containing semiconductor nanoparticles have been studied in laminar electrospray of droplets. A suitable microdripping mode has been observed, which can be utilized for depositing monodisperse microdroplets via electrospray. This technique allows an innovative approach for manufacturing energy, optical and electronic devices. A regime map is provided for identifying the limits to operate the EHD process under the microdripping mode to achieve uniform monodisperse microdroplets. An increase in nanoparticle concentration increases the liquid viscosity, which dampens the growth of perturbation and delays the jet breakup in the microdripping mode. However, viscosity does not affect the drop size in the dripping mode. For a given flow rate, the transition between ellipsoidal and conical meniscus regimes is found to occur at $Ca_e \approx 1.0$. The dripping mode occurs for $Ca_e < 1$ when the droplet size strongly depends on the electric field strength compared to the droplets of a nearly constant radius at $r^* = 0.1$ and $r^* = 0.07$ generated in microdripping and oscillating microdripping modes for a flow rate $Q = 1.67$ mm^3/s. Thus, the average droplet size can be determined using these results if the variables that define the electric capillary number and the radius of the droplet (r_0) in the absence of electric field are known. Electrical conductivity affects the transition between microdripping and oscillating microdripping modes. The onset of oscillating microdripping mode occurs first for suspensions with

higher conductivity. Ejection of uniform microdroplets in the microdripping mode is observed in the range $2.0 \leq Ca_e \leq 2.5$ and the oscillating microdripping mode is reached at $Ca_e \geq 3.3$ for all the nanoparticle suspensions of this study.

Electrohydrodynamic inkjet printing of semiconductor nanoparticle suspensions can be accomplished by the operation of an electrospray in microdripping mode and is more efficient than conventional inkjet printing. The effect of the physical properties on the droplet size and frequency of droplet formation is more precisely described by the relative influence of all the acting forces. A scaling analysis has yielded a parameter, $Ca_e/\sqrt{Bo(1+Ca)}$. Results for all suspensions with a wide range of viscosity show that r^* can be correlated using this parameter in both dripping and microdripping modes. The same parameter also correlates the normalized frequency of droplet formation as an increasing function in the microdripping mode. Viscosity affects the shape of the cone by resisting its deformation and thus promoting a stable microdripping mode. Reduction in surface tension decreases the drop size in dripping and microdripping modes. However, the capillary size and electrical conductivity have minimal effect on the size of the ejected droplets. Based on the analysis, it is possible to design the electrospray to produce uniform monodisperse droplets by manipulating the voltage at the electrode, for any desired nanoparticle concentration of a suspension to be sintered on a substrate.

An interdisciplinary mechanism involving optical effect for subwavelength focusing and microfluidic cooling effect for subwavelength laser heating has been identified in this study as an important laser-microdroplet interaction for next-generation technology development. The novelty lies in the dual role of each electrosprayed microdroplet that carries nanoparticles to the substrate

surface and simultaneously acts as a superlens to focus a laser beam to a subwavelength diameter. The microdroplets are generated from a suspension of nanoparticles using an electrospray technique and the superlens characteristic of these microdroplets is attributed to three optical phenomena such as Maxwell's fish eye lens or Lüneberg lens, evanescent waves by laser scattering, and evanescent waves by the total internal reflection principle. A microfluidic cooling effect can also contribute to creating subwavelength features. Results show that tiny features with high resolution can be created by squeezing a laser beam of wavelength $\lambda = 1064$ nm into subwavelength regions up to $\lambda/10$, thus overcoming the diffraction limit. While this process is demonstrated to produce subwavelength holes and nanodots of semiconductor materials such as silicon and germanium, the process is scalable to produce thin lines and microlayers of semiconductor and conductive materials by an additive manufacturing technique. The use of nanoparticles and simultaneous laser sintering provides a unique means of depositing thin films on various types of substrates. Although the electrical resistivity of the samples produced by this process is lower in comparison with that of the bulk material, the resistivity of conductive microlayers created on a silicon substrate compare well with those produced by thermal annealing. The resultant laser-sintered silver nanoparticle microlayers deposited on a silicon wafer show good electrical and mechanical properties with a faster fabrication time when compared to thermal cured samples. In the deposition on flexible substrates, the thermal penetration depth within the nanoparticles is less than the thickness of the solid layer, so there is no damage on textured cardstock substrate and polyimide film.

This process extends the application of infrared lasers to the production of nanostructures and features, and, therefore, provides a novel technology for nanomanufacturing and is envisaged to

evolve further for fabricating nanopatterns on flexible substrates such as papers and plastics for widespread applications including conformal solar cells and ultra-flexible electrodes in biological implants.

LIST OF REFERENCES

[1] D. R. Smith, J. B. Pendry, and M. C. Wiltshire, "Metamaterials and negative refractive index," *Science*, vol. 305, no. 5685, pp. 788–792, 2004.

[2] B. D. Gates, "Flexible electronics," *Science*, vol. 323, no. 5921, pp. 1566–1567, 2009.

[3] B. Y. Ahn, E. B. Duoss, M. J. Motala, X. Guo, S.-I. Park, Y. Xiong, J. Yoon, R. G. Nuzzo, J. A. Rogers, and J. A. Lewis, "Omnidirectional printing of flexible, stretchable, and spanning silver microelectrodes," *Science*, vol. 323, no. 5921, pp. 1590–1593, 2009.

[4] H.-H. Lee, K.-S. Chou, and K.-C. Huang, "Inkjet printing of nanosized silver colloids," *Nanotechnology*, vol. 16, no. 10, p. 2436, 2005.

[5] J.-U. Park, M. Hardy, S. J. Kang, K. Barton, K. Adair, D. kishore Mukhopadhyay, C. Y. Lee, M. S. Strano, A. G. Alleyne, J. G. Georgiadis *et al.*, "High-resolution electrohydrodynamic jet printing," *Nature Materials*, vol. 6, no. 10, p. 782, 2007.

[6] N. M. Muhammad, S. Sundharam, H.-W. Dang, A. Lee, B.-H. Ryu, and K.-H. Choi, "Cis layer deposition through electrospray process for solar cell fabrication," *Current Applied Physics*, vol. 11, no. 1, pp. S68–S75, 2011.

[7] S. Khan, Y. H. Doh, A. Khan, A. Rahman, K. H. Choi, and D. S. Kim, "Direct patterning and electrospray deposition through ehd for fabrication of printed thin film transistors," *Current Applied Physics*, vol. 11, no. 1, pp. S271–S279, 2011.

[8] A. M. Gañán-Calvo, "Cone-jet analytical extension of taylor's electrostatic solution and the asymptotic universal scaling laws in electrospraying," *Physical Review Letters*, vol. 79, no. 2, p. 217, 1997.

[9] J. Fernández de La Mora, "The fluid dynamics of taylor cones," *Annu. Rev. Fluid Mech.*, vol. 39, pp. 217–243, 2007.

[10] A. Jaworek and A. Krupa, "Jet and drops formation in electrohydrodynamic spraying of liquids. a systematic approach," *Experiments in Fluids*, vol. 27, no. 1, pp. 43–52, 1999.

[11] W. Yang, H. Duan, C. Li, and W. Deng, "Crossover of varicose and whipping instabilities in electrified microjets," *Physical Review Letters*, vol. 112, no. 5, p. 054501, 2014.

[12] J. B. Pendry, "Negative refraction makes a perfect lens," *Physical Review Letters*, vol. 85, no. 18, p. 3966, 2000.

[13] N. Fang, H. Lee, C. Sun, and X. Zhang, "Sub–diffraction-limited optical imaging with a silver superlens," *Science*, vol. 308, no. 5721, pp. 534–537, 2005.

[14] E. T. Rogers, J. Lindberg, T. Roy, S. Savo, J. E. Chad, M. R. Dennis, and N. I. Zheludev, "A super-oscillatory lens optical microscope for subwavelength imaging," *Nature Materials*, vol. 11, no. 5, p. 432, 2012.

[15] T. Taubner, D. Korobkin, Y. Urzhumov, G. Shvets, and R. Hillenbrand, "Near-field microscopy through a sic superlens," *Science*, vol. 313, no. 5793, pp. 1595–1595, 2006.

[16] U. Leonhardt, "Perfect imaging without negative refraction," *New Journal of Physics*, vol. 11, no. 9, p. 093040, 2009.

[17] U. Leonhardt and T. G. Philbin, "Perfect imaging with positive refraction in three dimensions," *Physical Review A*, vol. 81, no. 1, p. 011804, 2010.

[18] J.-H. Park, C. Park, H. Yu, J. Park, S. Han, J. Shin, S. H. Ko, K. T. Nam, Y.-H. Cho, and Y. Park, "Subwavelength light focusing using random nanoparticles," *Nature Photonics*, vol. 7, no. 6, p. 454, 2013.

[19] H.-J. Münzer, M. Mosbacher, M. Bertsch, J. Zimmermann, P. Leiderer, and J. Boneberg, "Local field enhancement effects for nanostructuring of surfaces," *Journal of Microscopy*, vol. 202, no. 1, pp. 129–135, 2001.

[20] S. Theppakuttai and S. Chen, "Nanoscale surface modification of glass using a 1064 nm pulsed laser," *Applied Physics Letters*, vol. 83, no. 4, pp. 758–760, 2003.

[21] C. A. López and A. H. Hirsa, "Fast focusing using a pinned-contact oscillating liquid lens," *Nature Photonics*, vol. 2, no. 10, p. 610, 2008.

[22] M. Duocastella, C. Florian, P. Serra, and A. Diaspro, "Sub-wavelength laser nanopatterning using droplet lenses," *Scientific Reports*, vol. 5, p. 16199, 2015.

[23] S. Bet and A. Kar, "Thin film deposition on plastic substrates using silicon nanoparticles and laser nanoforming," *Materials Science and Engineering: B*, vol. 130, no. 1-3, pp. 228–236, 2006.

[24] J. Yeo, G. Kim, S. Hong, M. S. Kim, D. Kim, J. Lee, H. B. Lee, J. Kwon, Y. D. Suh, H. W. Kang *et al.*, "Flexible supercapacitor fabrication by room temperature rapid laser processing of roll-to-roll printed metal nanoparticle ink for wearable electronics application," *Journal of Power Sources*, vol. 246, pp. 562–568, 2014.

[25] T. Park and D. Kim, "Excimer laser sintering of indium tin oxide nanoparticles for fabricating thin films of variable thickness on flexible substrates," *Thin Solid Films*, vol. 578, pp. 76–82, 2015.

[26] A. A. Shah, C. Ungaro, and M. C. Gupta, "High temperature spectral selective coatings for solar thermal systems by laser sintering," *Solar Energy Materials and Solar Cells*, vol. 134, pp. 209–214, 2015.

[27] M. Danek, K. Jensen, C. Murray, and M. Bawendi, "Electrospray organometallic chemical vapor depositiona novel technique for preparation of ii–vi quantum dot composites," *Applied Physics Letters*, vol. 65, no. 22, pp. 2795–2797, 1994.

[28] M. G. Mali, H. Yoon, M.-w. Kim, M. T. Swihart, S. S. Al-Deyab, and S. S. Yoon, "Electrosprayed heterojunction wo3/bivo4 films with nanotextured pillar structure for enhanced photoelectrochemical water splitting," *Applied Physics Letters*, vol. 106, no. 15, p. 151603, 2015.

[29] A. Jaworek, "Micro-and nanoparticle production by electrospraying," *Powder Technology*, vol. 176, no. 1, pp. 18–35, 2007.

[30] A. Cascio, J. Lyon, M. Beerbom, R. Schlaf, Y. Zhu, and S. Jenekhe, "Investigation of a polythiophene interface using photoemission spectroscopy in combination with electrospray thin-film deposition," *Applied Physics Letters*, vol. 88, no. 6, p. 062104, 2006.

[31] J. Choi, Y.-J. Kim, S. Lee, S. U. Son, H. S. Ko, V. D. Nguyen, and D. Byun, "Drop-on-demand printing of conductive ink by electrostatic field induced inkjet head," *Applied Physics Letters*, vol. 93, no. 19, p. 193508, 2008.

[32] S. Lee, D. Byun, D. Jung, J. Choi, Y. Kim, J. H. Yang, S. U. Son, S. B. Q. Tran, and H. S. Ko, "Pole-type ground electrode in nozzle for electrostatic field induced drop-on-demand inkjet head," *Sensors and Actuators A: Physical*, vol. 141, no. 2, pp. 506–514, 2008.

[33] J. Zeleny, "The electrical discharge from liquid points, and a hydrostatic method of measuring the electric intensity at their surfaces," *Physical Review*, vol. 3, no. 2, p. 69, 1914.

[34] I. Hayati, A. Bailey, and T. F. Tadros, "Investigations into the mechanisms of electrohydrodynamic spraying of liquids: I. effect of electric field and the environment on pendant drops and factors affecting the formation of stable jets and atomization," *Journal of Colloid and Interface Science*, vol. 117, no. 1, pp. 205–221, 1987.

[35] M. Cloupeau and B. Prunet-Foch, "Electrostatic spraying of liquids in cone-jet mode," *Journal of Electrostatics*, vol. 22, no. 2, pp. 135–159, 1989.

[36] ——, "Electrostatic spraying of liquids: main functioning modes," *Journal of Electrostatics*, vol. 25, no. 2, pp. 165–184, 1990.

[37] J. Grace and J. Marijnissen, "A review of liquid atomization by electrical means," *Journal of Aerosol Science*, vol. 25, no. 6, pp. 1005–1019, 1994.

[38] E. Castillo-Orozco, A. Kar, and R. Kumar, "Electrospray mode transition of microdroplets with semiconductor nanoparticle suspension," *Scientific Reports*, vol. 7, no. 1, p. 5144, 2017.

[39] H. Watanabe, T. Matsuyama, and H. Yamamoto, "Experimental study on electrostatic atomization of highly viscous liquids," *Journal of Electrostatics*, vol. 57, no. 2, pp. 183–197, 2003.

[40] A. Barrero and I. G. Loscertales, "Micro-and nanoparticles via capillary flows," *Annu. Rev. Fluid Mech.*, vol. 39, pp. 89–106, 2007.

[41] G. Taylor, "Disintegration of water drops in an electric field," *Proceedings of the Royal Society of London. Series A. Mathematical and Physical Sciences*, vol. 280, no. 1382, pp. 383–397, 1964.

[42] S. Ogata, "The dimensionless correlation of mean particle diameter in electrostatic atomization," *Kagaku Kogaku*, vol. 3, pp. 132–136, 1977.

[43] S. Ogata, Y. Hara, and H. Shinohara, "Break-up mechanism of a charged liquid jet," *International Chemical Engineering*, vol. 18, no. 3, pp. 482–488, 1978.

[44] Y. Tomita, Y. Ishibashi, and T. Yokoyama, "Fundamental studies on an electrostatic ink jet printer: 1st report, electrostatic drop formation," *Bulletin of JSME*, vol. 29, no. 257, pp. 3737–3743, 1986.

[45] J. F. De La Mora and I. G. Loscertales, "The current emitted by highly conducting taylor cones," *Journal of Fluid Mechanics*, vol. 260, pp. 155–184, 1994.

[46] R. Hartman, D. Brunner, D. Camelot, J. Marijnissen, and B. Scarlett, "Jet break-up in electrohydrodynamic atomization in the cone-jet mode," *Journal of Aerosol Science*, vol. 31, no. 1, pp. 65–95, 2000.

[47] A. Ganan-Calvo, J. Davila, and A. Barrero, "Current and droplet size in the electrospraying of liquids. scaling laws," *Journal of Aerosol Science*, vol. 28, no. 2, pp. 249–275, 1997.

[48] A. M. Gañán-Calvo, "The surface charge in electrospraying: its nature and its universal scaling laws," *Journal of Aerosol Science*, vol. 30, no. 7, pp. 863–872, 1999.

[49] D. P. Smith, "The electrohydrodynamic atomization of liquids," *IEEE Transactions on Industry Applications*, no. 3, pp. 527–535, 1986.

[50] M. Mutoh, S. Kaieda, and K. Kamimura, "Convergence and disintegration of liquid jets induced by an electrostatic field," *Journal of Applied Physics*, vol. 50, no. 5, pp. 3174–3179, 1979.

[51] A. Jaworek and A. Sobczyk, "Electrospraying route to nanotechnology: an overview," *Journal of Electrostatics*, vol. 66, no. 3-4, pp. 197–219, 2008.

[52] Y.-Y. Noh, N. Zhao, M. Caironi, and H. Sirringhaus, "Downscaling of self-aligned, all-printed polymer thin-film transistors," *Nature Nanotechnology*, vol. 2, no. 12, p. 784, 2007.

[53] M. Ladanov, P. Algarin-Amaris, G. Matthews, M. Ram, S. Thomas, A. Kumar, and J. Wang, "Microfluidic hydrothermal growth of zno nanowires over high aspect ratio microstructures," *Nanotechnology*, vol. 24, no. 37, p. 375301, 2013.

[54] I. G. Loscertales, A. Barrero, I. Guerrero, R. Cortijo, M. Marquez, and A. Ganan-Calvo, "Micro/nano encapsulation via electrified coaxial liquid jets," *Science*, vol. 295, no. 5560, pp. 1695–1698, 2002.

[55] Á. G. Marín, I. G. Loscertales, M. Marquez, and A. Barrero, "Simple and double emulsions via coaxial jet electrosprays," *Physical Review Letters*, vol. 98, no. 1, p. 014502, 2007.

[56] Y. Tian, G. Wu, X. Tian, X. Tao, and W. Chen, "Novel erythrocyte-like graphene microspheres with high quality and mass production capability via electrospray assisted self-assembly," *Scientific Reports*, vol. 3, p. 3327, 2013.

[57] J. Mahoney and J. Perel, "Ieee/ias 1981 annual meeting, phil," *PA (October 1981)*.

[58] T.-M. Pang, P. Prewett, and L. Gowland, "Properties of silicon films produced by field emission deposition," *Thin Solid Films*, vol. 88, no. 3, pp. 219–224, 1982.

[59] S. G. Kim, K. H. Choi, J. H. Eun, H. J. Kim, and C. S. Hwang, "Effects of additives on properties of mgo thin films by electrostatic spray deposition," *Thin Solid Films*, vol. 377, pp. 694–698, 2000.

[60] S. G. Kim, J. Y. Kim, and H. J. Kim, "Deposition of mgo thin films by modified electrostatic spray pyrolysis method," *Thin Solid Films*, vol. 376, no. 1-2, pp. 110–114, 2000.

[61] D. Wang, M. Edirisinghe, and S. Jayasinghe, "Solid freeform fabrication of thin-walled ceramic structures using an electrohydrodynamic jet," *Journal of the American Ceramic Society*, vol. 89, no. 5, pp. 1727–1729, 2006.

[62] H. Duan, C. Li, W. Yang, B. Lojewski, L. An, and W. Deng, "Near-field electrospray microprinting of polymer-derived ceramics," *Journal of Microelectromechanical Systems*, vol. 22, no. 1, pp. 1–3, 2013.

[63] E. Hecht *et al.*, *Optics Fourth Edition*. Addison Wesley, 2003.

[64] S. Lipson, *H. Lipson nd DS Tannhauser, Optical Physics*. Cambridge University Press, 1998.

[65] L. Novotny and B. Hecht, *Principles of nano-optics*. Cambridge University Press, 2012.

[66] X. Zhang and Z. Liu, "Superlenses to overcome the diffraction limit," *Nature Materials*, vol. 7, no. 6, p. 435, 2008.

[67] H. Lee, Y. Xiong, N. Fang, W. Srituravanich, S. Durant, M. Ambati, C. Sun, and X. Zhang, "Realization of optical superlens imaging below the diffraction limit," *New Journal of Physics*, vol. 7, no. 1, p. 255, 2005.

[68] X. Hu and C. Chan, "Photonic crystals with silver nanowires as a near-infrared superlens," *Applied Physics Letters*, vol. 85, no. 9, pp. 1520–1522, 2004.

[69] E. Bor, M. Turduev, and H. Kurt, "Differential evolution algorithm based photonic structure design: numerical and experimental verification of subwavelength $\lambda/5$ focusing of light," *Scientific Reports*, vol. 6, p. 30871, 2016.

[70] J. Guan, J. Lin, Y. Ma, J. Tan, and P. Jin, "A subwavelength spot and a three-dimensional optical trap formed by a single planar element with azimuthal light," *Scientific Reports*, vol. 7, no. 1, p. 7380, 2017.

[71] J. Park, C. Park, K. Lee, Y.-H. Cho, and Y. Park, "Time-reversing a monochromatic subwavelength optical focus by optical phase conjugation of multiply-scattered light," *Scientific Reports*, vol. 7, p. 41384, 2017.

[72] Z. Wang, W. Guo, L. Li, B. Luk'yanchuk, A. Khan, Z. Liu, Z. Chen, and M. Hong, "Optical virtual imaging at 50 nm lateral resolution with a white-light nanoscope," *Nature Communications*, vol. 2, p. 218, 2011.

[73] S. Lee, L. Li, Y. Ben-Aryeh, Z. Wang, and W. Guo, "Overcoming the diffraction limit induced by microsphere optical nanoscopy," *Journal of Optics*, vol. 15, no. 12, p. 125710, 2013.

[74] Y. Lu, S. Theppakuttai, and S. Chen, "Marangoni effect in nanosphere-enhanced laser nanopatterning of silicon," *Applied Physics Letters*, vol. 82, no. 23, pp. 4143–4145, 2003.

[75] Z. Wang, B. Lukyanchuk, M. Hong, Y. Lin, and T. Chong, "Energy flow around a small particle investigated by classical mie theory," *Physical Review B*, vol. 70, no. 3, p. 035418, 2004.

[76] S. Theppakuttai and S. Chen, "Submicron ripple formation on glass surface upon laser-nanosphere interaction," *Journal of Applied Physics*, vol. 95, no. 9, pp. 5049–5052, 2004.

[77] A. Battula, S. P. Theppakuttai, and S. Chen, "Direct, parallel nanopatterning of silicon carbide by laser nanosphere lithography," *Journal of Micro/Nanolithography, MEMS, and MOEMS*, vol. 5, no. 1, p. 011009, 2006.

[78] T. Krupenkin, S. Yang, and P. Mach, "Tunable liquid microlens," *Applied Physics Letters*, vol. 82, no. 3, pp. 316–318, 2003.

[79] S. Kuiper and B. Hendriks, "Variable-focus liquid lens for miniature cameras," *Applied Physics Letters*, vol. 85, no. 7, pp. 1128–1130, 2004.

[80] H. Oku, K. Hashimoto, and M. Ishikawa, "Variable-focus lens with 1-khz bandwidth," *Optics Express*, vol. 12, no. 10, pp. 2138–2149, 2004.

[81] M. von Waldkirch, P. Lukowicz, and G. Tröster, "Oscillating fluid lens in coherent retinal projection displays for extending depth of focus," *Optics Communications*, vol. 253, no. 4-6, pp. 407–418, 2005.

[82] E. Castillo-Orozco, A. Davanlou, P. K. Choudhury, and R. Kumar, "Droplet impact on deep liquid pools: Rayleigh jet to formation of secondary droplets," *Physical Review E*, vol. 92, no. 5, p. 053022, 2015.

[83] C. A. López, C.-C. Lee, and A. H. Hirsa, "Electrochemically activated adaptive liquid lens," *Applied Physics Letters*, vol. 87, no. 13, p. 134102, 2005.

[84] K. Campbell, Y. Fainman, and A. Groisman, "Pneumatically actuated adaptive lenses with millisecond response time," *Applied Physics Letters*, vol. 91, no. 17, p. 171111, 2007.

[85] D.-Y. Zhang, N. Justis, and Y.-H. Lo, "Fluidic adaptive lens of transformable lens type," *Applied Physics Letters*, vol. 84, no. 21, pp. 4194–4196, 2004.

[86] W. Steen, "Laser material processingan overview," *Journal of Optics A: Pure and Applied Optics*, vol. 5, no. 4, p. S3, 2003.

[87] W. M. Steen and J. Mazumder, *Laser material processing*. Springer Science & Business Media, 2010.

[88] N. Bieri, J. Chung, S. Haferl, D. Poulikakos, and C. Grigoropoulos, "Microstructuring by printing and laser curing of nanoparticle solutions," *Applied Physics Letters*, vol. 82, no. 20, pp. 3529–3531, 2003.

[89] N. Bieri, J. Chung, D. Poulikakos, and C. Grigoropoulos, "Manufacturing of nanoscale thickness gold lines by laser curing of a discretely deposited nanoparticle suspension," *Superlattices and Microstructures*, vol. 35, no. 3-6, pp. 437–444, 2004.

[90] J. Chung, N. Bieri, S. Ko, C. Grigoropoulos, and D. Poulikakos, "In-tandem deposition and sintering of printed gold nanoparticle inks induced by continuous gaussian laser irradiation," *Applied Physics A*, vol. 79, no. 4-6, pp. 1259–1261, 2004.

[91] T.-H. Han, Y. Lee, M.-R. Choi, S.-H. Woo, S.-H. Bae, B. H. Hong, J.-H. Ahn, and T.-W. Lee, "Extremely efficient flexible organic light-emitting diodes with modified graphene anode," *Nature Photonics*, vol. 6, no. 2, p. 105, 2012.

[92] M. Vomero, E. Castagnola, F. Ciarpella, E. Maggiolini, N. Goshi, E. Zucchini, S. Carli, L. Fadiga, S. Kassegne, and D. Ricci, "Highly stable glassy carbon interfaces for long-term neural stimulation and low-noise recording of brain activity," *Scientific Reports*, vol. 7, p. 40332, 2017.

[93] W. S. Wong and A. Salleo, *Flexible electronics: materials and applications*. Springer Science & Business Media, 2009, vol. 11.

[94] M. Naguib, V. N. Mochalin, M. W. Barsoum, and Y. Gogotsi, "25th anniversary article: Mxenes: a new family of two-dimensional materials," *Advanced Materials*, vol. 26, no. 7, pp. 992–1005, 2014.

[95] H. An, T. Habib, S. Shah, H. Gao, M. Radovic, M. J. Green, and J. L. Lutkenhaus, "Surface-agnostic highly stretchable and bendable conductive mxene multilayers," *Science Advances*, vol. 4, no. 3, p. eaaq0118, 2018.

[96] Q. Zhang, Y. Zheng, and J. Liu, "Direct writing of electronics based on alloy and metal (dream) ink: A newly emerging area and its impact on energy, environment and health sciences," *Frontiers in Energy*, vol. 6, no. 4, pp. 311–340, 2012.

[97] J. Castro, E. A. Rojas-Nastrucci, A. Ross, T. M. Weller, and J. Wang, "Fabrication, modeling, and application of ceramic-thermoplastic composites for fused deposition modeling of microwave components," *IEEE Transactions on Microwave Theory and Techniques*, vol. 65, no. 6, pp. 2073–2084, 2017.

[98] J. Perelaer, P. J. Smith, D. Mager, D. Soltman, S. K. Volkman, V. Subramanian, J. G. Korvink, and U. S. Schubert, "Printed electronics: the challenges involved in printing devices, interconnects, and contacts based on inorganic materials," *Journal of Materials Chemistry*, vol. 20, no. 39, pp. 8446–8453, 2010.

[99] M. Singh, H. M. Haverinen, P. Dhagat, and G. E. Jabbour, "Inkjet printingprocess and its applications," *Advanced Materials*, vol. 22, no. 6, pp. 673–685, 2010.

[100] D.-H. Lee, Y.-J. Chang, G. S. Herman, and C.-H. Chang, "A general route to printable high-mobility transparent amorphous oxide semiconductors," *Advanced Materials*, vol. 19, no. 6, pp. 843–847, 2007.

[101] A. Kamyshny and S. Magdassi, "Conductive nanomaterials for printed electronics," *Small*, vol. 10, no. 17, pp. 3515–3535, 2014.

[102] J. R. Greer and R. A. Street, "Thermal cure effects on electrical performance of nanoparticle silver inks," *Acta Materialia*, vol. 55, no. 18, pp. 6345–6349, 2007.

[103] J. Perelaer, A. W. De Laat, C. E. Hendriks, and U. S. Schubert, "Inkjet-printed silver tracks: low temperature curing and thermal stability investigation," *Journal of Materials Chemistry*, vol. 18, no. 27, pp. 3209–3215, 2008.

[104] D. Huang, F. Liao, S. Molesa, D. Redinger, and V. Subramanian, "Plastic-compatible low resistance printable gold nanoparticle conductors for flexible electronics," *Journal of the Electrochemical Society*, vol. 150, no. 7, pp. G412–G417, 2003.

[105] S. H. Ko, H. Pan, C. P. Grigoropoulos, C. K. Luscombe, J. M. Fréchet, and D. Poulikakos, "All-inkjet-printed flexible electronics fabrication on a polymer substrate by low-temperature high-resolution selective laser sintering of metal nanoparticles," *Nanotechnology*, vol. 18, no. 34, p. 345202, 2007.

[106] A. Luque, A. Martí, and C. Stanley, "Understanding intermediate-band solar cells," *Nature Photonics*, vol. 6, no. 3, pp. nphoton–2012, 2012.

[107] T. Matsui, K. Ogata, M. Isomura, and M. Kondo, "Microcrystalline silicon–germanium alloys for solar cell application: Growth and material properties," *Journal of Non-Crystalline Solids*, vol. 352, no. 9-20, pp. 1255–1258, 2006.

[108] B.-Y. Oh, M.-C. Jeong, T.-H. Moon, W. Lee, J.-M. Myoung, J.-Y. Hwang, and D.-S. Seo, "Transparent conductive al-doped zno films for liquid crystal displays," *Journal of Applied Physics*, vol. 99, no. 12, p. 124505, 2006.

[109] D. Zeng, W. P. Latham, and A. Kar, "Shaping of annular laser intensity profiles and their thermal effects for optical trepanning," *Optical Engineering*, vol. 45, no. 1, p. 014301, 2006.

[110] E. Castillo-Orozco, A. Davanlou, P. K. Choudhury, and R. Kumar, "On the impact of liquid drops on immiscible liquids," in *ASME 2016 14th International Conference on Nanochannels, Microchannels, and Minichannels collocated with the ASME 2016 Heat Transfer Summer Conference and the ASME 2016 Fluids Engineering Division Summer Meeting*. American Society of Mechanical Engineers, 2016, pp. V001T08A005–V001T08A005.

[111] P. K. Choudhury, A. Davanlou, E. Castillo Orozco, and R. Kumar, "Global and local measurements and proper orthogonal decomposition of a swirling conical liquid sheet," in *ASME 2016 Fluids Engineering Division Summer Meeting collocated with the ASME 2016 Heat Transfer Summer Conference and the ASME 2016 14th International Conference on Nanochannels, Microchannels, and Minichannels*. American Society of Mechanical Engineers, 2016, pp. V01BT20A005–V01BT20A005.

[112] A. Al-Azzawi, *Light and optics: principles and practices*. CRC Press, 2006.

[113] S. B. Fuller, E. J. Wilhelm, and J. M. Jacobson, "Ink-jet printed nanoparticle microelectromechanical systems," *Journal of Microelectromechanical Systems*, vol. 11, no. 1, pp. 54–60, 2002.

[114] D. Milanova and R. Kumar, "Role of ions in pool boiling heat transfer of pure and silica nanofluids," *Applied Physics Letters*, vol. 87, no. 23, p. 233107, 2005.

[115] A. Davanlou, J. D. Lee, S. Basu, and R. Kumar, "Effect of viscosity and surface tension on breakup and coalescence of bicomponent sprays," *Chemical Engineering Science*, vol. 131, pp. 243–255, 2015.

[116] A. Davanlou and R. Kumar, "Thermally induced collision of droplets in an immiscible outer fluid," *Scientific Reports*, vol. 5, p. 9531, 2015.

[117] B. Pongrác, H. Kim, M. Janda, V. Martišovitš, and Z. Machala, "Fast imaging of intermittent electrospraying of water with positive corona discharge," *Journal of Physics D: Applied Physics*, vol. 47, no. 31, p. 315202, 2014.

[118] W. J. Scheideler and C.-H. Chen, "The minimum flow rate scaling of taylor cone-jets issued from a nozzle," *Applied Physics Letters*, vol. 104, no. 2, p. 024103, 2014.

[119] A. Barrero, A. Ganan-Calvo, J. Davila, A. Palacios, and E. Gomez-Gonzalez, "The role of the electrical conductivity and viscosity on the motions inside taylor cones," *Journal of Electrostatics*, vol. 47, no. 1-2, pp. 13–26, 1999.

[120] R. T. Collins, J. J. Jones, M. T. Harris, and O. A. Basaran, "Electrohydrodynamic tip streaming and emission of charged drops from liquid cones," *Nature Physics*, vol. 4, no. 2, p. 149, 2008.

[121] S. Jayasinghe and M. Edirisinghe, "Effect of viscosity on the size of relics produced by electrostatic atomization," *Journal of Aerosol Science*, vol. 33, no. 10, pp. 1379–1388, 2002.

[122] J. Yu, S. Kim, and J. Hwang, "Effect of viscosity of silver nanoparticle suspension on conductive line patterned by electrohydrodynamic jet printing," *Applied Physics A*, vol. 89, no. 1, pp. 157–159, 2007.

[123] A. Speranza and M. Ghadiri, "Effect of electrostatic field on dripping of highly conductive and viscous liquids," *Powder Technology*, vol. 135, pp. 361–366, 2003.

[124] J. D. Wehking, L. Chew, and R. Kumar, "Droplet deformation and manipulation in an electrified microfluidic channel," *Applied Physics Letters*, vol. 103, no. 5, p. 054101, 2013.

[125] J. D. Wehking and R. Kumar, "Droplet actuation in an electrified microfluidic network," *Lab on a Chip*, vol. 15, no. 3, pp. 793–801, 2015.

[126] J. Mazumder and A. Kar, *Theory and application of laser chemical vapor deposition*. Springer Science & Business Media, 2013.

[127] A. Jones and K. Thong, "The production of charged monodisperse fuel droplets by electrical dispersion," *Journal of Physics D: Applied Physics*, vol. 4, no. 8, p. 1159, 1971.

[128] G. F. Scheele and B. J. Meister, "Drop formation at low velocities in liquid-liquid systems: Part i. prediction of drop volume," *Aiche Journal*, vol. 14, no. 1, pp. 9–15, 1968.

[129] A. Adamson and A. Gast, "Wiley interscience publication," *Physical Chemistry of Surfaces, John Wiley & Sons, Inc., New York*, 1997.

[130] J. D. Wehking, M. Gabany, L. Chew, and R. Kumar, "Effects of viscosity, interfacial tension, and flow geometry on droplet formation in a microfluidic t-junction," *Microfluidics and Nanofluidics*, vol. 16, no. 3, pp. 441–453, 2014.

[131] F. Cruz-Mazo, J. Montanero, and A. Gañán-Calvo, "Monosized dripping mode of axisymmetric flow focusing," *Physical Review E*, vol. 94, no. 5, p. 053122, 2016.

[132] D. Tam, V. von ARNIM, G. McKinley, and A. Hosoi, "Marangoni convection in droplets on superhydrophobic surfaces," *Journal of Fluid Mechanics*, vol. 624, pp. 101–123, 2009.

[133] Y. Shen, S. Liu, C. Zhu, J. Tao, Z. Chen, H. Tao, L. Pan, G. Wang, and T. Wang, "Bouncing dynamics of impact droplets on the convex superhydrophobic surfaces," *Applied Physics Letters*, vol. 110, no. 22, p. 221601, 2017.

[134] T. M. Schutzius, S. Jung, T. Maitra, G. Graeber, M. Köhme, and D. Poulikakos, "Spontaneous droplet trampolining on rigid superhydrophobic surfaces," *Nature*, vol. 527, no. 7576, p. 82, 2015.

[135] C. Hao, J. Li, Y. Liu, X. Zhou, Y. Liu, R. Liu, L. Che, W. Zhou, D. Sun, L. Li *et al.*, "Superhydrophobic-like tunable droplet bouncing on slippery liquid interfaces," *Nature Communications*, vol. 6, p. 7986, 2015.

[136] J. Burton, A. Sharpe, R. Van Der Veen, A. Franco, and S. Nagel, "Geometry of the vapor layer under a leidenfrost drop," *Physical Review Letters*, vol. 109, no. 7, p. 074301, 2012.

[137] F. Celestini, T. Frisch, and Y. Pomeau, "Take off of small leidenfrost droplets," *Physical Review Letters*, vol. 109, no. 3, p. 034501, 2012.

[138] J. Maxwell, "Problems," *Cambridge and Dublin Math. J.*, vol. 8, p. 188, 1854.

[139] R. Lüneberg, "Mathematical theory of optics p. 401," *(Brown University Press, Rhode Island, 1944)*.

[140] J. Valentine, J. Li, T. Zentgraf, G. Bartal, and X. Zhang, "An optical cloak made of dielectrics," *Nature Materials*, vol. 8, no. 7, p. 568, 2009.

[141] L. H. Gabrielli, J. Cardenas, C. B. Poitras, and M. Lipson, "Silicon nanostructure cloak operating at optical frequencies," *Nature Photonics*, vol. 3, no. 8, p. 461, 2009.

[142] P. Fischer, V. Romano, H.-P. Weber, and S. Kolossov, "Pulsed laser sintering of metallic powders," *Thin Solid Films*, vol. 453, pp. 139–144, 2004.

[143] D. Zhang, H. Yabe, E. Akita, P. Wang, R.-i. Murakami, and X. Song, "Effect of silver evolution on conductivity and transmittance of zno/ag thin films," *Journal of Applied Physics*, vol. 109, no. 10, p. 104318, 2011.

[144] A. Russo, B. Y. Ahn, J. J. Adams, E. B. Duoss, J. T. Bernhard, and J. A. Lewis, "Pen-on-paper flexible electronics," *Advanced Materials*, vol. 23, no. 30, pp. 3426–3430, 2011.

[145] S. Merilampi, T. Laine-Ma, and P. Ruuskanen, "The characterization of electrically conductive silver ink patterns on flexible substrates," *Microelectronics Reliability*, vol. 49, no. 7, pp. 782–790, 2009.